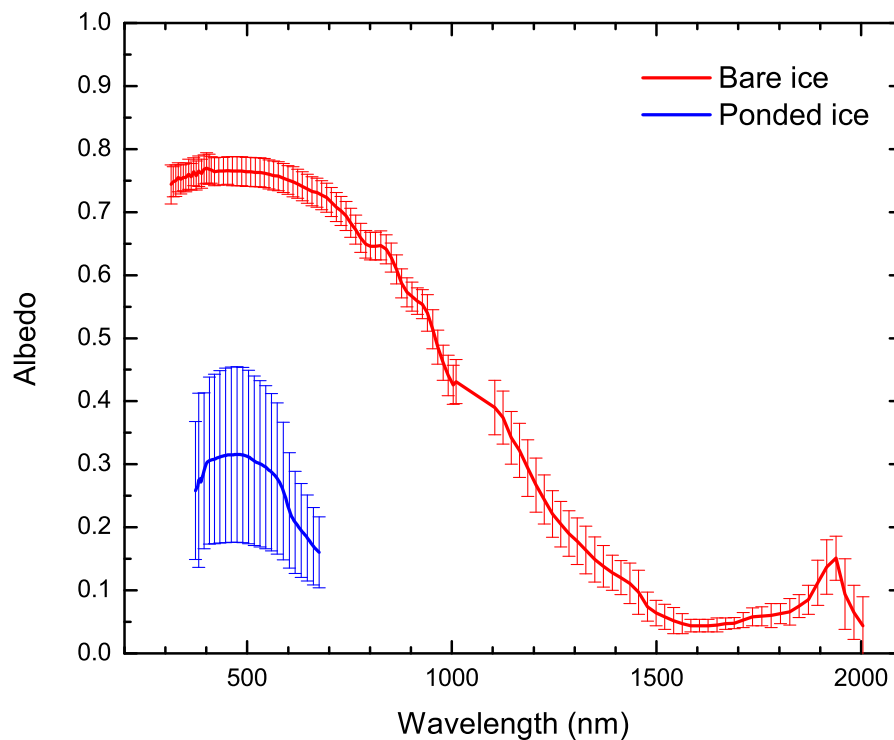


February 2007

A Delta-Eddington Multiple Scattering Parameterization for Solar Radiation in the Sea Ice Component of the Community Climate System Model

B. P. Briegleb and B. Light



CLIMATE AND GLOBAL DYNAMICS DIVISION

NATIONAL CENTER FOR ATMOSPHERIC RESEARCH
BOULDER, COLORADO

**A DELTA-EDDINGTON MULTIPLE SCATTERING
PARAMETERIZATION FOR SOLAR RADIATION
IN THE SEA ICE COMPONENT OF THE
COMMUNITY CLIMATE SYSTEM MODEL**

by Bruce P. Briegleb and Bonnie Light¹

National Center for Atmospheric Research
P.O. Box 3000, Boulder, CO 80307

¹ Polar Science Center, Applied Physics Laboratory, University of Washington

TABLE OF CONTENTS

Abstract	v
1. Introduction	1
2. Present Version of Solar Radiation in CCSM Sea Ice	2
3. Overview of the Delta-Eddington Solar Radiation Treatment for Sea Ice	9
4. Delta-Eddington Solar Radiation Treatment: Theory	14
4.1 Refraction	14
4.2 Single Scattering	17
4.3 Multiple Scattering Within a Layer	20
4.4 Multiple Scattering Between Layers	25
4.5 Apparent Optical Properties: Albedo, Absorbed and Transmitted Flux	26
5. Delta-Eddington Solar Radiation Treatment: Data	28
5.1 Spectral Bands	28
5.2 Inherent Optical Properties: Snow	28
A. Pure Snow	28
B. Aerosols in Snow	35
C. Transition From Snow Covered Ice to Bare Ice	35
D. Tuning Snow Apparent Optical Properties	36
5.3 Inherent Optical Properties: Sea Ice	37
A. Derivation of Bare Ice and Pondered Ice Profiles	37
B. Absorption by Algae	44
C. Transmittance Through Bare Ice and Pondered Ice	45
D. Variability	46
E. Transition From Bare Ice to Pondered Ice	47
F. Tuning Bare Ice and Pondered Ice Apparent Optical Properties	48
6. Delta-Eddington Solar Radiation Treatment: Comparisons	50
6.1 Benchmark Radiation Model for Snow: SNICAR	51
6.2 Benchmark Radiation Model for Sea Ice: Monte Carlo	53
6.3 Present Version of Solar Radiation in CCSM Sea Ice	57
7. Summary	60
Acknowledgments	60
Appendix A: Delta-Eddington Solution for a Single Layer	61
Appendix B: Solution for Multiple Layers	67
Appendix C: Atmosphere Radiation Model	72
Appendix D: Variable Number of Snow and Sea Ice Layers	74
Appendix E: Glossary of Acronyms	77
References	78
Figures	81

Abstract

Many climate model predictions of future climate change due to increasing greenhouse gases indicate polar warming two to three times the global mean (Holland and Bitz, 2003). One important factor in this enhanced polar warming is thought to be the snow and sea ice albedo feedback (Curry et al. 1995). The essence of this feedback is the strong contrast in how open water and snow-covered or bare sea ice reflect, absorb, and transmit incoming solar radiation. Snow and sea ice have high albedo; open water has low albedo. The high albedo of snow and sea ice is caused by multiple scattering attributed to individual snow grains and inclusions of gas, brine and precipitated salt crystals embedded in sea ice (Light et al. 2004). An accurate representation of solar radiation transfer in the snow/sea ice system requires a multiple scattering parameterization (Jin et al. 1994; Curry et al. 2001).

Interactions between snow and sea ice and solar radiation in the present version of the Community Climate System Model (Version 3) are not based on a multiple scattering calculation. Rather, these interactions are based on empirical parameterizations which depend solely on the depth of snow (if any) overlying sea ice, sea ice thickness and its surface temperature. Considerable arbitrariness and inconsistency are inherent in these parameterizations since it is possible to alter one part of this parameterization independent of other parts, which is often done when tuning sea ice albedo to achieve acceptable CCSM present-day simulations. Because of this arbitrariness and inconsistency, it is likely that the solar radiation parameterization for snow and sea ice in the present CCSM may not adequately represent the radiation physics necessary for an accurate estimate of the snow and sea ice albedo feedback.

A Delta-Eddington multiple scattering radiative transfer model is presented here as an alternative treatment for the interactions between solar radiation and snow and sea ice. Optical properties for snow and sea ice are prescribed based on physical measurements. These optical properties are then used in the radiative transfer model to compute the albedo, absorption within snow and sea ice and transmission to the underlying ocean. Snow and sea ice surface albedos and transmissions in this parameterization agree well with observations made during SHEBA (Perovich et al. 2002). The effects of absorption due to impurities such as carbon soot can be included without loss of consistency. This parameterization also provides opportunities for further improvements in the CCSM treatment of snow and sea ice physics, such as snow aging, vertical gradients in snow pack properties, and the effects of surface melt ponds. Employing the Delta-Eddington solar radiation parameterization for sea ice in CCSM will afford more consistent tuning for present climate, more accurate simulation of control climate annual cycle and variability, and provide increased confidence in simulations of future climate change.

1. Introduction

The Community Climate System Model, Version 3 (CCSM3) is a state-of-the-art coupled climate model (Collins et al., 2006), which includes a sea ice component (Briegleb et al. 2004). This sea ice component is a considerable improvement over its predecessor (Weatherly et al. 1998). It consists of elastic-viscous-plastic dynamics, energy conserving thermodynamics with resolved vertical temperature profile and explicit brine pocket parameterization, ice thickness distribution with five categories, linear remapping for thickness space evolution, mechanical redistribution due to rafting and ridging, ice strength computed from energetics, lateral and bottom melt processes, and second order horizontal advection using remapping.

Despite these improvements in thermodynamic and dynamic representation of sea ice processes, the solar radiation parameterization is relatively simple. Apparent optical properties (AOPs), including the albedo and extinction of solar radiation, are prescribed. Various measurements are used to correlate these optical properties with snow depth, sea ice thickness, and surface temperature.

Given the importance of the snow/sea ice albedo feedback in climate sensitivity (Maykut and Perovich, 1987, Curry et al. 1995, Holland and Bitz, 2003), this relatively simple method for computing the partitioning of solar radiation may not include enough physics to accurately describe the feedback. Holland and Bitz (2003) show how several models involved in the Coupled Model Intercomparison Project have polar warming in response to doubled CO_2 that is about two to three times that of the global mean. Snow and sea ice albedo feedback, as well as the basic sea ice simulation state, are important factors in polar amplification.

How well is the physics of solar radiation being represented in climate models other than CCSM3? Curry et al. (2001) compare several popular snow/ice albedo parameterizations against SHEBA/FIRE data. None are based on a multiple scattering method. While some of the parameterizations compare favorably with the data, all are based on the same method of prescribing AOPs (snow/sea ice albedo) based on gross physical properties (surface temperature and snow/sea ice thickness). In addition, Curry et al. 2001 (p. 15355) write “These calculations illustrate that two different albedo parameterizations used in the same sea ice model, with the same average surface albedo and very nearly the same baseline conditions, can produce markedly different strengths of the ice-albedo feedback mechanism. While it appears that a simple albedo parameterization tuned to give appropriate results for snow-covered and melting ice can give reasonable results when used in a sea ice model, it may be important to include a more complex albedo treatment to reproduce correctly the ice-albedo feedback and radiative interactions with the atmosphere.”.

Here we present an alternative parameterization for the interaction between sea ice and solar radiation in CCSM. Rather than prescribing AOPs, it prescribes inherent optical

properties (IOPs) for snow-covered, bare and ponded sea ice. Inherent optical properties define the scattering and absorption properties for snow and sea ice and included absorbers. The IOPs provide a framework for a physically based, self-consistent multiple scattering calculation of the disposition of solar radiation in the sea ice system.

These IOPs are then used in a Delta(also δ)-Eddington multiple scattering parameterization, along with information about the boundary conditions (snow depth and sea ice thickness) and incident light, to compute AOPs, including the albedo, internal absorption, and transmission to the underlying ocean. While there are several methods of approximating multiple scattering that could be used for the sea ice system, the Delta-Eddington method is one that the first author of this report is familiar with, and one which gives accurate and efficient results, as will be illustrated. Such a method has been used successfully in the atmospheric component of CCSM (Collins et al. 2004) for computing radiative transfer through gas molecules, aerosols and cloud particles. A small modification to the technique was required to approximate refraction at sea ice and melt pond surfaces.

In this report, we first review the solar radiation parameterization in the sea ice component of the present version of CCSM (Section 2). This gives the rationale for presenting an alternative solar radiation parameterization. An overview of the alternative Delta-Eddington solar radiation parameterization for sea ice is then presented (Section 3), then the specifics of the theory (Section 4), data (Section 5), comparisons with other calculations (Section 6), and finally a summary (Section 7). The appendices present the Delta-Eddington multiple scattering solution for a single layer, the solution for inter-layer scattering, a summary of the polar atmospheric radiation model used for various calculations in this work, some issues relevant to varying the number of snow and sea ice layers, and a glossary of acronyms.

2. Present Version of Solar Radiation in CCSM Sea Ice

In this section we review the solar radiation parameterization in the sea ice component of CCSM3. We will highlight and discuss the origin, rationale and limitations of the present parameterization.

The atmospheric component of CCSM3 provides the sea ice component with the downward solar radiation flux incident at the top sea ice surface, separated firstly into two terms by spectral region and each secondarily into two more terms which distinguish the direct solar beam radiation from the diffuse solar radiation. These solar radiation fluxes are assumed to be incident uniformly upon all categories of sea ice thickness in the sea ice component, so that the solar radiation parameterization reviewed in this section is the same for each sea ice thickness category. The final sea ice component albedos and fluxes are computed by aggregating the albedo and flux for each category over the ice thickness distribution (Briegleb et al. 2004).

Solar radiation in the atmospheric component is spectrally distinguished because many

radiative processes in both the atmosphere and the surface have different character in two broad wavelength regions: less than $700nm$ and greater than $700nm$. Thus the region with wavelengths less than $700nm$, termed the visible band, is distinguished from the region with wavelengths greater than $700nm$, termed the near-infrared band (the $700nm$ wavelength is a somewhat arbitrary but convenient separating wavelength for these two bands). In the atmosphere these two wavelength regions distinguish the relatively transparent visible band from the relatively opaque near-infrared band.

Solar radiation in the atmospheric component is separated into direct and diffuse portions to take into account any solar zenith angle (the angle between the sun and the zenith) dependence of the surface albedo. The direct term is that due to the non-scattered solar beam that penetrates to the surface; the diffuse term is that due to multiple scattering out of the solar beam in the atmosphere and/or with the surface that results in diffuse surface radiation. This diffuse radiation is assumed to be isotropic in the downwards hemisphere, though in reality there is some angular dependence. Note that the diffuse radiation flux accounts for multiple reflections between the surface and the atmosphere (usually due to clouds), a process that is particularly important in high albedo snow and ice covered regions. For example, such multiple reflections can substantially increase the downwelling diffuse solar radiation at the surface for cloudy conditions compared to clear sky conditions.

The four separate solar radiation fluxes, whose sum is the total downwelling solar radiation flux incident on the snow and sea ice surface, can be written as:

$$F_{SWDN} = F_{SWvsdr} + F_{SWvsdf} + F_{SWnidr} + F_{SWnidf} \quad (1)$$

where we use the notation of Briegleb et al. (2004), noting that in CCSM3, “short-wave”=SW is synonymous with “solar”. The visible band direct and diffuse fluxes are then F_{SWvsdr} and F_{SWvsdf} respectively, while the near-infrared band direct and diffuse fluxes are F_{SWnidr} and F_{SWnidf} respectively. For example, the subscript $SWvsdr$ refers to the solar (i.e. shortwave flux, SW), visible band (vs) and direct beam (dr), while $SWnidr$ refers to the corresponding near-infrared band (ni) flux. The subscript “df” refers to the diffuse flux. The term “shortwave” is used in CCSM3 to distinguish solar radiation fluxes from the “longwave”, or thermal radiation fluxes. The latter are not referred to in this report, where we focus exclusively on the solar (i.e. “shortwave”) fluxes.

Any parameterization of solar radiation at the Earth surface in CCSM3 must use these fluxes as upper boundary conditions for the reflection and absorption of solar radiation at and below the surface. For general radiation modeling of the surface, the solar zenith angle is also required, but in the sea ice component of CCSM3 it is not used, as the albedos for the direct solar beam are not distinguished from albedos for diffuse solar radiation. As will be shown in section 6.3, the ‘zenith angle dependence’ of albedos and absorbed fluxes for snow, sea ice, and pond is not negligible, and should be allowed for.

For the present solar radiation parameterization in the sea ice component of CCSM3, snow/ice albedo depends on spectral band (visible *vs* and near-infrared *ni*), surface temperature T_s (of snow if present, or sea ice, °C), snow thickness h_s (m), sea ice thickness h_i (m), and CCSM3 ocean and sea ice horizontal resolution (x1 and x3, referring to the nominal $1^\circ \times 1^\circ$ and $3^\circ \times 3^\circ$ resolutions, respectively; see Briegleb et al. (2004)).

We will first consider snow-covered sea ice, then bare and ponded sea ice.

For the present solar parameterization in CCSM3, snow on sea ice is distinguished by non-melting and near-melting conditions. The surface temperature T_s is used to distinguish these two conditions. For $T_s < -1^\circ\text{C}$, non-melting snow albedos are

$$\begin{aligned}\alpha_{vsdf}^s(\text{non melting}) &= 0.96 (\times 1), 0.91 (\times 3) \\ \alpha_{nidf}^s(\text{non melting}) &= 0.68 (\times 1), 0.63 (\times 3)\end{aligned}\tag{2}$$

where superscript “s” refers to snow, and $\times 1$ and $\times 3$ refer to the two standard CCSM3 ocean and sea ice horizontal resolutions respectively. The -1°C criterion is purely arbitrary, as discussed below. Note that only the albedos for diffuse solar radiation (“df”) are shown, as the albedos for direct solar radiation are identical for the respective bands. Broadband albedos can be estimated by knowing the partition of visible/near-infrared fluxes from the atmosphere. This partition depends mainly on solar zenith angle, cloudiness and surface albedo. Typical partitions for clear sky snow are 52%/48%, for clear sky sea ice (1.5 m thick) 51%/49%, and for clear sky deep ponds (.35 m pond over 1.5 m sea ice) 50%/50%. For overcast sky, typical partitions range from 62%/38% for bright snow and 61%/39% for dark pond, to 65%/35% for bare sea ice to 69%/31% for darker snow. A mean overcast sky partition would be 65%/35%. If we take the 65%/35% *vs* and *ni* partition, the broadband albedos are $0.86(\times 1)$ and $0.81(\times 3)$.

Near-melting snow albedos are determined for $T_s > -1^\circ\text{C}$ by:

$$\begin{aligned}\Delta T_s &= 0, & T_s < -1^\circ\text{C} \\ &= T_s + 1, & T_s > -1^\circ\text{C}\end{aligned}\tag{3}$$

$$\begin{aligned}\alpha_{vsdf}^s(\text{near melting}) &= \alpha_{vsdf}^s(\text{non melting}) - 0.10 \Delta T_s \\ \alpha_{nidf}^s(\text{near melting}) &= \alpha_{nidf}^s(\text{non melting}) - 0.15 \Delta T_s\end{aligned}$$

At $T_s = 0^\circ\text{C}$, the near-melting albedos are .86, .53 *vs* and *ni* respectively ($\times 1$), and .81, .47 *vs* and *ni* respectively ($\times 3$), with a broadband 65%/35% value of 0.745($\times 1$) and 0.691($\times 3$).

For snow on sea ice, the present solar radiation parameterization does not allow for physical property evolution. It is not known how long the snow has been on the surface, or whether previous melting and refreezing has occurred. Snow depth is increased by snow fall and decreased by snow melt. Since there is no snow aging dependence, snow can melt and then freeze again, and for $T_s < -1^\circ\text{C}$, the snow albedos will return to the non-melting values (Eq. 2); there is no dependence on snow thickness or on the albedo of the underlying sea

ice. Again, these are diffuse albedos, as the zenith angle dependence for the snow albedo is neglected. The temperature boundary -1°C was chosen, rather than 0°C , because in reality for near-melting conditions, slight declines in T_s below melting temperature do not lead to large increases in albedo, unless declines become significant. It is acknowledged that this is a crude empirical approximation.

For the non-melting snow albedos of Eq. 2 and the near-melting albedos of Eq. 3, the declines in albedo between resolutions in the former and between spectral bands in the latter use spectral partitions (i.e. changes in spectral albedos) that are either uniform (Eq. 2) or rough guesses (Eq. 3). For example, for the tuned albedos of Eq. 2, the decline in visible albedo (.05) equals that for the near-infrared albedo. One would not expect this in actuality. As will be shown in Section 5.2 of this report, snow albedo depends on grain size and spectral band. The temperature dependent declines in snow albedo in Eq. 3 (.10 and .15) are rough guesses whose accuracy is not known.

In reality, snow falls initially as a distribution of snow crystal shapes and sizes, but rapidly transforms once settled on the surface primarily by vapor diffusion into nearly uni-modal and roughly spherically-shaped snow grains (Flanner and Zender, 2006). These grains continue growing slowly over time by temperature-dependent vapor diffusion. Until significant compaction occurs, density remains low and there is considerable air space between the contiguous, nearly spherical snow grains. Temperatures near melting result in a rapid growth in snow grain size, and melting results in the presence of liquid water within the snow. The addition of liquid water, along with increasing grain size, generally cause snow albedos for melting or near-melting conditions to be lower than those for non-melting fresh snow.

The bare sea ice (i.e. no snow and no melt pond) albedos for non-melting ($T_s < -1^\circ\text{C}$), thick sea ice ($h_i > 0.5$ m) are:

$$\begin{aligned}\alpha_{vsdf}^i(\text{non melting, thick}) &= 0.73 (\times 1), 0.68 (\times 3) \\ \alpha_{nidf}^i(\text{non melting, thick}) &= 0.33 (\times 1), 0.30 (\times 3)\end{aligned}\tag{4}$$

where the superscript “i” refers to bare sea ice. The bare sea ice albedos for non-melting ($T_s < -1^\circ\text{C}$), thin sea ice ($h_i < 0.5$ m) are:

$$\begin{aligned}\alpha_{vsdf}^i(\text{non melting, thin}) &= \alpha^o (1 - fh) + \alpha_{vsdf}^i(\text{non melting, thick}) fh \\ \alpha_{nidf}^i(\text{non melting, thin}) &= \alpha^o (1 - fh) + \alpha_{nidf}^i(\text{non melting, thick}) fh\end{aligned}\tag{5}$$

where α^o is the open ocean diffuse albedo ($= .06$), and

$$fh = \min([\tan^{-1}(c_{fh} h_i) / \tan^{-1}(c_{fh} 0.5)], 1)\tag{6}$$

with $c_{fh} = 4 \text{ m}^{-1}$. The 0.5 m sea ice thickness between thin and thick albedos is somewhat arbitrary, being loosely based on measurements. The \tan^{-1} dependence of albedo for thin sea ice is loosely based on theoretical arguments. Note that the spectral and zenith angle

dependences of ocean albedo are ignored. For the greatest consistency with the ocean component of CCSM3, the spectral and zenith angle dependence of ocean albedo in the sea ice component should be identical to that of the ocean component.

The thickness dependent coefficients c_{fh} and 0.5 in Eq. 6 can be used as tuning coefficients, independent of any other changes in the surface albedo parameterization. Notice also that changes in band albedo for the two resolutions of Eq. 4 differ from those in Eq. 2 for snow; again the accuracy of these changes is not known.

Liquid water from snow melt collects at the base of the snow and either percolates through the sea ice, runs off into the ocean through leads or other fissures in the sea ice, or drains laterally into low-lying regions on the surface of sea ice. Liquid water from bare melting sea ice follows similar paths, resulting in melt ponds covering a horizontal fraction of melting bare sea ice (Perovich et al. 2002). Melt ponds are mostly transparent to visible radiation, but are strongly absorptive of near-infrared radiation. However, the sea ice under melt ponds, as will be shown in section 5.3, has less scattering than non-ponded bare melting sea ice. This appears to be due to melt pond water filling the voids in the surface layer of melting sea ice. These effects combine to reduce pond albedo compared to adjacent bare melting sea ice albedo. In the present solar parameterization for sea ice in CCSM3, this effect is implicitly approximated by:

$$\begin{aligned}\alpha_{vsdf}^{pi}(\text{near melting}) &= \alpha_{vsdf}^i(\text{non melting, thin or thick}) - 0.075 \Delta T_s \\ \alpha_{nidf}^{pi}(\text{near melting}) &= \alpha_{nidf}^i(\text{non melting, thin or thick}) - 0.075 \Delta T_s\end{aligned}\tag{7}$$

where the superscript “pi” refers to ponded sea ice, and ΔT_s is from Eq. 3. The spectral albedos at 0°C are 0.655, 0.255 ($\times 1$) and 0.605, 0.225 ($\times 3$) with the broadband albedo at 65%/35% partition of 0.515 ($\times 1$) and 0.472 ($\times 3$). Thus, when bare sea ice has surface temperature near melting, the effects of melt ponds are implicitly included. The spectrally uniform decline in band albedo of .075 for ponded ice is simply an educated guess, constrained somewhat by SHEBA measurements (Perovich et al. 2002). Note that there is no explicit pond fraction or depth, and no explicit pond albedo (i.e. for complete pond coverage over sea ice).

Notice that the resolution-tuned albedos, spectral band partitions, and near-melting albedo declines of Eqs. 2, 3, 4 and 7, can all be modified independently of one another.

It was mentioned above that snow albedo has no dependence on snow thickness (Eqs. 2 and 3). This is the case when thick snow overlies sea ice, for which complete coverage is assumed. However, it is observed that when snow thickness drops to a few centimeters, some underlying sea ice is uncovered due to variations in surface topography of sea ice. To crudely approximate this effect, the total horizontally-averaged snow and sea ice albedo over each ice thickness category is computed by weighting the snow and sea ice albedos together using the following empirical fraction of horizontal coverage of the sea ice by the

overlying snow of thickness h_s :

$$f_s = \frac{h_s}{h_s + 0.02} \quad (8)$$

This accounts for small vertical inhomogeneities in the sea ice which prevent small layers of snow from completely covering the ice. It is also advantageous for numerical reasons by allowing a smoother transition between snow and ice albedos for small snow thickness. The value of .02 m was taken from observations that a couple of centimeters of snow covers quite a bit of the underlying sea ice. Thus, the total horizontally-averaged snow and sea ice albedo is:

$$\begin{aligned} \alpha_{vsdf} &= f_s \alpha_{vsdf}^s + (1 - f_s) \alpha_{vsdf}^{pi} \\ \alpha_{vsdr} &= \alpha_{vsdf} \\ \alpha_{nidf} &= f_s \alpha_{nidf}^s + (1 - f_s) \alpha_{nidf}^{pi} \\ \alpha_{nidr} &= \alpha_{nidf} \end{aligned} \quad (9)$$

where the albedos with no superscripts refer to the area averaged albedo over sea ice in each ice thickness category. As noted above, the direct albedos are assumed identical to the diffuse as explicitly shown in Eqs. 9. The total albedos are limited for thin, bare melting sea-ice to be greater than the ocean albedo α^o .

For the present solar radiation parameterization in the sea ice component of CCSM3, the surface albedo, along with the four fluxes of Eq. 1, are used to determine the column absorption. Light not backscattered to the atmosphere is absorbed in the snow, sea ice and ocean column. The absorbed flux for visible, near-infrared bands, and the total absorption is:

$$F_{SWvs} = F_{SWvsdr} (1 - \alpha_{vsdr}) + F_{SWvsdf} (1 - \alpha_{vsdf}) \quad (10)$$

$$F_{SWni} = F_{SWnidr} (1 - \alpha_{nidr}) + F_{SWnidf} (1 - \alpha_{nidf}) \quad (11)$$

$$F_{SW} = F_{SWvs} + F_{SWni} \quad (12)$$

for the two spectral bands individually (Eqs. 10,11) and for the total solar radiation (Eq. 12).

Once band absorption is determined, a fixed fraction of each band absorption is considered absorbed at the surface, which then contributes to the surface temperature evaluation of the sea ice component (Briegleb et al., 2004). The rest of the band absorbed flux is assumed to penetrate the surface and be absorbed both within the sea ice interior as well as to penetrate into the underlying ocean. This approach only approximates the actual radiative transfer within the column. However, as we will discuss in this report in section 3, this approach does make use of the observation that the bulk of the backscattering from snow and sea ice surfaces occurs in fairly thin surface layers, and so the present solar parameterization approach is a reasonable first-order approximation. The amount of flux absorbed in the column used for the surface energy balance calculation is given by $F_{SWvs} - I_{0vs}$ for the visible and $F_{SWni} - I_{0ni}$ for the near-infrared, where I_{0vs}, I_{0ni} are the

portions of absorbed solar radiation in the visible and near-infrared that penetrate the surface, respectively, given by:

$$I_{0vs} = 0.0, \quad I_{0ni} = 0.0 \quad \text{snow over sea ice} \quad (13)$$

$$I_{0vs} = 0.70 F_{SWvs} (1 - f_s), \quad I_{0ni} = 0.0 \quad \text{bare and ponded sea ice} \quad (14)$$

For both snow and sea ice, the portion of total absorbed flux not penetrating into the sea ice is taken to be absorbed immediately at the surface. Thus, in the present sea ice component of CCSM3, there is an implied surface layer of unspecified thickness. While I_0 values (Eqs 13 and 14) may be good approximations for thick ice, they likely break down for thin ice conditions.

The internal heating (flux divergence) for the solar radiation penetrating below the surface layer is:

$$Q_{SW} = -\frac{d}{dz} \{I_{0vs} e^{-\kappa_{vs} z}\} \quad (15)$$

where z is the vertical coordinate in the ice increasing downwards from the ice surface ($z = 0$), and κ_{vs} the spectral absorption coefficient, evaluated using a radiation model (Gary Maykut, personal communication). Note that there is no distinction made between direct or diffuse solar radiation: in effect, we assume solar radiation penetrating the surface is diffuse. Also, the functional form of penetration in Eq. 15 is that for pure absorption; in effect, all scattering occurs at the surface while the rest of the ice is purely absorbing.

The solar radiation flux that penetrates to the underlying ocean through sea ice of thickness h_i , all of which is assumed to be absorbed in the ocean, is:

$$Q_{SWocn} = I_{0vs} e^{-\kappa_{vs} h_i} \quad (16)$$

This completes the review of the solar radiation parameterization in the sea ice component of CCSM3. This parameterization is a good first step in describing solar radiation interaction with snow, bare sea ice and (implicitly) melt ponds. As shown in this section however, the parameterizations do not include explicit multiple scattering, and as such are prone to inconsistency and arbitrariness. It is difficult to tune such a parameterization consistently. Albedos and sea ice absorption are only approximately constrained by observations. Modifying this parameterization, for example to include absorbers such as algae, carbon soot, and sediment, would be difficult to do in a physically consistent fashion for all possible sea ice states. Improvements to the parameterization, such as snow aging, vertical gradients in snow properties and an explicit treatment of melt ponds, would be difficult to make in a general and consistent manner.

These shortcomings in the sea ice solar radiation parameterization of CCSM3 can be attributed to the absence of a treatment for the fundamental radiation physics of multiple scattering. Thus, we propose an alternative solar radiation parameterization for sea ice in CCSM, one that is fundamentally based on the radiation physics of multiple scattering. We present an overview of this alternative parameterization in the next section.

3. Overview of the Delta-Eddington Solar Radiation Treatment for Sea Ice

In this section we present a general overview of the Delta-Eddington solar radiation parameterization for computing radiative transfer in sea ice. Sections 4 and 5 outline in more detail the theory and the data for this parameterization, respectively.

We first consider the boundary conditions for the Delta-Eddington multiple scattering parameterization. The previous section noted that in CCSM, the upper boundary condition for any solar radiation parameterization at the Earth surface are the four radiation fluxes from the atmosphere (Eq. 1). This new parameterization additionally requires the solar zenith angle (in the form of the cosine solar zenith angle, μ_0), to distinguish the direct solar beam from the diffuse solar radiation. The lower boundary conditions are ocean albedos at the sea ice/ocean interface, for the visible and near-infrared bands, for both direct and diffuse radiation.

As in the atmosphere, the two spectral bands (visible and near-infrared wavelengths) are employed in this parameterization. The near-infrared band is broken into two sub-bands and albedos and fluxes are evaluated before summing to get the total near-infrared band values. Three types of sea ice surface conditions are treated: snow-covered sea ice, bare sea ice, and ponded ice. This parameterization assumes horizontal homogeneity in each of these surface conditions, thus ignoring edge effects between them.

The CCSM3 sea ice model has one snow layer overlying four sea ice layers for computing thermodynamic heat transfer (Briegleb et al. 2004). To evaluate internal radiative absorption in these layers, radiative fluxes must be evaluated at all interfaces between layers. This vertical grid structure in the present sea ice model is used for the Delta-Eddington radiative transfer with the exception that the top layer is further divided into two layers. Appendix D discusses how the Delta-Eddington solar radiation treatment can be applied to situations with different numbers of snow and sea ice layers.

Three considerations lead us to sub-dividing the top sea-ice layer: (1) observations show that sea ice roughly above freeboard is distinguished by a coarse, near-granular surface layer underlain by a denser drained layer (Light et al. in review); (2) in CCSM3 a fraction of the solar radiation absorbed in the sea ice is used for the surface energy balance calculation, and this includes absorption in snow (if present) and in an *implicit* ice surface layer; and (3) the need to account for refraction in sea ice, which normally occurs at refractive boundaries between media. It is known that dry snow is granular in structure, composed of individual snow grains, while the top several centimeters of melting sea ice often appears granular as well. As depth increases in sea ice and the ice gradually becomes more solid, at some point it possesses a refractive boundary.

For this parameterization we make *explicit* the surface absorption by breaking the top sea-ice layer into two sub-layers (see Table 1 and Fig. 1), roughly consistent with observations. We index the undivided layers as in the CCSM sea ice model (i.e. layers 2,3,4) each with

layer thickness $h_i/4$, where h_i is the total ice thickness. We term these layers “interior” (INT). The top layer is divided into two sub-layers with indices 1/4 and 3/4, where the thickness of the 1/4 layer is .05 m (Grenfell and Maykut, 1977) for ice thicker than $h_i = 1.5$ m, and $h_i/30$ for $h_i < 1.5$ m. This layer is termed the “surface scattering layer” (SSL). The second sub-layer indexed 3/4 is termed the “drained layer” (DL). The total 1/4 sub-layer and 3/4 sub-layer thickness is $h_i/4$. Since sea ice in CCSM3 can be as thin as 0.1 m, the minimum SSL layer thickness is .0033 m. For bare sea ice the radiation absorbed in the SSL is included in the surface temperature calculation. We note that a .05 m thick SSL is consistent with the length scale $l = \sqrt{kt} = .06$ m for ice thermal diffusivity $k \approx 1 \times 10^{-6} m^2 s^{-1}$ and time scale $t = 1hr$ of flux exchange with the atmosphere (Briegleb et al. 2004).

In addition to the ice layers, we add a level 0 corresponding to a layer of snow or melt pond overlying the sea ice. Analogously to sea ice, we sub-divide the snow layer overlying sea ice, based on the thermodynamic requirements of surface energy balance and finite heat capacity of snow. The snow surface scattering layer, based on thermal length scale for one hour, is taken to be .04m. When sea ice is covered with pond, the absorption in the pond layer 0 is added to the absorption in the 1/4 sea ice layer for the surface temperature calculation. This approach assumes pond has zero heat capacity and is well-mixed vertically. Multiple snow and pond layers are possible (Appendix D).

Table 1. Level Structure of the Delta-Eddington Solar Radiation Treatment. Indices based on four layer CCSM3 sea ice. h_s is snow thickness, h_p is pond thickness, and h_i is ice thickness. The 1/4 layer thickness, $h_{1/4}$, is .05m or $h_i/30$, whichever is smaller. The refractive boundary is placed at the top of the 3/4 layer, and has no physical thickness. For the case of snow covered and bare sea ice, the refractive boundary is as shown, while in the case of pond over sea ice, the refractive boundary is placed at the top of layer 0, i.e. at the top of the pond. SSL thickness limited to half the layer thickness as appropriate.

Level	Media	Thickness
0 (SSL)	Snow or Pond	$h_{SSL} = .04$ m or $h_s, h_p/2$
0 (INT)	Snow or Pond	$h_s, h_p - h_{SSL}$
1/4 (SSL)	Sea Ice Surface Scattering Layer	.05 m (or $h_i/30$) = $h_{1/4}$
3/4 (DL)	Refractive Boundary	none
	Sea Ice Drained Layer	$h_i/4 - h_{1/4}$
2 (INT)	Sea Ice Interior	$h_i/4$
3 (INT)	Sea Ice Interior	$h_i/4$
4 (INT)	Sea Ice Interior	$h_i/4$

This parameterization is designed to accommodate thick as well as thin sea ice. Table 1 shows that the SSL remains at 5 cm for all sea ice thicker than 1.5 m, while for sea ice of

thickness less than 1.5 m, the SSL is a fixed fraction of total sea ice thickness ($h_i/30$, Table 1 and Fig. 1). Perovich et al. (2002) discuss how despite considerable surface ablation during the summer, a SSL is maintained. This parameterization thus assumes that ice thinner than 1.5 m maintains a SSL with thickness a fixed fraction of total sea ice thickness and therefore freeboard. A vertically weighted mean density (from Table 9) is 0.888 Mg m^{-3} , which implies a freeboard of $.112h_i$. Thus, we assume that the SSL maintains a constant fraction (about 30%) of ice freeboard for ice thinner than 1.5 m. Note that the specific fraction ($1/30$) of h_i for thin ice SSL thickness was chosen to give the best agreement with limited observations (see section 6.2). The DL on the other hand, for a four evenly-spaced sea ice model as CCSM3, has a thickness for ice thinner than 1.5 m of $h_i/4 - h_i/30$, or $.217h_i$, which is nearly twice freeboard (see Fig. 1).

We associate inherent optical properties (IOPs) to the snow layer, to pond water, and to each sea ice layer. These IOPs are extinction coefficient k , single scattering albedo ω , and asymmetry parameter g . They are considered vertically and horizontally uniform throughout each layer shown in Table 1 and Fig. 1. The extinction coefficient k (m^{-1}) is a measure of the total scattering and absorption occurring within each layer. Its inverse ($1/k$) is a typical length scale of radiation propagation in the layer before scattering and/or absorption occurs. The single scattering albedo ω is the probability that a single event results in scattering (verses absorption), ranging from 0 to 1. The asymmetry parameter g is the integrated cosine weighted phase function, ranging from -1 to +1. It is a measure of the scattering asymmetry, where -1 is complete backscattering, 0 is equal backward and forward, and +1 is complete forward scattering.

The IOPs for snow and sea ice are derived from information about the shape, number, and size of ice grains (snow) and brine, gas, and precipitated salts (sea ice). For snow, Flanner and Zender (2006) and Grenfell and Warren (1999) note that ice media of non-spherical particles, for hemispheric flux calculation within 5% accuracy, can be represented by a collection of ice spheres that conserves total volume and surface area regardless of snow crystal habit. Furthermore, realistic particle size distributions about an effective radius have minimal impact on fluxes compared to mono-disperse (i.e. single size) distributions (Mark Flanner, personal communication). Thus, we compute snow IOPs assuming snow grains can be modeled as ice spheres of equivalent radii from $5\mu\text{m}$ to $2500\mu\text{m}$. For bare and ponded sea ice, temperature dependent changes in the ice density, salinity, and brine volume are not considered. Instead, we make use of well-observed SHEBA bare ice and ponded ice cases, and infer IOPs from surface spectral albedo observations and a structural-optical model (Light et al. 2004).

We assume that snow covers sea ice until snow depth is less than .03 m. For snow depth less than .03 m, we assume a fractional snow coverage proportional to the snow depth (Allison et al. 1993, Brandt et al. 2005). When snow melts completely, bare sea ice and melt ponds are uncovered (Perovich et al. 2002). Pond areal fraction and pond depth are required to

complete the radiative transfer calculation (see Fig. 2).

We use the same two spectral bands required by the atmospheric component of CCSM. The wavelength boundaries are: $0.2 - 0.7 \mu\text{m}$ and $0.7 - 5.00 \mu\text{m}$ for the visible and near-infrared bands, respectively. To better resolve changing IOPs from the visible to the near-infrared, we break the near-infrared band into two sub-bands of wavelengths $0.7 - 1.19$ and $1.19 - 5.0 \mu\text{m}$. We use a relation between the direct and diffuse near-infrared solar radiation to partition the near-infrared solar fluxes received from the atmosphere into these two sub-bands. Once the sub-band albedos and fluxes are computed, they are summed with the same partition to obtain the $0.7 - 5.0 \mu\text{m}$ band values to return to the atmosphere. Subdividing the near-infrared band in this way allows better resolution of the penetration of near-infrared radiation below the snow-covered and bare sea ice surfaces, particularly for thin snow and sea ice.

To account for the strong forward scattering in snow and sea ice, we use the Delta-Eddington method (Joseph et. al 1976). This method assumes the strong forward scattering peak can be represented as a δ -function, which allows a scaling of the radiative transfer equation. Once scaled, the resulting transfer equation can be solved by the usual Eddington approximation (Shettle and Weinman, 1970).

The Delta-Eddington solar radiation solution proceeds as follows. Given the incident spectral fluxes (Eq. 1), the solar zenith angle, the spectral reflectivities of the underlying ocean, IOPs and layer structure for the snow/ice/pond system, the Delta-Eddington multiple scattering solution is evaluated for each layer. We compute the reflectivities and transmissivities of the refractive boundary separately. The layer reflectivities and transmissivities of direct and diffuse radiation are then combined between layers assuming scattered radiation between layers is diffuse. In this solution, we allow for the effects of refraction in ice and melt ponds. Once all layers are combined, up- and down-welling fluxes, reflectivities, internal absorption and transmittance can be evaluated.

The final spectral albedos and fluxes are computed by weighting the results by the fractional coverage of the surfaces types:

$$1 = f_s + f_i + f_p \quad (17)$$

$$\alpha = \alpha_s f_s + \alpha_i f_i + \alpha_p f_p \quad (18)$$

$$F = F_s f_s + F_i f_i + F_p f_p \quad (19)$$

where f_s is the horizontal coverage of snow over sea ice, f_i is the horizontal coverage of bare sea ice, f_p the horizontal coverage of melt ponds (for which the ponds completely cover underlying sea ice; see Fig. 2), α is the total albedo and $\alpha_s, \alpha_i, \alpha_p$ albedos of snow-covered, bare and ponded ice respectively, and F_s, F_i, F_p are the analogous fluxes. These albedos and fluxes are computed for each thickness category and aggregated for grid-box albedos and fluxes as in CCSM3. Table 2 summarizes the Delta-Eddington solar radiation treatment.

Table 2. Summary of the Delta-Eddington Solar Radiation Treatment in Sea Ice

Symbol	Description	Units
Atmospheric Input		
F_{SWvsdr}	visible band direct downwelling shortwave	W m^{-2}
F_{SWvsdf}	visible band diffuse downwelling shortwave	W m^{-2}
F_{SWnidr}	near infrared band direct downwelling shortwave	W m^{-2}
F_{SWnidf}	near infrared band diffuse downwelling shortwave	W m^{-2}
μ_0	cosine solar zenith angle	none
Oceanic Input		
α_o	ocean band direct and diffuse albedos	fractions (0 to 1)
Sea Ice Component Input		
h_s	snow thickness	m
ρ_s	snow density	kg m^{-3}
r_s	snow grain radius	m
h_i	sea ice thickness	m
f_p	pond fractional horizontal coverage	fraction
h_p	pond depth	m
Inherent Optical Property (IOP) Specification		
$k_s \ \omega_s \ g_s$	snow IOPs from ρ_s and r_s	m^{-1} , fractions
$k_p \ \omega_p \ g_p$	pond water IOPs	m^{-1} , fractions
$k_i \ \omega_i \ g_i$	sea ice IOPs for bare ice and under-pond ice	m^{-1} , fractions
Delta-Eddington Treatment Solution		
τ	if $h_s > 0.03$ m, $f_s = 1$: snow over sea ice if $h_s < 0.03$ m, $f_s = h_s/0.03\text{m}$: snow and sea ice if $h_s = 0$: bare sea ice ($1 - f_p$) and ponded sea ice (f_p) optical depths from $k_s, k_p, k_i, h_s, h_i, h_p$ layer by layer, then inter-layer multiple scattering	none
Apparent Optical Property (AOP) Output		
α_{vsdr}	albedo (visible, direct)	fraction (0 to 1)
α_{vsdf}	albedo (visible, diffuse)	fraction (0 to 1)
α_{nidr}	albedo (near infrared, direct)	fraction (0 to 1)
α_{nidf}	albedo (near infrared, diffuse)	fraction (0 to 1)
F_{SWsrf}	shortwave absorbed at the surface	W m^{-2}
Q_{SW}	shortwave absorbed in each layer	W m^{-2}
F_{SWo}	shortwave transmitted to ocean	W m^{-2}

4. Delta-Eddington Solar Radiation Treatment: Theory

In this section, we present in detail the Delta-Eddington solar radiation treatment outlined in the previous section, focusing on the formal theory. Sections 4.1 through 4.4 treat the solution band by band with fluxes normalized to unity. Refraction is treated in section 4.1, single scattering in 4.2, multiple scattering within a layer in 4.3, and multiple scattering between layers in 4.4. In section 4.5 the apparent optical properties (AOPs) of albedo, absorbed and transmitted flux are presented, scaled by the surface fluxes from the atmosphere. The inherent optical properties (IOPs) required for these calculations are presented in section 5.

4.1 Refraction

The general Delta-Eddington formulation does not explicitly include the effects of refraction. Because refractive boundaries exist when air (index of refraction $n = 1.0$), snow ($n = 1.0$), pond ($n = 1.31$) and ice ($n = 1.31$) layers exist in the domain, special accommodation must be made in the treatment. The penetration of light across a refractive boundary from a medium with low n to a medium with high n (e.g. air into ice or pond) produces three effects that must be accounted for: (1) the bending of downward propagating solar radiation (both direct and diffuse) into the normal direction, (2) the reflection of downward propagating solar radiation at the refractive boundary, and (3) the reflection and transmission of multiply scattered upwelling radiation from below the refractive boundary. The last effect refers to solar radiation that originally transmitted the refractive boundary only to be backscattered into the upward hemisphere and reach the refractive boundary from below.

Because the effects of refraction occur at the boundary between two distinct media, we will add an extra refractive boundary layer to handle refraction effects at the appropriate interfaces. We will refer to this refractive boundary layer as a “Fresnel layer”, to honor the scientist who made much contribution to understanding refraction effects, and sometimes simply as the refractive boundary; see Fig. 3. This Fresnel layer is an extra *radiative* layer in addition to those required by the sea ice thermodynamics. For each type of sea ice considered (ice with and without snow cover, and ponded ice; see Fig. 2), only one Fresnel layer is required, as we assume only two indices of refraction ($n = 1$ and $n = 1.31$). For sea ice with and without snow cover, the refractive boundary could be at the air/snow and sea ice interface. However, as noted previously, snow is granular and non-refractive, and sea ice typically has a granular and porous SSL. We therefore place the refractive boundary *between* the SSL and the remainder of the top sea ice thermodynamic layer (i.e. at the 1/4, 3/4 interface- see Table 1 and Fig. 3). For ponds we place the Fresnel layer at the *top* water surface.

Let us now represent the three basic effects of refraction mentioned above for the refractive boundary, here treated as a Fresnel layer.

The refraction of radiation at cosine zenith angle μ incident upon a medium of refractive index $n > 1$ (relative to air) is given by Snell's Law (angles are referred against the normal to the layer, with cosine solar zenith angle $\mu = -1$ vertically upwards and $\mu = +1$ vertically downwards, see Fig. 3):

$$\mu_n = \sqrt{1 - (1 - \mu^2)/n^2} \quad (20)$$

where μ_n is the cosine zenith angle of the refracted radiation. Eq. 20 is valid for both direct and diffuse solar radiation. For the direct solar beam in air at cosine solar zenith angle μ_0 , the cosine solar zenith angle in pond water and in sea ice below the refractive boundary is: $\mu_{0n} = \sqrt{1 - (1 - \mu_0^2)/n^2}$, where n is the index of refraction of water or sea ice relative to air.

As will be discussed in Sections 4.3 and 4.4, each snow, pond or sea ice layer is characterized by a reflectivity (R) and transmissivity (T) of the entire layer to direct and diffuse radiation incident on both upper and lower layer boundaries. This characterization is also necessary for the Fresnel layer that represents refraction. As the atmospheric component of CCSM3 treats only unpolarized solar radiation, we do so here as well. We use formulas known as the ‘‘Fresnel formulas’’ for R and T for direct beam polarized radiation at a plane-parallel refractive boundary, but combine planes of polarization equally so the expressions are appropriate for unpolarized radiation. We assume that incident solar radiation is unpolarized and that radiation transmitted through the refractive boundary and scattered is also unpolarized. Thus, the reflectivity and transmissivity for unpolarized radiation from above are (Liou, 1980):

$$\begin{aligned} R_f(\mu) &= \frac{1}{2}(R_1^2 + R_2^2) \\ T_f(\mu) &= \frac{1}{2}(T_1^2 + T_2^2) \quad n\mu_n/\mu \end{aligned} \quad (21)$$

where $R_f(\mu) + T_f(\mu) = 1$ (i.e. the refractive boundary is nonabsorbing), the subscript ‘‘f’’ refers to the Fresnel layer, and R_1, T_1 and R_2, T_2 are reflection/transmission amplitude factors for polarizations perpendicular (1) and parallel (2) to the plane containing the incident, reflected and refracted beams, respectively (Liou, 1980). For incident radiation at cosine zenith angle μ refracted into μ_n , the Fresnel formulas for R and T are:

$$\begin{aligned} R_1 &= \frac{\mu - n\mu_n}{\mu + n\mu_n} \\ R_2 &= \frac{n\mu - \mu_n}{n\mu + \mu_n} \\ T_1 &= \frac{2\mu}{\mu + n\mu_n} \\ T_2 &= \frac{2\mu}{n\mu + \mu_n} \end{aligned} \quad (22)$$

The reflectivity and transmissivity for diffuse unpolarized radiation from above (a) can be computed by integrating $R_f(\mu)$ in Eq. 21 for all angles in the downward hemisphere using

the isotropic diffuse assumption:

$$\begin{aligned}\overline{R}_{fa} &= \int_0^{+1} \mu R_f(\mu) d\mu / \int_0^{+1} \mu d\mu \\ \overline{T}_{fa} &= 1 - \overline{R}_{fa}\end{aligned}\tag{23}$$

where the nonabsorbing nature of the refractive boundary is used to evaluate \overline{T}_{fa} . Note that in reality, even atmospheric diffuse radiation has angular dependence (i.e. it is not generally isotropic in the downward hemisphere). However, the atmospheric component in CCSM provides only direct and diffuse fluxes, where the latter must be assumed to be isotropic. We compute normalized fluxes in the vertical direction only, therefore requiring the extra μ projection factor in the integrands for the R.H.S. \overline{R}_{fa} integrals in Eq. 23.

The reflectivity for diffuse radiation from below (b) must take account of total internal reflection. This arises since only a cone of angles, around the normal direction for upward multiply scattered radiation below the refractive boundary, can be transmitted upward through the boundary. In keeping with our assumption of depolarization upon scattering below the Fresnel layer, we assume that upwelling radiation is unpolarized. We have:

$$\begin{aligned}\mu &= \sqrt{1 - n^2(1 - \mu_n^2)} \\ \overline{R}_{fb} &= \{ \int_{-1}^{-\mu_c} \mu_n R_f(\mu_n) d\mu_n + \int_{-\mu_c}^0 \mu_n d\mu_n \} / \int_{-1}^0 \mu_n d\mu_n \\ \overline{T}_{fb} &= 1 - \overline{R}_{fb} \\ \mu_c &= \sqrt{1 - (1/n^2)}\end{aligned}\tag{24}$$

where from Snell's Law the critical cosine zenith angle for complete internal reflection is μ_c , and the integrals are evaluated for the upward hemisphere.

We need to specify the index of refraction for both pond water and sea ice, noting that in general it varies with wavelength. For pure ice at visible wavelengths (see section 5.1, $0.35-0.70\mu m$) n ranges from 1.325 to 1.307. For ice at near-infrared wavelengths ($0.70-1.19\mu m$), n ranges from 1.307 to 1.298. For ice in wavelengths ($1.19-5.00\mu m$), n ranges from 0.96 to 1.65 (Warren, 1984). For pure water at visible wavelengths ($0.35-0.70\mu m$), the index of refraction ranges from 1.343 to 1.331, and for the near-infrared wavelengths ($0.70-1.19\mu m$) from 1.331 to 1.327 (Paltridge and Platt, 1976). We note that the variations of index of refraction with wavelength between ice and water are relatively small. Therefore, we assume $n = 1.31$ for all wavelengths for both pond water and sea ice. This means that we assume no refraction effects at water-ice boundaries.

To evaluate the angular integrals in Eqs 23 and 24, we use gaussian integration, increasing the number of angles employed until convergence ($< .001$ change with increasing number of angles) is obtained. While the diffuse reflectivity from above (Eq. 23) converges quickly for a small number of angles (32), the diffuse reflectivity from below (Eq. 24) requires

many more (512) to resolve total internal reflection. The final values are:

$$\begin{aligned}
\overline{R}_{fa} &= 0.063 \\
\overline{T}_{fa} &= 0.937 \\
\overline{R}_{fb} &= 0.455 \\
\overline{T}_{fb} &= 0.545
\end{aligned} \tag{25}$$

The contrast between \overline{R}_{fa} and \overline{R}_{fb} occurs because light emerging from a medium of relatively high n into a medium of relatively low n experiences total internal reflection. The refractive boundary is thus much more transmissive to downward diffuse radiation from above than it is to upward diffuse radiation from below.

4.2 Single Scattering

Snow and sea ice scatter solar radiation: in the case of snow, individual snow grains, and in the case of sea ice, air bubble, brine pocket, precipitated salt, and inorganic/organic inclusions. We assume these grains and inclusions are sufficiently separated from one another so that each scattering event from a single scatterer can be individually characterized. We are assuming here that both snow and sea ice above the 1/4, 3/4 interface consist of granular scatterers separated by air, while below the 1/4, 3/4 refracting boundary the scatterers are embedded (or included) within solid sea ice, yet still separated from one another (see Table 1). As will be discussed further in section 5.3, the solid sea ice assumed below the 1/4, 3/4 interface does not itself scatter very much, yet it contains the embedded scatterers just mentioned. As discussed in the previous section, refraction at the 1/4, 3/4 interface bends the direct solar beam in the solid sea ice, and affects radiation propagating across it (both upward and downward), but the single and multiple scattering above and below the refractive boundary can be treated similarly.

The angular pattern of single scattering is described by the scattering phase function P , which is the fraction of radiation incident from direction $\hat{\Omega}$ that is scattered into direction $\hat{\Omega}'$:

$$\begin{aligned}
P &= P(\hat{\Omega}, \hat{\Omega}') \\
\hat{\Omega} &= (\sin \theta \cos \phi, \sin \theta \sin \phi, \cos \theta) \\
\hat{\Omega}' &= (\sin \theta' \cos \phi', \sin \theta' \sin \phi', \cos \theta')
\end{aligned} \tag{26}$$

where $\hat{\Omega}, \hat{\Omega}'$ are the normalized direction vectors for the incoming and scattered beams, respectively, with θ the zenith angle and ϕ the azimuth angle. The angles θ and ϕ are measured relative to an xyz orthogonal coordinate system with the xy plane the Earth's horizontal plane and the z axis perpendicular towards the zenith. The zenith angle θ is measured from the zenith (i.e. downward from the z axis) and ϕ from an arbitrary axial orientation of the xy axes. The scattering phase function is normalized over all scattering angles:

$$\frac{1}{4\pi} \int_{4\pi} d\Omega' P(\hat{\Omega}, \hat{\Omega}') = 1 \tag{27}$$

where the differential solid angle $d\Omega' = \sin\theta' d\theta' d\phi'$. We assume that the scattering is axially symmetric. This does not necessarily require that scatterers are treated as equivalent spheres, but only that on the average the scattering is axisymmetric. Hence:

$$P(\hat{\Omega}, \hat{\Omega}') = P(\hat{\Omega} \cdot \hat{\Omega}') = P(\Theta) \quad (28)$$

where $\hat{\Omega} \cdot \hat{\Omega}' = \cos\Theta$ and Θ is the scattering angle measured from the incident direction. The normalization condition for the axially symmetric scattering phase function becomes:

$$\frac{1}{2} \int_{-1}^{+1} d(\cos\Theta) P(\cos\Theta) = 1 \quad (29)$$

where positive Θ refers to forward scattering, negative to backward scattering. Any axially symmetric scattering phase function can be written as a series of Legendre polynomials as:

$$P(\cos\Theta) = \sum_{l=0}^{\infty} \omega_l P_l(\cos\Theta) \quad (30)$$

where $P_l(\cos\Theta)$ is the l^{th} Legendre polynomial, normalized so that:

$$\int_{-1}^{+1} P_l(\cos\Theta) P_m(\cos\Theta) d(\cos\Theta) = \frac{2}{2l+1} \delta_{lm} \quad (31)$$

It is very useful to characterize single scattering by its asymmetry (forward vs. backward) and by the amount scattered into the forward direction. Two lowest moments of the scattering phase function allow such characterization:

$$\begin{aligned} g &= \frac{1}{2} \int_{-1}^{+1} P_1(\cos\Theta) P(\cos\Theta) d(\cos\Theta) \\ f &= \frac{1}{2} \int_{-1}^{+1} P_2(\cos\Theta) P(\cos\Theta) d(\cos\Theta) \end{aligned} \quad (32)$$

where g is the asymmetry parameter, f is the forward scattered fraction, with $P_1(\cos\Theta) = \cos\Theta$ and $P_2(\cos\Theta) = (1/2)(3[\cos\Theta]^2 - 1)$. For example, if the scattering is isotropic (i.e. equal probability in all directions), then $P(\cos\Theta) = 1$ which means $g = f = 0$, so there is uniform symmetry to the scattering ($g = 0$) and no preference for forward scattering ($f = 0$).

Many realistic scattering phase functions are strongly forward peaked, as scattering particles are usually much larger than typical solar radiation wavelengths. For instance, Light et al. (2003a) report air bubble radii from $4\mu m$ to $2000\mu m$, salt crystals $10\mu m$, and equivalent spherical radii for brine inclusions of 5 to $150\mu m$, all well above the $0.2\mu m$ to $5.0\mu m$ wavelengths of scattering solar radiation, while in snow Wiscombe and Warren (1980) use grain radii from $5\mu m$ to $2500\mu m$. An axially symmetric function that can empirically represent many such scattering phase functions is the Henyey-Greenstein function (Henyey and Greenstein, 1941):

$$P_{HG}(\cos\Theta) = \frac{1 - g_{HG}^2}{(1 + g_{HG}^2 - 2g_{HG} \cos\Theta)^{\frac{3}{2}}} \quad (33)$$

where $g_{HG} < 1$ is the asymmetry parameter indicating the amount of forward scattering, which ranges from greater than -1 (completely backward) to less than $+1$ (completely forward). We can see this from the Legendre polynomial expansion of Eq. 33:

$$P_{HG}(\cos\Theta) = \sum_{l=0}^{\infty} (2l+1)g_{HG}^l P_l(\cos\Theta) \quad (34)$$

Using Eqs. 31, 32 and 34, we can show that $g = g_{HG}$ and $f = g_{HG}^2$. We will not explicitly use the Henyey-Greenstein phase function, other than to note that it represents realistic scattering phase functions specified by the asymmetry parameter and that its forward scattering fraction is the square of the asymmetry parameter.

In the Eddington approximation for multiple scattering (see the following section), one truncates the scattering phase function (Eq. 34) at its first moment:

$$P(\cos\Theta) \approx 1 + 3g^* \cos\Theta \quad (35)$$

where $P_1(\cos\Theta) = \cos\Theta$, and g^* is yet to be related to the asymmetry parameter g . However, such a smooth scattering phase function cannot represent the strong forward peak in realistic scattering. If the strong forward peak is represented by a δ -function, then one can form a modified phase function by including the forward scattering fraction f as in:

$$P(\cos\Theta) = af\delta(1 - \cos\Theta) + b(1 - f)(1 + 3g^* \cos\Theta) \quad (36)$$

so that any radiation not forward scattered as represented by the δ function is smoothly scattered as represented by the truncated series, where a, b are normalization constants. From normalization (Eq. 29) one can show that $a = 2$ and $b = 1$, and by direct calculation (Eq. 32) the asymmetry parameter is:

$$g = f + (1 - f)g^*$$

so that:

$$g^* = \frac{g - f}{1 - f} \quad (37)$$

We are assuming horizontal uniformity in the snow, sea ice and pond surfaces, and are interested in radiant energy flows perpendicular to these surfaces. Since we are also assuming axial symmetry in single scattering, then only the azimuthal average of intensity (see next section) needs to be calculated. Therefore, we compute the azimuthal average about the z axis of the scattering phase function Eq. 36. To do so, we express the scattering angle Θ in terms of the angles θ and ϕ by using $\delta(1 - \cos\Theta) = 2\pi\delta(\mu - \mu')\delta(\phi - \phi')$ and the expansion of $\hat{\Omega} \cdot \hat{\Omega}'$ in terms of $(\mu, \phi), (\mu', \phi')$ (e.g. Eqs 26, 28). This results in the Delta-Eddington azimuthally averaged scattering phase function $P_{\delta E}(\mu)$:

$$P_{\delta E}(\mu) = \frac{1}{2\pi} \int_0^{2\pi} d\phi' P(\mu, \phi; \mu', \phi') = \frac{1}{2\pi} \int_0^{2\pi} d\phi' [2f(2\pi\delta(\mu - \mu')\delta(\phi - \phi')) + (1 - f)(1 + 3g^*(\mu\mu' + \sqrt{1 - \mu^2}\sqrt{1 - \mu'^2}\cos(\phi' - \phi)))]$$

$$P_{\delta E}(\mu) = 2f\delta(\mu - \mu') + (1 - f)(1 + 3g^*\mu\mu') \quad (38)$$

where δE refers to “Delta-Eddington”. This scattering phase function will be used to calculate multiple scattering within a layer as presented in the next section.

4.3 Multiple Scattering Within a Layer

Variations in snow, sea ice and melt pond properties, that determine the transfer of solar radiation, occur both vertically and horizontally. The most important variations are vertical, as snow and ice form stratified layers approximately parallel to the ocean surface. Horizontal variations are most important for patchy snow, for melt ponds and for ridged sea ice. Typical radiance attenuation coefficients resulting from multiple scattering (which characterize the variation of in-snow/sea ice mean intensity) are order 1 to 2 m^{-1} (see sections 5 and 6), which implies radiance variations over a meter or so both vertically and horizontally. When significant scattering occurs, radiation can propagate horizontally by several meters, and so edge effects can potentially be important for patchy snow and melt ponds. Such lateral spreading can also smooth out horizontal variations in scattering from inhomogeneities in sea ice. In any case, we assume horizontal homogeneity and explicitly solve only for vertical variations in IOPs. We represent vertical variations in the sea ice column by a series of layers, each of which is assumed to be vertically homogeneous (see Figs. 1 and 2).

Our approach to the multiple scattering problem is to separate the layer multiple scattering solution from the inter-layer scattering. In other words, assuming horizontal and vertical homogeneity within each layer, and given the IOPs necessary to define the single scattering properties, then the entire single layer multiple scattering problem can be evaluated explicitly using the Delta-Eddington approximation. We then combine each layer solution to allow for multiple scattering between layers. In this section, we treat multiple scattering within a single layer, while in the next section we describe inter-layer scattering.

We consider each layer to be both absorbing and scattering. We specify the absorbing and scattering properties of each layer in terms of an absorption coefficient κ and a scattering coefficient σ , whose sum is the extinction coefficient $k = \kappa + \sigma$. The single scattering albedo is the ratio of scattering to extinction, or $\omega = \sigma/(\kappa + \sigma)$, and the degree of forward/backward single scattering is given by the asymmetry parameter g (see the previous subsection). These last three properties (k, ω, g) are the inherent optical properties (IOPs) of the layer. The specification of snow, sea ice and pond water IOPs is presented in section 5.

The radiative transfer equation for the plane-parallel, horizontally homogeneous scattering and absorbing layer is:

$$\mu \frac{dI}{d\tau} + I = \frac{\omega}{4\pi} \int_{4\pi} d\Omega' P(\Omega, \Omega') I(\Omega', \tau) \quad (39)$$

with extinction optical depth of $\tau = 0$ at the layer upper boundary and $\tau = \tau_0$ at the lower layer boundary, with $\tau_0 = kz$, k is the extinction coefficient and z is the layer thickness,

$\mu = \cos\theta$ defined as positive for downward directed radiation and negative for upward directed radiation, I the intensity (or radiance), ω the single particle scattering albedo ($0 \leq \omega < 1$), P the scattering phase function, and Ω the solid angle defined by the normalized direction vector. The intensity I represents the radiant energy per unit cross sectional area, per unit solid angle, and per unit time in a particular location and direction for each wavelength band. The radiative transfer equation (Eq. 39) states that variations in intensity (or radiance) in a direction μ at optical depth τ follow from losses due to extinction (the L.H.S.), and from gains due to multiply scattered radiation into the direction μ (the R.H.S.). It is simply a statement of energy conservation.

The intensity in Eq. 39 is a function of both angles θ and ϕ , but it is only the θ dependence that contributes to the flow of radiant energy perpendicular to the Earth's surface (see Eqs. 49 and A2). Therefore we take the azimuthal average of the transfer equation (Eq. 39) and denote the azimuthal average of the intensity $I(\mu, \tau)$:

$$\mu \frac{dI(\mu, \tau)}{d\tau} + I(\mu, \tau) = \frac{\omega}{2} \int_{4\pi} d\mu' \left\{ \frac{1}{2\pi} \int_0^{2\pi} P(\Omega, \Omega') d\phi' \right\} I(\mu', \tau) \quad (40)$$

Substituting the azimuthally averaged Delta-Eddington phase function (Eq. 38) of the previous section for the bracketed term and rearranging:

$$\begin{aligned} \mu \frac{dI}{d\tau} + I &= \frac{\omega}{2} \int_{-1}^{+1} d\mu' \{P_{\delta E}(\mu)\} I(\mu', \tau) \\ \mu \frac{dI}{d\tau} + I &= \frac{\omega}{2} \int_{-1}^{+1} d\mu' \{2f\delta(\mu - \mu') + (1-f)(1+3g^*\mu\mu')\} I(\mu', \tau) \\ \mu \frac{dI}{d\tau} + I &= \omega f I + \frac{\omega(1-f)}{2} \int_{-1}^{+1} d\mu' (1+3g^*\mu\mu') I(\mu', \tau) \\ \mu \frac{1}{1-\omega f} \frac{dI}{d\tau} + I &= \frac{\omega(1-f)}{2(1-\omega f)} \int_{-1}^{+1} d\mu' (1+3g^*\mu\mu') I(\mu', \tau) \end{aligned} \quad (41)$$

Defining the *scaled* optical properties:

$$\begin{aligned} \tau^* &= (1-\omega f)\tau \\ \omega^* &= \frac{(1-f)\omega}{1-\omega f} \\ g^* &= \frac{g-f}{1-f} \end{aligned} \quad (42)$$

along with:

$$f = g^2 \quad (43)$$

then allows us to write a *scaled* radiative transfer equation:

$$\mu \frac{dI}{d\tau^*} + I = \frac{\omega^*}{2} \int_{-1}^{+1} d\mu' (1+3g^*\mu\mu') I(\mu', \tau^*) \quad (44)$$

Thus, we have removed the forward scattering peak by scaling the transfer equation to a more soluble one. In effect, we have replaced the original transfer equation (Eq. 39)

with a *scaled* transfer equation (Eq. 44) that has less optical depth ($\tau^* < \tau$), less forward scattering ($g^* = \frac{g-f}{1-f} = \frac{g}{1+g} < g$), but the same layer absorption ($\tau^*(1 - \omega^*) = \tau(1 - \omega)$). Given the original extinction optical depth τ , single scattering albedo ω , asymmetry parameter g and forward scattering fraction $f = g^2$, we can define the scaled optical properties and associated scaled transfer equation.

A common technique in radiative transfer is to distinguish the direct solar beam from multiply scattered radiation, and embed the former directly into the transfer equation as a source term. Since we know the solar beam direction and that it is extinguished according to Beer's law through the layer, we then express the intensity as $I \Rightarrow I + I_s$, with the diffuse (i.e. multiply scattered) intensity I and the direct beam solar intensity I_s , the latter given by:

$$I_s = \frac{1}{2} F_0 \delta(\mu - \mu_{0n}) e^{-\tau^*/\mu_{0n}}, \quad \mu_{0n} > \mu_c \quad (45)$$

where πF_0 is the solar flux in the beam direction, μ_{0n} is the solar beam direction in the media of index of refraction $n \geq 1$, and μ_c is the critical cosine solar zenith angle for complete internal reflection. Eq. 45 is applicable for both air above the sea ice system, as well as within snow and sea ice SSL *and* the solid sea ice below the refractive boundary. In the former, $n = 1$, $\mu_{0n} = \mu_0$, the cosine solar zenith angle in the atmosphere and surface *above* the refractive boundary, and $\mu_c = 0$, while in the latter $n = 1.31$, μ_{0n} is the cosine solar zenith angle of the direct beam *below* the refractive boundary, given by Eq. 20, and μ_c is given by Eq. 24. The downward flux F_s of solar radiation is thus:

$$F_s = 2\pi \int_0^{+1} \mu I_s d\mu = 2\pi \left(\frac{1}{2} F_0\right) \int_0^{+1} \mu \delta(\mu - \mu_{0n}) e^{-\tau^*/\mu_{0n}} d\mu = \pi F_0 \mu_{0n} e^{-\tau^*/\mu_{0n}} \quad (46)$$

Separating the direct solar beam from the diffuse intensity ($I \Rightarrow I + I_s$), and using Eq. 45 for I_s , Eq. 44 becomes:

$$\mu \frac{dI}{d\tau^*} + I = \frac{\omega^*}{2} \int_{-1}^{+1} (1 + 3g^* \mu \mu') I d\mu' + \frac{\omega^* F_0}{4} (1 + 3g^* \mu_{0n} \mu) e^{-\tau^*/\mu_{0n}} \quad (47)$$

where the direct beam solar now appears as a single scattered source for diffuse radiation (second term R.H.S. of Eq. 47). We note in passing that if we were solving the entire column radiative transfer equation across the refractive boundary, it would be necessary to include a factor μ_0/μ_{0n} in the solar beam source term for energy conservation. However, as we are only solving the transfer equation layer by layer, we need only account for the change in solar beam direction and transmission through the refractive boundary to insure energy is conserved.

Now we invoke the Eddington approximation: $I = I_0 + \mu I_1$, where I_0 is the mean intensity:

$$I_0 = \frac{1}{4\pi} \int_{4\pi} I d\Omega = \frac{1}{2} \int_{-1}^{+1} I(\mu) d\mu \quad (48)$$

and $I_1/3$ is the mean flux:

$$I_1/3 = \frac{1}{4\pi} \int_{4\pi} \mu I d\Omega = \frac{1}{2} \int_{-1}^{+1} \mu I(\mu) d\mu \quad (49)$$

The Eddington approximation is accurate only when the radiation field due to multiple scattering is very diffuse (i.e. the second R.H.S. term of Eq. 47 is small and layer optical depth $\tau_0 \gg 1$), or when little multiple scattering occurs (i.e. $\tau_0 < 1$), and the first R.H.S. term of Eq. 47 is small compared to the second R.H.S. term.

We briefly outline the solution to the transfer equation (Eq. 47); for further details, see Appendix A. We substitute the Eddington approximation into the radiative transfer equation and take moments $\int_{-1}^{+1} d\mu$, $\int_{-1}^{+1} \mu d\mu$ which yields two first order coupled differential equations for the mean intensity and mean flux (Eqs. 48 and 49). We then take optical depth derivative of each equation to eliminate the first derivative terms, yielding two second order inhomogeneous differential equations; $F_0 = 0$ yields the homogeneous differential equations. General solutions to both homogeneous and inhomogeneous equations can then be written down, with constants determined from the boundary conditions. Differences and sums of the mean intensity and mean flux yield the up flux (upward hemisphere) and down flux (downward hemisphere), respectively, which allow the boundary conditions to be set for the case of direct solar beam and no diffuse flux. Finally, the layer reflectivity and transmissivity for both direct incident radiation and diffusely incident radiation can be evaluated, which completes the solution.

We summarize the solution as follows. For direct radiation at cosine zenith angle μ_{0n} incident on a layer of thickness z and inherent optical properties of absorption coefficient κ , scattering coefficient σ , and single particle scattering asymmetry parameter g , the solution

equations (following the notation of Coakley et. al 1983) are given by:

$$\begin{aligned}
k &= \kappa + \sigma \\
\omega &= \sigma / (\kappa + \sigma) \\
f &= g^2 \\
\tau &= kz \\
\tau^* &= (1 - \omega f) \tau \\
\omega^* &= \frac{(1 - f) \omega}{1 - \omega f} \\
g^* &= \frac{g - f}{1 - f} \\
\lambda &= \sqrt{3(1 - \omega^*)(1 - \omega^* g^*)} \\
\alpha &= \frac{3}{4} \omega^* \mu_{0n} \left(\frac{1 + g^*(1 - \omega^*)}{1 - \lambda^2 \mu_{0n}^2} \right) \\
\gamma &= \frac{1}{2} \omega^* \left(\frac{1 + 3g^*(1 - \omega^*) \mu_{0n}^2}{1 - \lambda^2 \mu_{0n}^2} \right) \\
u &= \frac{3}{2} \left(\frac{1 - \omega^* g^*}{\lambda} \right) \\
N &= (u + 1)^2 e^{\lambda \tau^*} - (u - 1)^2 e^{-\lambda \tau^*} \\
R(\mu_{0n}) &= (\alpha - \gamma)(4u/N) e^{-\tau_0^*/\mu_{0n}} + (\alpha + \gamma)(u + 1)(u - 1) \left[e^{+\lambda \tau_0^*} - e^{-\lambda \tau_0^*} \right] / N - (\alpha - \gamma) \\
T(\mu_{0n}) &= (\alpha + \gamma)(4u/N) + (\alpha - \gamma) \left[\frac{(u + 1)(u - 1)(e^{+\lambda \tau_0^*} - e^{-\lambda \tau_0^*})}{N} \right] e^{-\tau_0^*/\mu_{0n}} \\
&\quad - (\alpha + \gamma - 1) e^{-\tau_0^*/\mu_{0n}} \\
\overline{R} &= 2 \int_0^{+1} \mu R(\mu) d\mu \\
\overline{T} &= 2 \int_0^{+1} \mu T(\mu) d\mu
\end{aligned} \tag{50}$$

where $R(\mu_{0n})$, $T(\mu_{0n})$ are the layer reflectivity and transmissivity to direct radiation respectively, and \overline{R} , \overline{T} are the layer reflectivity and transmissivity to diffuse radiation respectively. Note that these reflectivities and transmissivities account for multiple scattering within the layer. We use an explicit integration of $R(\mu)$ and $T(\mu)$, rather than closed form expressions for \overline{R} and \overline{T} , as the closed form expression for \overline{R} in particular can sometimes be negative; see Appendix A for more discussion and a table of angles and weights for the angular integration.

How accurate is the Delta-Eddington solution compared to more accurate radiative transfer solutions? In general, for optically thin layers where single scattering dominates, the reflectivities and transmissivities are quite accurate (typical errors $< .01$). For the intermediate regime of low order scattering, errors can be somewhat larger (order $.01 - .02$). For the asymptotic regime of a large number of scatterings, the errors become order $.01$ again (see Briegleb 1992). From the IOP data of section 5, we note that for snow depth more than a few cm thickness and for the ice SSL, visible optical depths (τ^*) are generally greater than

five, and therefore close to the asymptotic regime. For ice interior, the layer scattering is in the low order regime ($\tau^* \approx 1$). See section 6 for example calculations consistent with these general error estimates.

4.4 Multiple Scattering Between Layers

Once multiple scattering for each layer has been computed (Eqs. 50), multiple scattering between layers must be evaluated. We call the evaluation of inter-layer scattering the *combining* of layers. Hence, given a column of individual layer AOPs $[R(\mu) \ T(\mu) \ \bar{R} \ \bar{T}]$, representing the layer solutions (Eqs. 50), we combine layers to complete the full multiple scattering solution.

To combine layers, we consider only diffuse radiation resulting from multiple scattering within each layer (Eqs. 50, \bar{R} and \bar{T}). In other words, we account for diffuse inter-layer scattering only. This approximation of diffuse inter-layer scattering is not very accurate through the refractive boundary, reasonably accurate for optically thick snow and sea ice surface layers, but less accurate for deeper ice layers and ponds. We note also that apart from the Fresnel layer, all layers are homogeneous, meaning that the reflectivity and transmissivity formulas in Eqs. 50 are the same for radiation incident from above and from below the layer. That is no longer the case when layers are combined, so care must be taken to keep the directions consistent.

For an arbitrary homogeneous layer 1 with AOPs $[R_1(\mu) \ T_1(\mu) \ \bar{R}_1 \ \bar{T}_1]$ overlying homogeneous layer 2 with AOPs $[R_2(\mu) \ T_2(\mu) \ \bar{R}_2 \ \bar{T}_2]$, the combination formulas for direct and diffuse radiation incident from above are:

$$\begin{aligned} R_{12}(\mu) &= R_1(\mu) + \frac{\{(T_1(\mu) - Tdr_s)\bar{R}_2 + Tdr_s R_2(\mu)\}\bar{T}_1}{1 - \bar{R}_1 \bar{R}_2} \\ T_{12}(\mu) &= Tdr_s T_2(\mu) + \frac{\{(T_1(\mu) - Tdr_s) + Tdr_s R_2(\mu)\bar{R}_1\}\bar{T}_2}{1 - \bar{R}_1 \bar{R}_2} \\ \bar{R}_{12} &= \bar{R}_1 + \frac{\bar{T}_1 \bar{R}_2 \bar{T}_1}{1 - \bar{R}_1 \bar{R}_2} \\ \bar{T}_{12} &= \frac{\bar{T}_1 \bar{T}_2}{1 - \bar{R}_1 \bar{R}_2} \end{aligned} \tag{51}$$

with $Tdr_s = e^{-\tau_1^*/\mu}$ the direct solar beam transmission through layer 1, and the cosine solar zenith angle μ is μ_0 above the refractive boundary and μ_{0n} below the refractive boundary. The transmissions for each layer $[T_1(\mu_0) \ T_2(\mu_0)]$ and for the combined layers $[T_{12}(\mu_0)]$ are total transmissions, containing both direct and diffuse transmission.

To combine the layers over the entire column, two vertical passes are made, one starting from the top and proceeding downward, the other starting from the specified ocean surface reflectivities at the sea ice/ocean interface and proceeding upward. The result is that for every interface, the following combined reflectivities and transmissivities are available: Fdr_s , the direct beam flux transmission from the top to the interface, $R_{up}(\mu)$, the reflectivity

to direct solar radiation of the entire column below the interface, $T_{dn}(\mu)$, the total transmission to direct solar radiation incident from the top to the interface, \bar{R}_{up} , the reflectivity of the column below the interface to diffuse radiation from above, \bar{R}_{dn} , the reflectivity of the column above the interface to diffuse radiation from below, and \bar{T}_{dn} , the transmissivity to diffuse radiation from the top to the interface. With these quantities, the upward and downward fluxes at every interface can be computed. The resulting expressions for the downward and upward fluxes are:

$$\begin{aligned}
Fdr_{dn} &= Fdr_s + \frac{(T_{dn}(\mu) - Fdr_s) + Fdr_s R_{up}(\mu) \bar{R}_{dn}}{1 - \bar{R}_{dn} \bar{R}_{up}} \\
Fdr_{up} &= \frac{Fdr_s R_{up}(\mu) + (T_{dn}(\mu) - Fdr_s) \bar{R}_{up}}{1 - \bar{R}_{dn} \bar{R}_{up}} \\
Fdf_{dn} &= \frac{\bar{T}_{dn}}{1 - \bar{R}_{dn} \bar{R}_{up}} \\
Fdf_{up} &= \frac{\bar{T}_{dn} \bar{R}_{up}}{1 - \bar{R}_{dn} \bar{R}_{up}}
\end{aligned} \tag{52}$$

where Fdr_s is the solar beam flux that transmits from the top to the interface, and again the cosine solar zenith angle μ is μ_0 above the refractive boundary and μ_{0n} below the refractive boundary.

A complete discussion of assumptions and derivation of combination formulas for multiple scattering between layers is given in Appendix B.

4.5 Apparent Optical Properties: Albedo, Absorbed and Transmitted Flux

Given the multiple scattering solutions within and between layers presented in the previous two subsections, the apparent optical properties (AOPs) of albedo, absorbed and transmitted flux can be evaluated. The Delta-Eddington theory of the past several sections has suppressed any explicit reference to spectral band. In this subsection we make explicit the visible (*vs*) and near-infrared (*ni*) spectral bands for the albedos and fluxes. Finally, the fluxes presented in Eqs. 52 are normalized to unity, whereas here we scale these normalized fluxes by the solar radiation fluxes incident from above.

The surface albedos for direct and diffuse radiation are given by the band reflectivities $R_{up}(\mu_0)$, \bar{R}_{up} at the top interface:

$$\begin{aligned}
\alpha_{vsdr} &= R_{vsup}(\mu_0, top) \\
\alpha_{vsdf} &= \bar{R}_{vsup}(top) \\
\alpha_{nidr} &= R_{niup}(\mu_0, top) \\
\alpha_{nidf} &= \bar{R}_{niup}(top)
\end{aligned} \tag{53}$$

where we have added the spectral *vs* and *ni* to the reflectivities (see section 5.1), *up* refers to reflectivities at the surface for solar radiation from above, and where *top* is the surface of snow, bare sea ice or pond. Thus, the spectral band and total column absorption can

be evaluated as in Eqs. 10-12:

$$F_{SWvs} = F_{SWvsdr}(1 - \alpha_{vsdr}) + F_{SWvsdf}(1 - \alpha_{vsdf}) \quad (54)$$

$$F_{SWni} = F_{SWnidr}(1 - \alpha_{nidr}) + F_{SWnidf}(1 - \alpha_{nidf}) \quad (55)$$

$$F_{SW} = F_{SWvs} + F_{SWni} \quad (56)$$

The visible and near-infrared surface absorption are:

$$F_{SWvs-srf} = \{Fdr_{vsdn}(top) - Fdr_{vsup}(top)\}F_{SWvsdr} + \{Fdf_{vsdn}(top) - Fdf_{vsup}(top)\}F_{SWvsdf} \\ - \{Fdr_{vsdn}(bot) - Fdr_{vsup}(bot)\}F_{SWvsdr} + \{Fdf_{vsdn}(bot) - Fdf_{vsup}(bot)\}F_{SWvsdf} \quad (57)$$

$$F_{SWni-srf} = \{Fdr_{nidn}(top) - Fdr_{niup}(top)\}F_{SWnidr} + \{Fdf_{nidn}(top) - Fdf_{niup}(top)\}F_{SWnidf} \\ - \{Fdr_{nidn}(bot) - Fdr_{niup}(bot)\}F_{SWnidr} + \{Fdf_{nidn}(bot) - Fdf_{niup}(bot)\}F_{SWnidf} \quad (58)$$

where we have added the spectral *vs* and *ni* to the up/down direct and diffuse fluxes of Eqs. 52, *top* is the pond surface (if present) as for the albedos above, and for snow and bare sea ice *top* is the top of the SSL, while *bot* is always the bottom of the SSL (see Table 1).

The portions of absorbed flux that penetrate the SSL (Eqs. 13 and 14) are:

$$I_{0vs} = F_{SWvs} - F_{SWvs-srf} \\ I_{0ni} = F_{SWni} - F_{SWni-srf} \quad (59)$$

The INT ice flux divergences (Eq. 15) are similar to those for the SSL, except *top* is the layer top interface, and *bot* is the layer bottom interface:

$$Q_{SWvs} = \{Fdr_{vsdn}(top) - Fdr_{vsup}(top)\}F_{SWvsdr} + \{Fdf_{vsdn}(top) - Fdf_{vsup}(top)\}F_{SWvsdf} \\ - \{Fdr_{vsdn}(bot) - Fdr_{vsup}(bot)\}F_{SWvsdr} + \{Fdf_{vsdn}(bot) - Fdf_{vsup}(bot)\}F_{SWvsdf} \quad (60)$$

$$Q_{SWni} = \{Fdr_{nidn}(top) - Fdr_{niup}(top)\}F_{SWnidr} + \{Fdf_{nidn}(top) - Fdf_{niup}(top)\}F_{SWnidf} \\ - \{Fdr_{nidn}(bot) - Fdr_{niup}(bot)\}F_{SWnidr} + \{Fdf_{nidn}(bot) - Fdf_{niup}(bot)\}F_{SWnidf} \quad (61)$$

$$Q_{SW} = Q_{SWvs} + Q_{SWni} \quad (62)$$

Note that for the layer immediately under the SSL (see Table 1), the top of that layer for the flux divergence calculation is the SSL/INT interface for snow and the SSL/DL interface for sea ice, as the flux absorbed above that interface is included in the surface absorption.

The spectral fluxes absorbed in the underlying ocean are:

$$Q_{SWvs-ocn} = \{Fdr_{vsdn}(ocn) - Fdr_{vsup}(ocn)\}F_{SWvsdr} + \{Fdf_{vsdn}(ocn) - Fdf_{vsup}(ocn)\}F_{SWvsdf} \quad (63)$$

$$Q_{SWni-ocn} = \{Fdr_{nidn}(ocn) - Fdr_{niup}(ocn)\}F_{SWnidr} + \{Fdf_{nidn}(ocn) - Fdf_{niup}(ocn)\}F_{SWnidf} \quad (64)$$

$$Q_{SWocn} = Q_{SWvs-ocn} + Q_{SWni-ocn} \quad (65)$$

where *ocn* refers to the ocean/sea ice interface.

5. Delta-Eddington Solar Radiation Treatment: Data

In this section, we present the inherent optical properties (IOPs) for snow, bare sea ice and ponded ice that are required by the Delta-Eddington solar radiation treatment. For snow IOPs we follow Wiscombe and Warren (1980). For bare and ponded ice, IOPs were inferred from matching SHEBA spectral albedo data with an empirical/optical model (Light et al. 2003a, Light et al. 2004).

In section 5.1 following, we present the Delta-Eddington solar radiation spectral bands. In the next two sections 5.2 and 5.3, we present the IOP data for snow and sea ice respectively.

5.1 Spectral Bands

As noted in section 2 (Eq. 1), the boundary radiative fluxes from the atmosphere to sea ice in CCSM distinguish visible (wavelengths $< 0.7\mu m$) from near-infrared (wavelengths $> 0.7\mu m$). This spectral distinction separates the less absorbing from more absorbing regions of many atmospheric and surface constituents. In the atmospheric component the generally increasing absorption for wavelengths greater than $0.7\mu m$ is accounted for, though only the total near-infrared fluxes are available to the sea ice (Eq. 1; Collins et al., 2004). Sea ice absorption also generally increases for near-infrared wavelengths, so using integrated optical properties for the entire near-infrared band tends to weight the greater absorption. Such weighting masks the more transmissive near-infrared regions.

Therefore, we divide the near-infrared band into two sub-bands: $0.7-1.19\mu m$ and $1.19-5.0\mu m$, with flux weights based on radiative model calculations with cloudy polar atmospheres (Appendix C). The wavelength boundary $1.19\mu m$ is chosen to be compatible with atmosphere (Collins et al., 2004) and snow/ice albedo calculations (Ebert and Curry 1993, Curry et al., 2001). Using the atmospheric profile from Table C in Appendix C (with an overcast low stratus cloud), for bare sea ice, resulted in 78% of the $0.7-5.00\mu m$ down near-ir flux from the atmosphere in the $0.7-1.19\mu m$ sub-band, and 67% for clear sky. This change is due to differences in clear sky and overcast sky absorption: clouds absorb more of the $1.19-5.0\mu m$ sub-band relative to the $0.7-1.19\mu m$ sub-band, compared to clear sky conditions. We linearly interpolate between these extremes based on the fraction of direct to total near-infrared flux (i.e. $F_{SWnldr}/(F_{SWnldr} + F_{SWnidf})$; see Eq. 1).

5.2 Inherent Optical Properties: Snow

A. Pure Snow

Evaluation of IOPs for pure snow follows Wiscombe and Warren (1980), who modeled snow as ice spheres resulting in snow pack albedos (computed with the Delta-Eddington method) that agree well with spectral observations. As noted in section 3, this approach has been supported by recent work summarized in Flanner and Zender (2006). Mie scattering quantities of extinction efficiency, asymmetry parameter and single scattering albedo are available for ice spheres from 5 to 2500 μm radius over the spectral range of 300 to 3000 nm

(Steve Warren, personal communication). We spectrally interpolate these data linearly to 1 nm resolution for the range 300 to 2500 nm. For the purpose of incident weightings, we used observed downward surface solar spectral irradiance data for a mostly clear polar sky (Don Perovich, personal communication), from 350 to 2500 nm at 1 nm resolution. We assume a linear decrease in irradiance from 350 nm to zero at 304 nm, and zero irradiance for wavelengths longer than 2500 nm.

To evaluate IOPs averaged over our spectral bands (i.e. band IOPs), we take the following approach. Let $\kappa_\lambda, \omega_\lambda, g_\lambda$ represent the 1 nm Mie IOP data, and let $\alpha_\lambda(\kappa_\lambda, \omega_\lambda, g_\lambda)$ represent the 1 nm snow albedos for an optically thick layer with incident beam at $\mu=0.5$. We calculate the true band albedo, computed with the Delta-Eddington approximation, using $\bar{\alpha} = \int_{\lambda_1}^{\lambda_2} \alpha_\lambda S_\lambda d\lambda$, where S_λ is the normalized solar irradiance over the band λ_1 to λ_2 (Table 3 and Fig. 4). We calculate band IOPs as $k = \int_{\lambda_1}^{\lambda_2} \kappa_\lambda S_\lambda d\lambda$, $\omega = \int_{\lambda_1}^{\lambda_2} \omega_\lambda S_\lambda d\lambda$, $g = \int_{\lambda_1}^{\lambda_2} g_\lambda S_\lambda d\lambda$. We calculate a band albedo based on the band IOPs as $\alpha(k, \omega, g)$; but in general $\alpha < \bar{\alpha}$. Thus, we increase ω to ω' until $|\alpha(k, \omega', g) - \bar{\alpha}| < .0001$. The band extinction efficiency $Q = \int_{\lambda_1}^{\lambda_2} Q_\lambda S_\lambda d\lambda$, k, ω' , and g are shown in Tables 4 through 7 respectively. There are other approaches that one could take to determining band means (Mark Flanner, personal communication), but this seems to be a straightforward method, as single scattering albedo varies strongly across the bands compared with the extinction efficiency and the asymmetry parameter (see Wiscombe and Warren, 1980). In section 6.1 we discuss some limitations of this method.

We compute band snow extinction coefficient k_s for snow grain radius r_s (m) and number density N_s (m⁻³) from:

$$k_s(r_s) = Q_s(r_s) N_s \pi r_s^2 \quad (66)$$

where $Q_s(r_s)$ is the band solar weighted extinction efficiency. The number density N_s of snow grains is calculated from the snow density ρ_s :

$$\rho_s = N_s(\rho_i \frac{4}{3} \pi r_s^3) \quad \text{or} \quad N_s = \frac{\rho_s}{\rho_i} \frac{3}{4 \pi r_s^3} \quad (67)$$

where ρ_i is pure ice density. We use $\rho_s = 330$ kg m⁻³ and $\rho_i = 917$ kg m⁻³ from CCSM3 (Briegleb et al., 2004). Using the expression for number density N_s , the band extinction coefficient can be expressed as:

$$k_s(r'_s) = Q_s(r'_s) \frac{\rho_s}{\rho_i} \frac{3}{4 r_s'^3} \quad (68)$$

$$r'_s = f_r r_s$$

showing that snow extinction to first order varies inversely with grain radius as the extinction efficiency is a weak function of snow grain radius and wavelength, and where we have included an adjustment factor f_r as discussed in section 6.1 (the other IOPs $\omega(r'_s)$ and $g(r'_s)$ are evaluated at r'_s also). Note that in snow models with varying ρ_s and r_s , Eq. 68 can be used to compute varying extinction coefficient. Band parameters are shown in Tables 4 through 7. For snow grain radii r_s other than those in these tables, Q_s , ω_s and g_s can be linearly interpolated between table entries.

Table 3. Snow Albedo $\bar{\alpha} = \int_{\lambda_1}^{\lambda_2} \alpha_{\lambda} S_{\lambda} d\lambda$ (see text), for snow grain radii r_s and incident beam $\mu = 0.5$. Broadband and $0.7 - 5.0\mu m$ albedos computed with spectral cloudy-sky weights 0.67, 0.2574 and 0.0726 for $0.2 - 0.7\mu m$, $0.7 - 1.19\mu m$ and $1.19 - 5.0\mu m$ bands respectively.

$r_s(\mu m)$	$0.2 - 0.7\mu m$	$0.7 - 1.19\mu m$	$1.19 - 5.0\mu m$	$0.70 - 5.0\mu m$	broadband
5	0.995880	0.970839	0.725607	0.916888	0.969813
7	0.995161	0.964587	0.670421	0.899870	0.963715
10	0.994228	0.957411	0.617852	0.882708	0.957426
15	0.992844	0.948032	0.559041	0.862454	0.949815
20	0.991594	0.939454	0.518557	0.846857	0.943831
30	0.989708	0.926181	0.459038	0.823410	0.934830
40	0.988128	0.915255	0.417838	0.805823	0.927967
50	0.986741	0.905816	0.386818	0.791636	0.922356
65	0.984905	0.893542	0.351500	0.774293	0.915403
80	0.983278	0.882856	0.324554	0.760030	0.909606
100	0.981336	0.870346	0.296671	0.744138	0.903060
120	0.979585	0.859289	0.274754	0.730691	0.897450
140	0.977980	0.849327	0.256847	0.718981	0.892510
170	0.975780	0.835942	0.235124	0.703762	0.886014
200	0.973773	0.823996	0.217666	0.690603	0.880327
240	0.971327	0.809763	0.198870	0.675367	0.873660
290	0.968549	0.794039	0.180271	0.659010	0.866401
350	0.965530	0.777429	0.162715	0.642192	0.858828
420	0.962331	0.760376	0.146599	0.625345	0.851126
500	0.959001	0.743191	0.132039	0.608738	0.843414
570	0.956312	0.729716	0.121658	0.595943	0.837390
660	0.953099	0.714071	0.110616	0.581311	0.830409
760	0.949791	0.698460	0.100577	0.566926	0.823445
870	0.946410	0.683003	0.091500	0.552872	0.816543
1000	0.942698	0.666581	0.082709	0.538129	0.809190
1100	0.940014	0.655062	0.077018	0.527892	0.804014
1250	0.936225	0.639270	0.069806	0.513988	0.796887
1400	0.932675	0.624957	0.063812	0.501505	0.790389
1600	0.928250	0.607734	0.057226	0.486622	0.782513
1800	0.924119	0.592244	0.051840	0.473355	0.775367
2000	0.920231	0.578169	0.047354	0.461390	0.768813
2500	0.911368	0.547751	0.038858	0.435795	0.754429

Table 4. Snow extinction efficiencies $Q_s = \int_{\lambda_1}^{\lambda_2} Q_\lambda S_\lambda d\lambda$ (see text), for snow grain radii r_s .

$r_s(\mu m)$	$0.2 - 0.7\mu m$	$0.7 - 1.19\mu m$	$1.19 - 5.0\mu m$
5	2.131798	2.187756	2.267358
7	2.104499	2.148345	2.236078
10	2.081580	2.116885	2.175067
15	2.062595	2.088937	2.130242
20	2.051403	2.072422	2.106610
30	2.039223	2.055389	2.080586
40	2.032383	2.045751	2.066394
50	2.027920	2.039388	2.057224
65	2.023444	2.033137	2.048055
80	2.020412	2.028840	2.041874
100	2.017608	2.024863	2.036046
120	2.015592	2.022021	2.031954
140	2.014083	2.019887	2.028853
170	2.012368	2.017471	2.025353
200	2.011092	2.015675	2.022759
240	2.009837	2.013897	2.020168
290	2.008668	2.012252	2.017781
350	2.007627	2.010813	2.015678
420	2.006764	2.009577	2.013880
500	2.006037	2.008520	2.012382
570	2.005528	2.007807	2.011307
660	2.005025	2.007079	2.010280
760	2.004562	2.006440	2.009333
870	2.004155	2.005898	2.008523
1000	2.003794	2.005379	2.007795
1100	2.003555	2.005041	2.007329
1250	2.003264	2.004624	2.006729
1400	2.003037	2.004291	2.006230
1600	2.002776	2.003929	2.005700
1800	2.002590	2.003627	2.005276
2000	2.002395	2.003391	2.004904
2500	2.002071	2.002922	2.004241

Table 5. Snow extinction coefficients $k_s = \int_{\lambda_1}^{\lambda_2} k_\lambda S_\lambda d\lambda$ (see text), m^{-1} , for snow density 330 kg m^{-3} and snow grain radii r_s .

$r_s(\mu\text{m})$	$0.2 - 0.7\mu\text{m}$	$0.7 - 1.19\mu\text{m}$	$1.19 - 5.0\mu\text{m}$
5	115075.26	118095.87	122392.85
7	81144.01	82834.61	86217.37
10	56182.24	57135.11	58705.45
15	37113.21	37587.19	38330.41
20	27683.87	27967.53	28428.90
30	18346.33	18491.77	18718.47
40	13713.60	13803.80	13943.09
50	10946.79	11008.69	11104.97
65	8402.02	8442.27	8504.21
80	6816.41	6844.84	6888.82
100	5445.56	5465.14	5495.33
120	4533.43	4547.89	4570.24
140	3882.89	3894.08	3911.37
170	3194.95	3203.05	3215.57
200	2713.99	2720.17	2729.73
240	2260.24	2264.81	2271.86
290	1869.46	1872.80	1877.94
350	1548.18	1550.63	1554.39
420	1289.59	1291.40	1294.17
500	1082.87	1084.21	1086.29
570	949.64	950.72	952.38
660	819.94	820.78	822.09
760	711.89	712.55	713.58
870	621.75	622.29	623.11
1000	540.83	541.26	541.91
1100	491.60	491.97	492.53
1250	432.55	432.84	433.30
1400	386.16	386.40	386.78
1600	337.85	338.04	338.34
1800	300.28	300.43	300.68
2000	270.23	270.36	270.56
2500	216.15	216.24	216.38

Table 6. Snow single scattering albedo ω' (see text), for snow grain radii r_s .

$r_s(\mu m)$	$0.2 - 0.7\mu m$	$0.7 - 1.19\mu m$	$1.19 - 5.0\mu m$
5	0.9999994	0.9999673	0.9954589
7	0.9999992	0.9999547	0.9938576
10	0.9999990	0.9999382	0.9917989
15	0.9999985	0.9999123	0.9889724
20	0.9999979	0.9998844	0.9866190
30	0.9999970	0.9998317	0.9823021
40	0.9999960	0.9997800	0.9785269
50	0.9999951	0.9997288	0.9751601
65	0.9999936	0.9996531	0.9706974
80	0.9999922	0.9995783	0.9667577
100	0.9999903	0.9994798	0.9621007
120	0.9999885	0.9993825	0.9579541
140	0.9999866	0.9992862	0.9541924
170	0.9999838	0.9991434	0.9490959
200	0.9999810	0.9990025	0.9444940
240	0.9999772	0.9988171	0.9389141
290	0.9999726	0.9985890	0.9325819
350	0.9999670	0.9983199	0.9256405
420	0.9999605	0.9980117	0.9181533
500	0.9999530	0.9976663	0.9101540
570	0.9999465	0.9973693	0.9035031
660	0.9999382	0.9969939	0.8953134
760	0.9999289	0.9965848	0.8865789
870	0.9999188	0.9961434	0.8773350
1000	0.9999068	0.9956323	0.8668233
1100	0.9998975	0.9952464	0.8589990
1250	0.9998837	0.9946782	0.8476493
1400	0.9998699	0.9941218	0.8367318
1600	0.9998515	0.9933966	0.8227881
1800	0.9998332	0.9926888	0.8095131
2000	0.9998148	0.9919968	0.7968620
2500	0.9997691	0.9903277	0.7677887

Table 7. Snow asymmetry parameter $g_s = \int_{\lambda_1}^{\lambda_2} g_\lambda S_\lambda d\lambda$ (see text), for snow grain radii r_s .

$r_s(\mu m)$	$0.2 - 0.7\mu m$	$0.7 - 1.19\mu m$	$1.19 - 5.0\mu m$
5	0.859913	0.848003	0.824415
7	0.867130	0.858150	0.848445
10	0.873381	0.867221	0.861714
15	0.878368	0.874879	0.874036
20	0.881462	0.879661	0.881299
30	0.884361	0.883903	0.890184
40	0.885937	0.886256	0.895393
50	0.886931	0.887769	0.899072
65	0.887894	0.889255	0.903285
80	0.888515	0.890236	0.906588
100	0.889073	0.891127	0.910152
120	0.889452	0.891750	0.913100
140	0.889730	0.892213	0.915621
170	0.890026	0.892723	0.918831
200	0.890238	0.893099	0.921540
240	0.890441	0.893474	0.924581
290	0.890618	0.893816	0.927701
350	0.890762	0.894123	0.930737
420	0.890881	0.894397	0.933568
500	0.890975	0.894645	0.936148
570	0.891035	0.894822	0.937989
660	0.891097	0.895020	0.939949
760	0.891147	0.895212	0.941727
870	0.891189	0.895399	0.943339
1000	0.891225	0.895601	0.944915
1100	0.891248	0.895745	0.945950
1250	0.891277	0.895951	0.947288
1400	0.891299	0.896142	0.948438
1600	0.891323	0.896388	0.949762
1800	0.891340	0.896623	0.950916
2000	0.891356	0.896851	0.951945
2500	0.891386	0.897399	0.954156

B. Aerosols in Snow

The effects of aerosols, such as dust and carbon soot, can be included if desired. Field work (Warren and Wiscombe, 1980, Warren and Clark, 1990, Grenfell et al. 2002, and Brandt et al. 2005) suggest minimal aerosol contamination in snow except very close to human settlements or possibly due to unusual volcanic or dust events. Aerosol effects can be included (for each grain radius r_s and band λ) from the definitions of extinction and single scattering albedo using the band data in Tables 4 to 7 as:

$$\begin{aligned} k_s(r_s, \lambda) &= \kappa_s(r_s, \lambda) + \sigma_s(r_s, \lambda) \\ \omega_s(r_s, \lambda) &= \sigma_s(r_s, \lambda) / k_s(r_s, \lambda) \end{aligned} \tag{69}$$

where κ_s and σ_s are the band absorption and scattering coefficients respectively. If for example, we assume the aerosol effects only the absorption coefficients, we can write:

$$\kappa_s(r_s, \lambda) = \kappa_{ps}(r_s, \lambda) + \kappa_d(r_s, \lambda) + \kappa_{cs}(r_s, \lambda) \tag{70}$$

where subscript ps refers to pure snow, d to desert dust and cs to carbon soot respectively. Then from the definitions in Eq. 69 the adjusted extinctions and single scattering albedo can be recomputed and used in the snow radiation calculation to include the desired dust and carbon soot effects.

C. Transition From Snow Covered Ice to Bare Ice

The present treatment of solar radiation in CCSM3 (section 2) uses a fractional horizontal coverage of snow over sea ice, f_s , as in Eqs. 8 and 9, which is a function of snow depth. In reality, for small snow depths (order a few centimeters) some patchy snow and uncovered sea ice will usually be present simultaneously (Allison et al. 1993, Brandt et al. 2005). In the CCSM3 solar radiation treatment, snow of any depth is completely opaque to solar radiation (Eq. 13), which is not realistic for small snow depths and large snow grain radii.

For the Delta-Eddington solar radiation treatment, the fractional horizontal coverage of snow is one for snow depth greater than .03 m; for snow depth less than .03 m we allow fractional snow coverage proportional to the snow depth. For snow overlying sea ice, the Delta-Eddington solar radiation treatment allows penetrating solar radiation that depends on snow depth and snow grain size, as illustrated in Fig. 5. As shown in Fig. 5, when snow grains increase in size, the snow depth required to mask the underlying sea ice from penetrating solar radiation becomes thicker. A few centimeters of snow will mask the underlying sea ice only for the smallest snow grain radii. This shows that the Delta-Eddington solar radiation treatment results in a smooth transition in AOPs between snow covered and bare sea ice as the snow melts. Also, the larger the snow grain radii, the more absorptive each grain becomes (i.e. lower ω' ; see Table 6) and therefore the asymptotic snow layer albedos for thick layers decline with increasing grain radius (Fig. 5).

D. Tuning Snow Apparent Optical Properties

It is sometimes necessary to adjust solar radiation absorbed in sea ice for coupled CCSM applications to produce acceptable polar simulations. In the present CCSM3 treatment, such tuning usually involves direct changes to the snow albedos (section 2; compare the x1 and x3 non-melting snow albedos of Eq. 2 for example), but such changes are usually not consistent with the rest of the parameterization. For instance, one could arbitrarily change the visible band albedos and not the near-infrared band albedos, or change the two band albedos by guessing how much each band should change relative to the other.

In the Delta-Eddington solar radiation treatment, we can adjust the snow grain radius r_s used for non-melting and/or near-melting snow, and thus snow IOPs, in a manner that self-consistently changes all computed snow AOPs. Table 3 can be used as a guide to determine how much to change grain size if an estimated change in the snow albedo is known. The details of such changes will depend on how the snow grain radius r_s and snow density ρ_s are specified (see Table 2).

Let us consider the simplest sea ice snow model that specifies snow grain radius r_s and snow density ρ_s for non-melting and near-melting conditions. One can select a non-melting snow grain radius whose snow albedo agrees closely with the present version of solar radiation in CCSM for the high horizontal resolution case (x1; see Table 21). From Table 3, we could estimate that a snow grain radius of $290\mu m$ would result in about the same snow broadband albedo. To lower the broadband albedo by .05 for x3 resolution (see Eqs. 2), from Table 3 one could choose a snow grain radius of $870\mu m$. The snow band albedos shown in Table 3 (and hence all other AOPs) for the increased snow grain radius will be computed consistently (e.g. the snow IOP Tables 5 through 7). For near-melting conditions from Eq. 3 we note that CCSM has broadband snow albedos 0.745, so from Table 3 we would need a very large snow grain radius of $2000\mu m$ or more.

5.3 Inherent Optical Properties: Sea Ice

The objective is to specify vertical profiles of inherent optical properties (IOPs) for bare and ponded sea ice that are (i) consistent with climatology, (ii) representative of both first and multi-year ice, (iii) appropriate for both thin and thick ice, and (iv) designed to produce appropriate backscatter of solar radiation to atmosphere, transmittance to ocean, and vertical flux distribution within the ice.

IOP profiles for bare and ponded ice are derived from optical observations made during SHEBA. The variability in observed spectral albedo is used to identify variability in the IOP profile. Finally, ways to tune the IOP profiles are suggested. Many of the model calculations presented in this section were carried out using a 4-stream discrete ordinates method 1-D radiative transfer model (DOM; Grenfell, 1991) with diffuse incident radiation. The assumption of diffuse incident radiation is appropriate for the low sun angle of high latitudes and the frequent complete overcast observed in the Arctic during summer.

A. Derivation of Bare Ice and Ponded Ice Profiles

Average albedo

Spectral albedo data taken along the albedo survey line (“albedo line”) during the SHEBA observations of the summer of 1998 (Perovich et al., 2002) were used to identify average albedos for bare and ponded ice cases (Fig. 6). The ponded ice cases represent 100% pond coverage. These average albedo measurements were taken on the albedo line between 7 July and 12 August 1998. The band averaged values for these spatially and temporally averaged albedos are given in Table 8. Since the data do not span the entire spectral range encompassed by the CCSM computation, the computation of spectrally integrated values for the 0.2 – 0.7 micron band and 1.19 – 5.0 micron band were carried out by extrapolating the data based on our best understanding of the optical properties of sea ice. Measurements in the 1.19 - 5.0 μm band are highly uncertain. For the ponded case, DOM was used to predict an albedo in this band of 0.066, based on the Fresnel reflection at the pond surface. Bare ice measurements were not made at these long wavelengths either, so the model was used to predict an albedo in this band of 0.110. Since the Fresnel layer in the bare ice case is beneath the surface scattering layer, we do not expect light at these long wavelengths to be affected by the refraction. The estimated albedo is based on our best understanding of the scattering and absorption of ice in the surface layer.

Table 8. Band averaged albedos and related standard deviations for observed spectra, obtained along the albedo line during the SHEBA observations of the summer of 1998. The ponded ice band albedos are for 100% pond coverage.

Spectral band	$0.2 - 0.7\mu m$	$0.7 - 1.19\mu m$	$1.19 - 5.0\mu m$
Bare ice albedo	0.753 ± 0.023	0.569 ± 0.028	0.110 ± 0.027
Ponded ice albedo	0.251 ± 0.115	0.086 ± 0.022	0.066 ± 0.007

The determination of typical IOP profiles for the bare and ponded ice cases was carried out by assuming two typical ice property profiles. The bare ice case was assumed to be 2 m thick ice and the ponded ice was taken to be 1.5 m thick. Density profiles were assigned based on observed field data (Table 9). We distinguish three types of layers for bare sea ice: SSL, DL and INT layers, and two for ponded ice: SSL and INT layers. Note that the density of interior and ponded ice (0.920 Mg m^{-3}) is greater than the density of pure ice (0.917 Mg m^{-3}), reflecting fractions of liquid water and salt in the included brine.

Table 9. Ice thickness and density profiles for bare and ponded ice cases used to derive IOP profiles. The ice thickness was taken to be 2 m for the bare case, 1.5 m for the ponded case.

Bare ice			Ponded ice		
Layer	Thickness (cm)	Density (Mg m^{-3})	Layer	Thickness (cm)	Density (Mg m^{-3})
1/4 (SSL)	5	0.42	1/4 (SSL)	5	0.92
3/4 (DL)	45	0.83	3/4 (INT)	32.5	0.92
2 (INT)	50	0.92	2 (INT)	37.5	0.92
3 (INT)	50	0.92	3 (INT)	37.5	0.92
4 (INT)	50	0.92	4 (INT)	37.5	0.92

Absorption coefficient

The IOPs required by the Delta-Eddington treatment of solar radiation consist of vertical profiles of extinction coefficient $k(z)$, single scattering albedo $\omega(z)$, and asymmetry parameter g through the snow/pond/ice column. The first two of these three quantities are functions of the scattering coefficient $\sigma(z)$ and absorption coefficient $\kappa(z)$, such that $k(z) = \sigma(z) + \kappa(z)$, and $\omega(z) = \sigma(z)/k(z)$.

It is useful to determine values of the absorption coefficient $\kappa(z)$ first. Following Grenfell (1991), the bulk $\kappa(\lambda)$ for sea ice (where λ is wavelength) can be computed as:

$$\kappa(\lambda) = \kappa_{pi}(\lambda)V_{pi} + \kappa_{br}(\lambda)V_{br} + \kappa_{ps}(\lambda)V_{ps} + \kappa_{im}(\lambda)V_{im} \quad (71)$$

where subscript “pi” indicates pure ice, subscript “br” indicates brine, subscript “ps” indicates precipitated salts, subscript “im” indicates impurities (typically soot, sediment, or organic material), and V is the fractional volume of each constituent. Fractional volumes range between 0 and 1. Precipitated salts are solid salt crystals that precipitate from the brine as the temperature decreases, liquid water freezes to the inclusion walls, and the brine concentrates.

In this treatment, the bulk absorption for sea ice is attributed entirely to the pure ice and liquid brine components. The precipitated salts are assumed to have negligible absorption. We assume no impurities within the ice. Furthermore, differences in absorption for brine (liquid water) and pure ice are assumed to be negligible. As a result,

$$\kappa(\lambda) \approx \kappa_{pi}(\lambda)(V_{pi} + V_{br}) \quad . \quad (72)$$

From Cox and Weeks’ (1983) expressions for V_{pi} and V_{br} , we make the approximation that $V_{pi} + V_{br} = \rho_{si}/\rho_{pi}$ where ρ_{si} is the density of sea ice (typically between 0.5 Mg/m³ and 0.92 Mg/m³) and ρ_{pi} is the density of pure ice (0.917 Mg/m³), so that:

$$\kappa(\lambda) \approx \kappa_{pi}(\lambda)\rho_{si}/\rho_{pi} \quad (73)$$

Because we assume the absorption coefficient of water (brine) to be approximated by the absorption coefficient for pure ice, this approximation is best for low salinity ice, but grows worse for high salinity ice. At 15 ppt salinity, this approximation will result in as much as a 4% error in the calculation of $\kappa(\lambda)$. Estimated uncertainties for the assignment of density for the various layers within the ice column are at least as large.

Table 10. Calculated absorption coefficients for bare, melting sea ice.

Layer	Thickness (cm)	0.2 – 0.7 μm $\kappa(m^{-1})$	0.7 – 1.19 μm $\kappa(m^{-1})$	1.19 – 5.0 μm $\kappa(m^{-1})$
1/4 (SSL)	5	.100	3.74	642
3/4 (DL)	45	.198	7.39	1270
2 (INT)	50	.219	8.20	1400
3 (INT)	50	.219	8.20	1400
4 (INT)	50	.219	8.20	1400

Table 10 gives the computed values of $\kappa(\lambda)$ relevant for the bare ice case. We distinguish SSL, DL and INT layer values. Band averaged values are derived from the spectral κ values from the visible (Grenfell and Perovich, 1981) and near infrared (Irvine and Pollack, 1968) by integrating $\kappa(\lambda)$ weighted by a downwelling incident spectrum for a mostly clear polar sky (D. Perovich, personal communication, 2005). This downwelling spectrum does not include wavelengths shorter than 350 nm or longer than 2500 nm, so values for these wavelengths were extrapolated from the existing spectrum.

These band-averaged absorption coefficients are appropriate for use near the ice surface, but not necessarily in the ice interior. Ideally, absorption coefficients for use within the ice should be weighted by a typical in-ice spectral irradiance. This implicitly introduces a bias to whatever ice thickness is initially selected for determining this within-ice irradiance. As of now, all the absorption coefficients employed in this parameterization were calculated with an estimated surface irradiance weighting. While the transmittance calculated through the ice might be sensitive to this approximation, the albedo should not be sensitive to the method used to estimate absorption coefficients deeper within the ice.

Scattering coefficient and asymmetry parameter

Scattering parameters were inferred from the observed spectral albedo data using results from the 4-stream Discrete Ordinates Method radiative transfer model (DOM). Scattering was taken to be independent of wavelength, a result of Mie theory for scatterers with a distribution of sizes considerably larger than the wavelength. A similarity relation was used to assume that the scattering asymmetry parameter (g) could be fixed and, by adjusting the scattering coefficient (σ), the total amount of scattering could be appropriately represented. This similarity relation is:

$$s = \sigma(1 - g) \tag{74}$$

From this relationship, domains with identical s and κ have approximately the same apparent optical properties (e.g. McCormick and Rinaldi, 1989). This relationship thus permits us to fix the value of g and then determine a value for σ . The range of g values appropriate for sea ice is estimated from Mie theory, given typical inclusion sizes and known refractive indices for ice, brine (Maykut and Light, 1995), and air. Mie calculations result in values between 0.86 and 0.99, but the development of a consistent treatment for IOPs is considerably simplified if the g values are fixed and similarity employed. Therefore, the value of g was set to 0.94 for all layers in the ice.

By matching DOM calculations run for a matrix of σ values and the $\kappa(z)$ profiles given in Table 10 with the observed spectral albedo, a $\sigma(z)$ profile is inferred. We adjust the $\sigma(z)$ profile to distinguish SSL, DL and INT layers, and constrain the values further to be roughly in the mid-range of the SHEBA cases observed in Light et al. (submitted) and to yield spectral albedos within the variance of the albedo line values of Table 8. The final $\sigma(z)$ profile is shown in Table 11. Because the inclusions in sea ice that cause the scattering of solar radiation are generally much larger (diameters greater than $10\text{ }\mu\text{m}$) than the wavelength of the radiation ($0.2 - 5\text{ }\mu\text{m}$), values of σ are assumed to be independent of wavelength. The real refractive index (n) given in Table 11 corresponds to typical values for the $0.2 - 0.7\text{ }\mu\text{m}$ waveband. Because of the enhanced absorption in the longer wavebands, the refractive index plays a diminished role as the Fresnel boundary is buried beneath a layer which is highly absorptive.

Table 11. Vertical profiles of refractive index (n), scattering coefficient (σ), and scattering asymmetry parameter (g) for the bare ice case.

Layer	Thickness (cm)	n	σ (m^{-1})	g
1/4 (SSL)	5	1.0	1000	0.94
3/4 (DL)	45	1.3	100	0.94
2 (INT)	50	1.3	20	0.94
3 (INT)	50	1.3	20	0.94
4 (INT)	50	1.3	20	0.94

Fig. 7 shows the observed average spectral albedo compared with the CCSM3 albedo parameterization and the Delta-Eddington parameterization. The integrated wavelengths for the observed average albedo are shown in Table 8. Uncertainties for the observed albedo in the $1.19 - 5.0 \mu\text{m}$ waveband could be considerably larger than indicated here. Not only are measurements in this waveband scarce, but the albedo is very sensitive to the microstructure of the uppermost millimeters of the ice. These observed values compare with the proposed new band averaged DOM computed albedo values of 0.754, (0.2% difference from observation), 0.573, (0.75%), and 0.023, (80%) for the three bands respectively. It is worth pointing out that the finite resolution of the vertical variation in ice IOPs in CCSM, especially near the surface, along with the constraint to treat scattering properties independent of waveband, results in significant departure between observed and modeled albedo in one or more wavebands. To correct for this problem, we have adjusted the scattering coefficient for the $1.19-5.0\mu\text{m}$ band to produce an albedo in better agreement with the observations. This adjustment is designed to compensate for the finite layer structure required by CCSM within the sea ice. To compensate for this lack of a very thin, highly scattering layer at the ice surface, we have increased the scattering coefficient for the entire 5 cm thick surface layer from 1000 m^{-1} to 6400 m^{-1} for this waveband alone. Scattering coefficients of magnitude 6400 m^{-1} have been observed in thin surface layers on melting bare ice (Light et al., submitted). The full set of IOPs for bare ice are given in Table 12.

Table 12. Inherent Optical Properties of bare sea ice. k is the extinction coefficient, ω the single scattering albedo, and g the asymmetry parameter.

Level	$0.2 - 0.7\mu m$	$0.7 - 1.19\mu m$	$1.19 - 5.0\mu m$
	$k(m^{-1})$	$k(m^{-1})$	$k(m^{-1})$
1/4 (SSL)	1000.1	1003.7	7042
3/4 (DL)	100.2	107.7	1309
2 (INT)	20.2	27.7	1445
3 (INT)	20.2	27.7	1445
4 (INT)	20.2	27.7	1445
	ω	ω	ω
1/4 (SSL)	.9999	.9963	.9088
3/4 (DL)	.9980	.9287	.0305
2 (INT)	.9901	.7223	.0277
3 (INT)	.9901	.7223	.0277
4 (INT)	.9901	.7223	.0277
	g	g	g
1/4 (SSL)	.94	.94	.94
3/4 (DL)	.94	.94	.94
2 (INT)	.94	.94	.94
3 (INT)	.94	.94	.94
4 (INT)	.94	.94	.94

The albedo of ponded ice is determined by the optical properties of pond water and the ice beneath the pond. Perovich et al. (2002) noted “light” and “dark” ponds along the albedo line which resulted in the large visible pond albedo range of Fig. 6 . We constrained the pond INT IOPs to be those for bare sea ice, then tailored the SSL scattering such that the albedo matched the average melt pond albedo for the albedo line, averaged over the SHEBA summer. The IOPs were derived for 150 cm-thick ice overlain by a 35 cm deep pond. The average IOPs appropriate for ponded ice are given in Tables 13, 14 and 15. Because variations in the scattering properties of ice beneath ponds are understood to be significantly larger than the variation in pond water optical properties, only the absorption of radiation, not scattering (molecular or particulate), within the water is represented. Note also that the refractive index of the ponded case is set to 1.3 for both the pond water and underlying ice.

Table 13. Absorption coefficients for the ponded ice profile.

Layer	Thickness (cm)	$0.2 - 0.7\mu m$ $\kappa(\text{m}^{-1})$	$0.7 - 1.19\mu m$ $\kappa(\text{m}^{-1})$	$1.19 - 5.0\mu m$ $\kappa(\text{m}^{-1})$
Pond	35	.200	12.4	729
Ice	150	.219	8.2	1400

Table 14. Scattering properties for ponded ice: index of refraction (n), scattering coefficient (σ), and scattering asymmetry parameter (g).

Layer	Thickness (cm)	n	σ (m^{-1})	g
Pond	35	1.3	0	0
Ice (SSL)	5	1.3	70	0.94
Ice (INT)	145	1.3	20	0.94

Table 15. Inherent Optical Properties of ponded ice. k is the extinction coefficient, ω the single scattering albedo, and g the asymmetry parameter. Ice properties are for the under-pond ice, and valid for all levels. Pond depth used to infer IOPs is 0.35 m and ice-under-pond thickness is 1.5 m.

Type	$0.2 - 0.7\mu m$	$0.7 - 1.19\mu m$	$1.19 - 5.0\mu m$
	$k(\text{m}^{-1})$	$k(\text{m}^{-1})$	$k(\text{m}^{-1})$
pond	0.20	12	729
ice (SSL)	70.2	77.7	1309
ice (INT)	20.2	27.7	1445
	ω	ω	ω
pond	0	0	0
ice (SSL)	.9972	.9009	.0305
ice (INT)	.9901	.7223	.0277
	g	g	g
pond	0	0	0
ice (SSL)	.94	.94	.94
ice (INT)	.94	.94	.94

Note that the under-pond SSL and DL ice IOPs are different from those of bare ice in Table 12. In section 5.3E we present one approach to modeling the transition between

these two surface types as pond depth becomes small.

In addition to the inherent optical properties of bare ice and ponded ice, the spectral reflectivities to direct and diffuse radiation of the underlying ocean are required. As ice and ocean have very nearly the same index of refraction, the usual surface refraction effects of the air/ocean interface can be ignored. For distilled water, scattering coefficients for wavelengths $> 0.7\mu\text{m}$ are so small that diffuse reflectivities would be less than .001 and can be ignored. For the visible band, the reflectivity depends on the spectral distribution of penetrating radiation, as the scattering coefficients are spectrally varying due to molecular scattering: see Paltridge and Platt (1976) and references therein. As various approximations are possible, we assume visible band direct and diffuse reflectivity of .01, and near-infrared reflectivity 0 (see also Paulson and Simpson, 1977).

B. Absorption by Algae

The assumption that there exist no impurities within the ice is reasonable for the surface and interior, but probably not a good assumption for the ice at the ocean interface. Absorption by impurities in the lowest layer will not substantially affect the spectral albedo, but will affect the transmittance of light to the ocean.

Concentrations of light absorbing algae are commonly found in sea ice near the ice-ocean interface. Algae particles are assumed to cause no significant scattering. Absorption by algae is assumed to be due to chlorophyll a (Chl a), and is restricted to the $0.2 - 0.7 \mu\text{m}$ waveband. We follow the treatment of Grenfell (1991), where

$$\kappa_{alg} = SA * mgchla / z \quad (75)$$

where κ_{alg} is the absorption coefficient for algae, SA the specific absorption coefficient ($0.004 \text{ m}^2 [\text{mg Chl a}]^{-1}$), and $mgchla$ is the absorber mass path in milligrams of Chl a per m^2 over the layer thickness z . The specific absorption coefficient SA is derived from that given by Soo Hoo et al., 1987 ($0.0078 \text{ m}^2 (\text{mg Chl a})^{-1}$) multiplied by a spectral weighting coefficient (Grenfell, 1991) and weighted by the same standard incident irradiance used to weight the ice absorption coefficients. Thus,

$$\kappa_{alg} = 0.004 \text{ m}^2 [\text{mg Chl a}]^{-1} * mgchla / z \quad (76)$$

Typical values of $mgchla$ are between 0 and 300 mg m^{-2} . This computed value of κ_{alg} can then be added directly to the bulk κ for the layer (Eq. 71). This value of κ will in turn affect extinction and ω . Values for κ_{alg} are given in Table 16 for a range of $mgchla$ values distributed over a 0.5 m thick ice layer. The magnitude of the absorption incurred by 10 mg Chl a distributed over a 0.5 m thick layer is comparable to the absorption incurred by 19 cm of clean, interior sea ice (Table 10; $0.2 - 0.7 \mu\text{m}$ band).

Table 16. Values of κ_{alg} (for $0.2 - 0.7 \mu\text{m}$ waveband) for select values of $mgchla$ distributed over a 0.5 m thick layer.

$mgchla$ (mg Chl a) m^{-2}	κ_{alg} (m^{-1})
1	0.008
10	0.08
100	0.8
300	2.4

C. Transmittance Through Bare Ice and Ponded Ice

Spectral values of ice transmittance computed from the IOP profiles were compared with observations. There exists no observational “climatology” for ice transmittance. It is difficult to compare predicted and observed transmittance for at least three reasons. First, transmittance of light beneath sea ice is difficult to measure, so there is not an abundance of data, and the uncertainties are significant (particularly due to edge effects). Second, the transmittance depends on ice thickness, so meaningful comparisons between observed cases requires such cases to have identical ice thicknesses, which is rarely obtainable in practice. Third, the transmittance can be very sensitive to the presence of absorbing impurities within the ice column. In particular, substantial concentrations of chlorophyll and sediment can be prevalent within the ice. Concentrations of these impurities can affect both albedo and transmittance, but those within the interior or near the bottom of the ice will affect transmittance predominantly. Fig. 8 shows spectral transmittance data taken beneath various bare ice locations (with various ice thicknesses) during the SHEBA summer, along with model predicted transmittance for ice thicknesses between 1.0, 1.5 and 2.0 m. We assume 75 mg Chl a m^{-2} over 0.5 m in the lowest sea ice layer.

The model-predicted transmittances roughly correspond with the observations. Clearly the transmittance measured under the ice on 15 August (first year, 1 m thick) has distinctly different spectral shape than the other transmittance spectra. The spectral peak at wavelength longer than 550 nm suggests that a significant quantity of ice algae inhabited this ice. The wavelength integrated transmittance for this observed spectrum is 0.09, which is close to the computed 0.094 value.

Fig. 9 shows observed spectral transmittance beneath ponded ice on 27 July measured at the SHEBA site, along with the Delta-Eddington solar radiation calculation for 200 cm thick ponded ice (150 cm ice + 50 cm pond depth). Based on these comparisons, we conclude that the new treatment for solar radiation is appropriate for the simulation of light transmission through both bare and ponded ice.

D. Variability

The observed albedo variability is remarkably small for bare ice (average standard deviation in $0.2 - 0.7 \mu\text{m}$ waveband is ± 0.02) and remarkably large for ponded ice (average standard deviation in $0.2 - 0.7 \mu\text{m}$ waveband is ± 0.12), (see Table 8). The reason for this albedo variability difference is due to the physical properties of the two ice types. Bare ice has an optically thick SSL. The thickness of this layer responds to changes in freeboard height (and hence changes in ice thickness), surface meteorological conditions, and the penetration and absorption of solar radiation. When the thickness of the layer increases, the total backscattering from the layer increases. The properties of the uppermost millimeters/centimeters of this surface layer are sensitive to the amount of direct solar radiation incident on the ice and whether there is atmospheric moisture available to form condensation on the surface. In general, when direct solar radiation penetrates the uppermost layers, there are increases in backscattering at depth within this surface layer. When condensation forms immediately at the top surface of the ice, the backscattering increases where the condensation forms. The net effects of these physical changes lead to only small variability in the solar radiative properties of bare ice at all wavelengths.

Ponded ice, on the other hand, has been observed to have widely varying spectral albedo in the visible band. The albedo at visible wavelengths depends critically on the thickness and scattering properties of the ice beneath the pond, and has little relation to the pond depth. When this ice contains significant concentrations of gas and brine inclusions it is highly scattering; likewise ponded ice with small numbers of inclusions has considerably lower albedo. It is common to observe the full range of pond albedos at various sites on a single multiyear floe at a single time. Ponds on undeformed first-year floes are likely to have albedos with less pond-to-pond variability.

A simple way of simulating these variations is to vary the total amount of scattering by the ice. Fig. 10 shows model calculated albedos for the bare and ponded ice cases where the scattering coefficient has been increased and decreased by 15% (designed to simulate one standard deviation of the bare ice observations) and 30% (designed to simulate two standard deviations of the bare ice observations), and by +300% and -50% (designed to simulate one standard deviation of the ponded ice observations). Since a significant part of the pond albedo variability can be attributed to changes in ice thickness during the course of a melt season, some of the considerable variability associated with ponds will be expressed strictly as a result of the ice thickness distribution. For this reason, estimates of +300% and -50% increases in scattering coefficient are to be used with caution when simulating the variability of ponded ice albedo. Realistically, these changes in scattering apply to optical depth, the product of extinction and ice thickness. Since the albedo of thick bare ice is relatively insensitive to the ice thickness, the variability in observed bare ice albedo is largely attributable to changes in extinction, particularly scattering.

Also note that variability of ponded ice is approximately five times larger than variability

of bare ice, and that the areal coverage of ponded ice is roughly 0.3 at its maximum value. This implies that the relative influences of bare and ponded ice variability on the area averaged albedo are comparable.

Fig. 11 shows the effects of applying a one standard deviation change (15%) in $\sigma(z)$ and two standard deviation change (30%) to the bare ice transmittance calculation. Fig. 12 shows the effects of applying a one standard deviation change (+50% and -300%) in $\sigma(z)$ to the ponded ice transmittance calculation. Note that uncertainty in transmittance through ponded ice can be translated to uncertainty in ice thickness.

E. Transition From Bare Ice to Ponded Ice

In section 5.3A we presented bare ice and ponded ice IOPs (Tables 12 and 15 respectively). The SHEBA measured albedos on which these IOPs are based (Table 8) differ significantly between bare ice and ponded ice. As pond water is mostly transparent in the visible band (e.g. Tables 14 and 15), the difference between bare ice and ponded ice albedo is due primarily to the reduction in scattering in the under pond ice (compare Tables 11 and 14). We showed in section 3 that when pond depth $h_p = 0$, bare ice IOPs are used to compute AOPs; when $h_p > 0$, ponded ice IOPs are used (e.g. Eq. 18). This raises the question of how small h_p can be before bare ice IOPs and not ponded ice IOPs are used, and what kind of transition should there be between the two sets of IOPs that somehow depends on the value of h_p . Can it be argued that ponds with h_p values as small as, say .01m, should have under pond IOPs? What about .001m?

We approximate the transition between the highly scattering bare ice and reduced scattering ice under ponds by following the previous subsection on variability. There it was argued that albedo variability in both bare sea ice and ponded ice can be simulated by variations in the scattering coefficient in sea ice, due to variability in concentrations of gas and brine inclusions. If we then interpolate the scattering coefficient in pond depth between bare ice and ponded ice IOPs, we will compute a bare ice to ponded ice transition that is consistent with observations on albedo variability.

Hence, we define two pond depths: h_{pmin} , the minimum pond depth, and h_{p0} , an asymptotic pond depth below which a linear interpolation of the scattering coefficient in pond depth h_p is done for IOPs from bare ice to ponded ice. For $h_{pmin} < h_p < h_{p0}$, with “i” and “p” for bare ice and ice under pond IOPs respectively, we have at each sea ice level (Table 1):

$$\sigma_i = k_i \omega_i, \quad \sigma_p = k_p \omega_p \quad (77)$$

$$\kappa_p = k_p(1 - \omega_p) \quad (78)$$

$$\sigma(h_p) = \sigma_i + (\sigma_p - \sigma_i)(h_p/h_{p0}) \quad (79)$$

$$k(h_p) = \sigma(h_p) + \kappa_p \quad (80)$$

$$\omega(h_p) = \sigma(h_p)/k(h_p) \quad (81)$$

$$g(h_p) = g_i \quad (82)$$

(see first few equations in Eqs. 50 for definitions of σ and k). Fig. 13 shows the resulting broadband Delta-Eddington albedo dependence on pond depth, using the values $h_{pmin} = 0.005$ m and $h_{p0} = 0.20$ m. Ponds deeper than 0.20 m in this plot show decline in pond albedo towards the deep ocean limit; the large depths are unrealistic for ponds over sea ice, but are shown to illustrate that the broadband Delta-Eddington albedo for deep water asymptotes to the correct albedo. One can see that without any interpolation at all, pond albedos would remain very small as pond depth tends to zero, as the under pond ice IOPs have little scattering as just mentioned. The interpolation allows an adjustable and more physically defensible transition. Note that most of the spectral variation in albedo with pond depth is in the visible, as the near-ir asymptotes quickly for pond depths larger than .05 m .

F. Tuning Bare Ice and Poned Ice Apparent Optical Properties

As mentioned for snow, it is sometimes necessary to adjust solar radiation absorbed in sea ice for coupled CCSM applications to produce acceptable polar simulations. In the present treatment of solar radiation in CCSM3, such tuning can involve direct changes to the sea ice albedos (section 2; compare the x1 and x3 non-melting sea ice albedos of Eq. 4 for example), but such changes are usually not consistent with the rest of the parameterization. For instance, just as for snow albedos, one could arbitrarily change the visible band sea ice albedos and not the near-infrared band sea ice albedos, or change the two band albedos by guessing how much each band should change relative to the other.

In an effort to provide guidance for tuning this parameterization, we address the question: What is the typical range of the IOPs that produce realistic variations in surface albedos and other measured apparent optical properties (AOPs)? We can think of the variation in IOPs as a standard deviation about the mean. Tuning can then involve adjusting the mean IOPs in units of the standard deviation. In this manner, any user will know how far (in units of variance) from the typical mean they are tuning. We already presented a discussion of bare ice and pond ice albedo variability two subsections ago, and introduced implicit scaling factors for the scattering coefficients when we discussed one and two sigma variations. Here, we formalize this for tuning purposes.

Within the interior of the ice, the gas and brine content are determined by ice growth rate, brine capture and desalination processes (gravitational drainage and flushing primarily). Within the SSL, the individual ice grain sizes are determined by the absorption of solar radiation, drainage of melt water, and condensation of atmospheric moisture at the surface. These micro-structural properties directly affect the scattering coefficient of the ice, which in turn affect the AOPs (e.g., albedo and transmittance) of the ice cover. We propose to vary the IOPs by maintaining the vertical structure and absorption coefficient but permitting the scattering coefficient to vary, consistent with the discussion on variability

two subsections previous.

For sea ice, let $\sigma(z)$ and $\kappa(z)$ be the scattering and absorption coefficients respectively, where z is the vertical coordinate. Let $s_{\sigma}^{\pm}(z)$ be the empirical standard deviations for an increase and decrease of the scattering coefficient, respectively. To preserve the vertical and spectral profiles for the coefficients, we assume $s_{\sigma}^{\pm}(z)$ are fractions f_{ice}^{\pm} of the mean value, i.e.

$$s_{\sigma}^{\pm}(z) = f_{ice}^{\pm} \sigma(z) \quad (83)$$

where f_{ice}^{+} , f_{ice}^{-} are the positive fractions of the mean scattering coefficient that yield the standard deviation for a typical increase and decrease, respectively. These fractions are to be determined from the data.

Thus, tuning can be done by defining a dimensionless “standard deviation parameter” R_{ice} , so that the modified standard deviation for scattering $s'_{\sigma}(z)$ can be expressed as:

$$s'_{\sigma}(z) = R_{ice} s_{\sigma}^{\pm}(z) = R_{ice} f_{ice}^{\pm} \sigma(z) \quad (84)$$

$$k(z) = \kappa(z) + \sigma(z) + s'_{\sigma}(z) \quad (85)$$

$$\omega(z) = (\sigma(z) + s'_{\sigma}(z)) / (\sigma(z) + s'_{\sigma}(z) + \kappa(z)) \quad (86)$$

Note that R_{ice} can be negative as well as positive, and has no bounds apart from the requirements of positivity of the modified scattering coefficient $\sigma(z) + s'_{\sigma}(z)$, and rationality! Any value within -1 to $+1$ would be within the range of most measurements. Typical tuning might be in the range of -2 to $+2$.

From our discussion of variability, for bare ice we select $f_{ice}^{+} = 0.15$ and $f_{ice}^{-} = 0.15$. For bare sea ice of thickness 1.5 m and $R_{ice} = +1$, broad band albedo changes from 0.648 to 0.671, a change of $+0.023$. For $R_{ice} = -1$, the change is from 0.648 to 0.620, a change of -0.028 . The corresponding albedos for $R_{ice} = +2$ and $R_{ice} = -2$ are 0.648 to 0.690 and 0.648 to 0.585, changes of $+0.042$ and -0.063 respectively. These changes are approximately consistent with Table 8; but note they are not linear about the mean. Note also that the visible band transmissivity to the ocean changes in the opposite sense to the broadband albedo, with about half the broadband change.

For ponded ice, we select $f_{ice}^{+} = 2.00$ and $f_{ice}^{-} = 0.50$. With sea ice of thickness 1.5 m and pond thickness 0.35, for $R_{ice} = +1$, broad band albedo changes from 0.193 to 0.262, a change of $+0.069$. For $R_{ice} = -1$, the change is from 0.193 to 0.153, a change of -0.040 . As with bare sea ice, these changes are approximately consistent with Table 8, but are non-linear about the mean.

For completeness, we also acknowledge that from the previous subsection, the two pond depths h_{pmin} and h_{p0} can be changed to modify the transition between bare ice and ponded ice for tuning purposes. Fig. 13 can be used as a guide as to how the transitional albedos will vary with changes in these two depths.

6. Delta-Eddington Solar Radiation Treatment: Comparisons

In this section, we compare solar radiation calculations between the Delta-Eddington solar radiation treatment and three other radiation methods: (1) SNICAR for snow-covered sea ice, (2) a Monte Carlo radiation model for bare sea ice, and (3) the present solar radiation scheme for sea ice in CCSM3 (section 2).

There are several reasons for making such comparisons. The Delta-Eddington solar radiation parameterization is an approximate solution to the spectral multiple scattering problem, albeit a reasonably good one (see section 4.3). It would be wise nevertheless to compare it against a more accurate calculation of spectral multiple scattering for several idealized cases. Close agreement would then increase confidence in the accuracy of the Delta-Eddington solar radiation parameterization, and also give some guidance as to the absolute accuracy of the approximation.

In addition, the approximate method of representing refraction in sea ice (section 4.1) needs to be checked against a radiation model that more accurately calculates the angular details of multiple scattering across the refractive boundary. The large number of angles required for convergent calculation of diffuse reflectivity below the refractive boundary (see end of section 4.1 and Eq. 25) is an indication of how sensitive the results may be to angular resolution.

Finally, it is of great interest to compare radiation calculations with the present solar radiation scheme for sea ice in CCSM3 against those of the Delta-Eddington solar radiation parameterization. The discussion in section 2 highlighted the shortcomings of the present solar radiation method in sea ice for CCSM3, but more from a fundamental theoretical point of view; in this section, we compare actual radiation calculations between the two methods.

For most of these comparisons, the broadband Delta-Eddington albedos are computed employing an atmosphere radiation model above the surface that has a typical polar atmosphere profile. This allows a realistic assessment of multiple scattering between the surface sea ice system and the atmosphere above, for both clear sky and overcast conditions. The spectral partition between visible and near-infrared, which is important when comparing broadband absorption, is more accurately assessed when such an atmosphere radiation model is used above the sea ice system. The atmosphere radiation model also allows an accurate calculation of the partition between direct and diffuse solar radiation incident on the surface, in a manner similar to that of CCSM3, allowing the full use of the direct/diffuse dependencies of the Delta-Eddington solar radiation parameterization. If an atmosphere radiation model above the surface is not used, then one has to make some assumptions about surface/atmosphere multiple scattering and spectral partition in order to specify the atmosphere solar radiation fluxes. Hence, using the atmosphere radiation model yields a self-consistent calculation of both solar radiation absorption within the

surface sea ice system as well as multiple scattering between the surface and atmosphere, which is a dominant factor determining the values of the four solar radiation fluxes (Eq. 1).

In section 6.1 we compare albedos and absorptions between the Delta-Eddington solar radiation parameterization and SNICAR, a benchmark radiative transfer model of snow (Flanner et al. 2006). This model computes radiative transfer through snow assuming equivalent ice spheres over a log-normal size distribution about a specified effective radius, using 470 spectral bands, for each of which Mie parameters were pre-computed for each radius. The multiple scattering is evaluated using a two-stream solution. The incident solar irradiance is taken from a narrow-band atmospheric radiative transfer model for mid-latitude winter conditions for both clear and overcast skies. We consider this a benchmark model for snow radiative transfer, which treats spectral variation of both incident solar irradiance and the IOPs of snow grains in great detail. For this comparison, the Delta-Eddington solar radiation treatment for snow can be considered as a three band mono-disperse (i.e. single grain size which equals the effective radius) approximation.

In section 6.2 we present comparisons of albedos between the Delta-Eddington solar radiation parameterization and a benchmark Monte Carlo radiation model. The Monte Carlo radiation model of Light et al. (2003b) is used. This model is a highly angularly resolved model, whereas the Delta-Eddington method (see around Eqs. 48,49) is very smooth in its representation of the angular dependence of multiply scattered radiation. Because the Monte Carlo model typically resolves the cosine zenith angle μ from +1 to -1 by 140 separate streams of radiation, we refer to it as a benchmark, or standard, model for sea ice. We use identical inherent optical properties in both models to insure that the basic differences between the two calculations are confined to the angular resolution of the radiation and the solution technique. Additionally, the Monte Carlo model is able to resolve the angular details of the radiation across the refractive boundary, and therefore does not compute diffuse radiation as does the approximate Delta-Eddington scheme (see Eqs. 23,24 and the moment calculation following Eqs. 48,49).

In section 6.3 we compare not only albedos but also transmissions and absorbed fluxes between Delta-Eddington solar radiation and the the present solar radiation scheme for sea ice in CCSM3, for realistic polar conditions. The atmosphere radiation model and polar atmosphere profile used in this comparison is presented in Appendix C. These comparisons give an indication of how the Delta-Eddington solar radiation parameterization might differ compared to the present sea ice solar radiation when used in fully-coupled CCSM3 integrations.

6.1 Benchmark Radiation Model for Snow: SNICAR

We compare snow-over-sea ice with 0.3 m deep snow and sea ice thickness 1.5 m in Table 17. The snow surface scattering layer is 0.04 m thick. The absorption of this layer is

Table 17. Delta-Eddington (DE) and SNICAR comparison. Surface (srfc) snow layer .04 m thick, total snow depth 0.3 m, sea ice thickness 1.5 m, solar zenith angle 60° for 20 May at 80N latitude. For various snow grain radii r_s . Fluxes in Wm^{-2} .

(a) Clear Sky. For DE, Appendix C atmospheric profile without cloud layer.

Flux and Albedo	DE(50 μm)	SNICAR(50 μm)	DE(500 μm)	SNICAR(500 μm)
solar irradiance	516.4	516.4	513.7	513.7
broad band albedo	0.865	0.860	0.755	0.754
vs/ni absorbed	3.7/66.0	3.4/69.2	12.8/113.2	11.7/114.7
snow SSL absorbed	67.4	70.6	102.1	108.4
snow INT absorbed	2.3	1.9	18.0	13.7
sea ice absorbed	0.1	0.1	5.9	4.5

Flux and Albedo	DE(1000 μm)	SNICAR(1000 μm)	DE(2000 μm)	SNICAR(2000 μm)
solar irradiance	512.3	512.3	510.3	510.3
broad band albedo	0.710	0.710	0.658	0.658
vs/ni absorbed	19.4/129.3	17.8/130.7	28.7/145.8	26.8/147.6
snow SSL absorbed	106.9	116.2	108.1	120.8
snow INT absorbed	29.9	22.4	45.0	34.3
sea ice absorbed	11.9	10.0	21.4	19.3

(b) Overcast Sky. For DE, Appendix C atmospheric profile, and $r'_s = 0.8r_s$.

Flux and Albedo	DE(40 μm)	SNICAR(50 μm)	DE(400 μm)	SNICAR(500 μm)
solar irradiance	376.9	376.9	341.1	341.1
broad band albedo	0.916	0.921	0.841	0.844
vs/ni absorbed	3.3/28.5	3.2/26.6	10.5/43.8	10.4/42.9
snow SSL absorbed	30.0	28.0	39.4	40.1
snow INT absorbed	1.8	1.7	10.6	9.2
sea ice absorbed	0.0	0.1	4.2	4.1

Flux and Albedo	DE(800 μm)	SNICAR(1000 μm)	DE(1600 μm)	SNICAR(2000 μm)
solar irradiance	326.1	326.1	308.7	308.7
broad band albedo	0.805	0.807	0.759	0.758
vs/ni absorbed	15.3/48.2	15.4/47.6	21.9/52.4	22.0/52.6
snow SSL absorbed	38.6	41.0	35.8	40.6
snow INT absorbed	16.3	13.6	23.3	18.9
sea ice absorbed	8.7	8.3	15.2	15.1

termed the surface absorption. We consider both clear sky and overcast sky conditions with cosine solar zenith angle $\mu_0 = 0.5$. The Delta-Eddington solar radiation calculations use the polar atmosphere of Table C for May 20 at 80N latitude; clear sky removes the cloud layer. For clear sky, the Delta-Eddington calculations use r_s without scaling (i.e. $f_r = 1$ in Eq. 68), while for overcast sky the best agreement with SNICAR results is obtained for $f_r = 0.8$. We note that a solar irradiance was used for the band average albedos (see section 5.2A), and therefore it is not surprising that the clear and overcast comparisons should differ. Overcast sky generally has less near-ir absorption due to water vapor and cloud, and so the band albedos which are in close agreement for clear sky will tend to over-absorb for overcast sky. By scaling the grain size down with $f_r = 0.8$, we reduce the absorption in DE and improve agreement with SNICAR.

The resulting broad band albedos between DE and SNICAR agree very well. However, in nearly every case, the Delta-Eddington solar under absorbs in the snow surface layer around 10%, while over absorbing in the snow interior up to 30% and in the underlying sea ice up to 10%, compared to SNICAR. The under/over absorption biases are larger in the clear sky than in the overcast comparison. The differences in the vertical profile of absorption is not unexpected for just 3 spectral bands in DE compared to 470 for SNICAR. Though adding a few more spectral bands in DE would likely improve the vertical profile, we consider 30% accuracy in vertical absorption profile for snow acceptable considering other uncertainties and computational constraints.

We finally note that to most accurately calculate snow layer albedo and absorption for both clear and overcast sky, we can use the ratio of direct to total near-ir incident solar irradiance (as used in section 5.1 to combine the two near-ir bands) to weight the scaling factor f_r between clear sky value of 1.0 and overcast sky value of 0.8.

6.2 Benchmark Radiation Model for Sea Ice: Monte Carlo

We consider first an idealized case available for comparison from the Monte Carlo calculations of Light et al. (2003b). This case is that of radiation of specified wavelength incident normally (i.e. perpendicularly) on a single horizontally uniform slab. The slab thickness and inherent optical properties are specified. Both non-refractive and refractive slabs are considered. The non-refractive slab consists of granular scatterers and absorbers; the refractive slab has the same number of scatterers and absorbers, but the slab index of refraction is $n = 1.31$ (section 4.1). In other words, both non-refractive and refractive conditions have the same optical depth τ , single scattering albedo ω , and asymmetry parameter g for the slab, but differ in the index of refraction, $n = 1$ and $n = 1.31$ respectively. Results for a purely scattering slab (i.e. no absorption) for both isotropic scattering $g = 0$ and strong forward scattering $g = 0.95$, are shown in Table 18. The isotropic scattering case is of more theoretical interest, while the strong forward scattering case is more applicable to sea ice.

Table 18 shows that the Delta-Eddington solar radiation parameterization results compare well with those of the Monte Carlo benchmark calculations. For the case of isotropic scattering and no refraction (first two columns of Table 18), the absolute differences are very small, less than .005. For isotropic scattering and refraction (next two columns) the absolute differences are as large as .01 . This shows that our method of accounting for refraction (section 4.1) introduces some error. The case of strong forward scattering but no refraction (next two columns) have errors less than .008, while the case of strong forward scattering with refraction (last two columns), the most realistic case for sea ice, has errors as large as .02 . We note that the Delta-Eddington solar radiation albedos are systematically higher than the Monte-Carlo, suggesting that there is not enough radiation trapped by refraction in our approximation (section 4.1; because of total internal reflection of diffusely scattered upward radiation below the refractive boundary, radiation transmitting the refractive boundary is partially “trapped” below it). Despite the errors, the overall increase in albedo with optical depth is represented very well.

Table 18. Radiative Model Comparisons: Delta-Eddington and Monte Carlo Albedos. Normally incident beam on a non-absorbing but scattering slab of specified optical thickness τ and asymmetry parameter g . For the refractive slab, $n=1.31$. DEG=Delta-Eddington granular; DER=Delta-Eddington refractive; MCG=Monte Carlo granular; MCR=Monte Carlo refractive. Monte Carlo results from Light et al. (2003b).

τ	$g = 0$ DEG	$g = 0$ MCG	$g = 0$ DER	$g = 0$ MCR	$g = .95$ DEG	$g = .95$ MCG	$g = .95$ DER	$g = .95$ MCR
1	.338	.341	.341	.340	.014	.012	.058	.055
2	.514	.518	.490	.480	.029	.025	.088	.077
5	.737	.736	.680	.681	.077	.071	.164	.145
10	.853	.852	.799	.805	.159	.152	.258	.242
20	.922	.924	.884	.893	.306	.307	.377	.367
50	.968	.970	.950	.955	.566	.568	.548	.544

The results comparing an absorbing slab are given in Table 19. In this case, only refractive slab results are shown for strong forward scattering $g = 0.95$. The single scattering values ω are typical for sea ice, and corresponding wavelengths are also shown. Absolute differences in the Delta-Eddington solar radiation albedos compared to the Monte Carlo are less than .007 . We note again that the Delta-Eddington albedos are systematically higher than the Monte Carlo.

Table 19. Spectral Radiative Model Comparisons: Delta-Eddington and Monte Carlo Albedos. Normally incident beam on a refractive slab ($n=1.31$) of specified optical thickness τ and single scattering albedo ω . Asymmetry parameter $g=0.95$. λ is wavelength in nanometers. DE=Delta-Eddington; MC=Monte Carlo. Monte-Carlo results from Light et al. (2003b).

λ	τ	ω	DE	MC
500	37.51	0.9998	.481	.474
600	37.52	0.9995	.463	.458
700	37.58	0.9979	.386	.379
800	37.81	0.9917	.229	.221
900	38.38	0.9771	.114	.107
1000	40.55	0.9247	.044	.040

Finally, we compare spectral radiative model albedos between Delta-Eddington and Monte Carlo in Table 20. These comparisons use the full vertical profile for bare ice (Table 12). To compare the effect of refraction and its vertical location, we perform an additional three comparisons, as shown in Table 20: with no refraction at all (first row), with the refractive boundary at the top sea ice surface (second row), with the refractive boundary at the standard level (third row), and with the refractive boundary one level below the standard level (fourth row). The Monte Carlo calculations also include the effects of refraction, where appropriate.

When no refractive boundary is present, spectral band albedos agree to better than .016 absolute (first row of Table 20). Notice how the $0.7 - 1.19\mu m$ band nicely represents the intermediate effects between the highly scattering visible band and the strongly absorbing $1.19 - 5.0\mu m$ far infrared band. When the refractive boundary is placed at the top of the ice (second row of Table 20), the Delta-Eddington errors are larger, particularly in the $0.7 - 1.19\mu m$ spectral band, indicating that our Delta-Eddington refraction method is only approximate. Notice how the refractive boundary “traps” radiation below it due to total internal reflection, resulting in lower albedos (e.g. compare the first and second rows of Table 20), for both the Delta-Eddington solar radiation and for the Monte Carlo. However, the Delta-Eddington solar refraction does not trap sufficient radiation below the refractive boundary, resulting in slightly higher albedos compared to the Monte Carlo. For the standard position (top of the $3/4$ layer, the third row of Table 20), the errors are order .01 absolute. Of course, as expected, when the refractive boundary is even deeper in the ice, the effects of refraction on the albedo are reduced even more (first, second and fourth rows of Table 20).

Table 20. Spectral Radiative Model Comparisons: Delta-Eddington and Monte Carlo Albedos. Diffuse incident radiation for bare sea ice with layer structure given in Table 1 and IOPs from Table 12. Refraction is either absent, or the refractive boundary ($n = 1.31$) is placed at various interfaces as indicated. DE=Delta-Eddington; MC=Monte Carlo. The Monte Carlo calculation also includes the effects of refraction, as indicated. Note that the third row of results is the most applicable to sea ice as modeled in this work, as in Table 1. Sea ice thickness 1.5 m.

Type	$0.2 - 0.7\mu m$	$0.7 - 1.19\mu m$	$1.19 - 5.0\mu m$
No refraction			
DE	.781	.551	.100
MC	.765	.556	.104
Refraction at top of 1/4			
DE	.682	.438	.117
MC	.650	.410	.091
Refraction at top of 3/4			
DE	.754	.551	.100
MC	.742	.558	.104
Refraction at top of 2			
DE	.777	.551	.100
MC	.759	.557	.104

In summary, these comparisons show that the Delta-Eddington solar radiation is a good approximation to the scattering and absorption of solar radiation in sea ice, even when a refractive boundary is included below the surface scattering layer. The errors in the spectral albedos are nearly always less than .01 absolute.

6.3 Present Version of Solar Radiation in CCSM Sea Ice

In this subsection we compare albedos, absorption and transmission between the Delta-Eddington solar radiation treatment and the present solar radiation scheme for sea ice in CCSM3. The atmosphere radiation model and polar atmosphere profile used in this comparison is presented in Appendix C. We use the atmosphere radiation model to provide a self-consistent calculation of multiple scattering between the surface and atmosphere for a typical polar atmosphere profile, both for clear and overcast sky.

We first consider several snow-overlying-sea ice cases, then thick bare sea ice and ponded sea ice, as shown in Table 21. The broadband albedos shown in this table are determined from the summed band absorbed fluxes (Eq. 56) and the summed band downward solar fluxes (Eq. 1): $\alpha_{bb} = 1 - (F_{SW}/F_{SWDN})$. Broadband and spectral band albedos are compared in Table 21. We include a range of snow grain radii in these comparisons, and note that the Delta-Eddington solar radiation albedos bracket the CCSM3 albedos for non-melting and melting snow. The bare sea ice Delta-Eddington albedos are larger than those of CCSM3, while the ponded ice albedos are smaller.

Fig. 14 shows modeled and observed broadband albedo as a function of bare ice thickness. Figs. 15 and 16 show modeled I_0 (see Eqs. 13,14) and transmittance as functions of ice thickness, respectively. The ice thicknesses less than 0.10 m are shown only to highlight very thin ice thickness, as CCSM3 limits the ice to thicker than 0.10 m. Fig. 14 shows that both CCSM3 and the Delta-Eddington solar radiation represent the albedo dependence on ice thickness similarly given the limited data. Note that the Delta-Eddington thin ice albedo asymptotes to 0.063, the diffuse Fresnel layer refraction albedo (see section 4.1), a value also appropriate for the ocean. Thus, the thin ice refraction layer becomes that for the ocean surface in the thin ice limit. The Delta-Eddington I_0 values of Fig. 15 are shown only for comparison with CCSM3, as they are not directly used in the solution, but it does show how variable this quantity is and how poor an approximation is the constant value of CCSM3. Notice how different the ice transmissions are between the two models in Fig. 16. The Delta-Eddington solar radiation even allows some near-infrared radiation to penetrate all the way through the thinnest ice to the underlying ocean, while CCSM3 allows no penetration beyond the surface layer. CCSM3 is less transmissive in the visible than is the Delta-Eddington.

Table 22 and Figs. 17a-c compare internal sea ice and ocean absorption between Delta-Eddington and CCSM3 for three ice thicknesses. Shown are computed fluxes for the atmospheric profile and seasonal data presented in Appendix C. In general, the Delta-Eddington absorbs less in the surface layer than CCSM3 and more in the ice and the underlying ocean. This is particularly true for the thinnest ice.

Table 21. Broadband and Spectral Delta-Eddington and CCSM3 Albedos for various surface types. “bb” is broadband, “vs” visible and “ni” near-infrared. Atmosphere radiation model and profile (Appendix C) has an overcast low stratus cloud. The solar zenith angle is 60° . The Delta-Eddington albedos are for diffuse incident radiation; DE=Delta-Eddington, with h_i =sea ice thickness, h_p =pond depth and h_s =snow depth. The ponded ice albedos for CCSM3 were inferred from the grid box albedos assuming 30% coverage by ponds. $\times 1$ refers to the nominally $1^\circ \times 1^\circ$ horizontal resolution of sea ice in CCSM3.

Type	vs $0.2 - 0.7\mu m$	ni $0.7 - 5.0\mu m$	bb(overcast) $0.2 - 5.0\mu m$	bb(clear) $0.2 - 5.0\mu m$
Snow on Sea Ice				
DE ($r_s = 50\mu m$, $h_s = 0.3m$)	.985	.772	.910	.865
CCSM3 non-melting ($\times 1$)	.946	.658	.848	.808
DE ($r_s = 500\mu m$, $h_s = 0.3m$)	.948	.581	.830	.755
DE ($r_s = 1000\mu m$, $h_s = 0.3m$)	.921	.509	.791	.710
CCSM3 melting ($\times 1$)	.847	.513	.734	.686
DE ($r_s = 2500\mu m$, $h_s = 0.3m$)	.869	.410	.726	.640
Bare Sea Ice				
DE ($h_i = 1.5m$)	.754	.452	.647	.610
CCSM3 non-melting ($\times 1$)	.73	.33	.595	.535
Pond on Sea Ice				
DE ($h_p = 0.35m$, $h_i = 1.5m$)	.274	.063	.192	.156
CCSM3 (see above) ($\times 1$)	.48	.08	.345	.302

In addition to sea ice thickness, the sea ice albedo depends on snow depth, meltpond depth, and solar zenith angle. None of these dependencies is in the present solar radiation parameterization in CCSM3 (see section 2).

Fig. 18 shows the zenith angle dependence of broadband Delta-Eddington albedos for clear sky conditions for snow, bare sea ice and pond (snow and pond completely cover sea ice). Note that CCSM3 has no zenith angle dependence. The zenith angle dependencies range from order .05 for snow, .10 for bare ice and .20 for pond, for low to moderately high sun ($\mu_0 = .68$ is appropriate for local noon on summer solstice at latitude 67°). Because the low stratus cloud is optically thick (Appendix C), there is virtually no direct radiation for this case, and thus this dependence is not realized for overcast sky.

Table 22. Sea ice absorption: Delta-Eddington and CCSM3(x1), Wm^{-2} . Total column and by level. DE=Delta-Eddington. Atmospheric profile (Appendix C) has an overcast low stratus cloud. The solar radiation zenith angle 60° .

(a) Ice thickness 0.1 m. Downwelling surface solar radiation is 192.9 Wm^{-2} , with visible and near-infrared fractions .588 and .412 respectively for DE. $\alpha_{\text{bb}}(\text{DE})=0.242$

Level	DE vs	CCSM3 vs	DE ni	CCSM3 ni	DE bb	CCSM3 bb
total	81.9	81.4	63.5	65.2	145.4	146.6
surface	0.1	24.4	17.0	65.2	17.1	89.6
1	0.8	2.0	13.2	0	14.0	2.0
2	0.9	1.9	10.1	0	11.0	1.9
3	0.8	1.8	7.0	0	7.8	1.8
4	33.0	1.8	4.8	0	37.8	1.8
ocn	46.7	49.5	11.5	0	58.2	49.5

(b) Ice thickness 1.0 m. Downwelling surface solar radiation is 258.7 Wm^{-2} , with visible and near-infrared fractions .636 and .364 respectively for DE. $\alpha_{\text{bb}}(\text{DE})=0.594$

Level	DE vs	CCSM3 vs	DE ni	CCSM3 ni	DE bb	CCSM3 bb
total	50.8	46.5	54.0	58.5	104.8	105.3
surface	1.3	13.9	33.6	58.5	34.9	72.4
1	9.7	9.6	19.8	0	29.5	9.9
2	5.8	6.8	0.6	0	6.4	6.8
3	4.1	4.8	0	0	4.1	4.8
4	14.8	3.4	0	0	14.8	3.4
ocn	15.3	8.0	0	0	15.3	8.0

(c) Ice thickness 5.0 m. Downwelling surface solar radiation is 275.7 Wm^{-2} , with visible and near-infrared fractions .651 and .349 respectively for DE. $\alpha_{\text{bb}}(\text{DE})=0.658$

Level	DE vs	CCSM3 vs	DE ni	CCSM3 ni	DE bb	CCSM3 bb
total	41.7	46.3	52.6	58.5	94.3	104.8
surface	2.2	13.9	39.6	58.5	41.8	72.4
1	34.2	26.8	13.0	0	47.2	26.8
2	3.5	4.7	0	0	3.5	4.7
3	1.1	0.8	0	0	1.1	0.8
4	0.5	0.1	0	0	0.5	0.1
ocn	0.2	0	0	0	0.2	0

7. Summary

We have presented an alternate approach for calculating solar radiation in CCSM sea ice. It is based on the Delta-Eddington solar radiation treatment of representing multiple scattering (see Table 2). The Delta-Eddington solar radiation treatment allows surface types of snow over sea ice, bare melting sea ice, and ponded ice. Our approach makes use of inherent optical properties from equivalent ice spheres for snow, and from SHEBA spectral surface albedo and physical ice measurements for sea ice. The SHEBA spectral surface albedo measurements allow for characterization of variability in IOPs which can be used in tuning procedures. Comparisons with SNICAR calculations for snow-over-sea ice show that the Delta-Eddington solar radiation is a very good approximation for snow radiative transfer, with albedo errors less than .01 absolute. Comparisons with benchmark theoretical calculations which accurately resolve multiple scattering and the effects of refraction show that the Delta-Eddington solar radiation is a good approximation for sea ice radiative transfer, with albedo errors usually less than .02 absolute. Comparisons of the Delta-Eddington solar radiation treatment with the present solar radiation parameterization in CCSM3 sea ice illustrate the inaccuracies and limitations of the latter. These comparisons show that, relative to the present solar radiation treatment in CCSM3 sea ice, the Delta-Eddington solar radiation treatment produces less absorption near the surface and more with depth. The response of the climate in CCSM3 to this solar radiation treatment must await further development in the sea ice component of CCSM. Because of their importance for solar radiation reflection and absorption in sea ice, developments in snow modeling to allow prognostic snow density and grain size in a multi-layer parameterization, and in meltpond modeling to allow prognostic pond fraction and depth, are key. New developments in these areas, in combination with the Delta-Eddington solar radiation treatment, should result in significant improvements in the modeling of the snow/sea ice albedo feedback in CCSM. The Delta-Eddington solar radiation treatment also allows incorporation of additional absorbers, such as carbon soot.

It is concluded that using the Delta-Eddington solar radiation treatment in place of the present parameterization in CCSM sea ice would result in a significant improvement in sea ice solar radiation accuracy, consistency and generality. We strongly hope that this treatment will be included in future versions of CCSM sea ice. It could also be applied profitably to other sea ice models as well.

Acknowledgments B.Light gratefully acknowledges support for this work through the NSF Climate Dynamics Program SGER grant ATM-0454311. We thank the many members of the Polar Climate Working Group of CCSM who have contributed to this work. In particular, we thank M.M.Holland, D.Bailey, C.M.Bitiz, R.E.Moritz, and A.Conley for many fruitful discussions. C.M.Bitiz contributed numerous comments which significantly improved this document. S.Warren made ice sphere Mie calculations available, D.Perovich contributed an observed solar irradiance, and M.Flanner made SNICAR results available.

Appendix A: Delta-Eddington Solution for a Single Layer

We present here the detailed solution of the scaled, direct/diffuse split radiative transfer equation (Eq. 47) that leads to the reflectivities and transmissivities in Eqs. 50.

Consider a homogeneous plane-parallel layer of scaled optical depth τ_0^* , single scattering albedo $\omega^* < 1$ and asymmetry parameter g^* . Optical depth is taken as $\tau^* = 0$ at top and $\tau^* = \tau_0^*$ at bottom. Angles are referred against the normal to the layer, with cosine zenith angle $\mu = -1$ vertically upwards, and $\mu = +1$ vertically downwards. We consider the layer to have index of refraction $n > 1$ and to be embedded within a medium of the same index of refraction, so refraction effects at the boundaries can be ignored.

The boundary conditions are no upwelling direct or diffuse fluxes at the bottom, but incident direct solar radiation flux at the top of $\pi F_0 \mu_{0n}$ where $\mu_{0n} > 0$ is the cosine of the solar zenith angle in the medium, and incident diffuse flux at the top F_{top} . The scaled, direct/diffuse split radiative transfer equation to be solved is:

$$\mu \frac{dI}{d\tau^*} + I = \frac{\omega^*}{2} \int_{-1}^{+1} (1 + 3g^* \mu \mu') I d\mu' + \frac{\omega^* F_0}{4} (1 + 3g^* \mu_{0n} \mu) e^{-\tau^*/\mu_{0n}} \quad (A1)$$

We invoke the Eddington approximation: $I = I_0 + \mu I_1$, where I_0 is the mean intensity, and I_1 is three times the mean flux:

$$\begin{aligned} I_0 &= \frac{1}{4\pi} \int_{4\pi} I d\Omega = \frac{1}{2} \int_{-1}^{+1} I(\mu) d\mu \\ I_1 &= \frac{3}{4\pi} \int_{4\pi} \mu I d\Omega = \frac{3}{2} \int_{-1}^{+1} \mu I(\mu) d\mu \end{aligned} \quad (A2)$$

Thus, Eq. A1 can be written:

$$\mu \frac{dI_0}{d\tau^*} + \mu^2 \frac{dI_1}{d\tau^*} + I_0 + \mu I_1 = \omega^* I_0 + \omega^* g^* \mu I_1 + \frac{\omega^* F_0}{4} (1 + 3g^* \mu_{0n} \mu) e^{-\tau^*/\mu_{0n}}$$

or

$$\mu \left\{ \frac{dI_0}{d\tau^*} + (1 - \omega^* g^*) I_1 \right\} + \mu^2 \frac{dI_1}{d\tau^*} + (1 - \omega^*) I_0 = \frac{\omega^* F_0}{4} (1 + 3g^* \mu_{0n} \mu) e^{-\tau^*/\mu_{0n}} \quad (A3)$$

Using the integrals:

$$\int_{-1}^{+1} d\mu = 2 \quad \int_{-1}^{+1} \mu d\mu = 0 \quad \int_{-1}^{+1} \mu^2 d\mu = 2/3 \quad \int_{-1}^{+1} \mu^3 d\mu = 0 \quad (A4)$$

we separate the transfer equation by taking moments $\int_{-1}^{+1} d\mu$ and $\int_{-1}^{+1} \mu d\mu$:

$$\begin{aligned} \frac{dI_1}{d\tau^*} + 3(1 - \omega^*) I_0 &= \frac{3}{4} \omega^* F_0 e^{-\tau^*/\mu_{0n}} \\ \frac{dI_0}{d\tau^*} + (1 - \omega^* g^*) I_1 &= \frac{3}{4} \omega^* g^* \mu_{0n} F_0 e^{-\tau^*/\mu_{0n}} \end{aligned} \quad (A5)$$

For convenience in applying flux boundary conditions, we transform these transfer equations into flux forms. The downward and upward diffuse fluxes, F^\downarrow and F^\uparrow respectively,

can be written:

$$\begin{aligned} F^\downarrow &= 2\pi \int_0^{+1} \mu I \, d\mu = 2\pi \int_0^{+1} \mu(I_0 + \mu I_1) \, d\mu = \pi I_0 + \frac{2\pi}{3} I_1 \\ F^\uparrow &= 2\pi \int_0^{-1} \mu I \, d\mu = 2\pi \int_0^{-1} \mu(I_0 + \mu I_1) \, d\mu = \pi I_0 - \frac{2\pi}{3} I_1 \end{aligned} \quad (A6)$$

We define the functions G and H by:

$$\begin{aligned} G &= \pi I_0 \\ H &= \frac{2\pi}{3} I_1 \end{aligned} \quad (A7)$$

so that the downward and upward diffuse fluxes can be expressed by:

$$\begin{aligned} F^\downarrow &= G + H \\ F^\uparrow &= G - H \end{aligned} \quad (A8)$$

Using the definitions of G and H , the transfer equations A5 become:

$$\begin{aligned} \frac{dH}{d\tau^*} + 2(1 - \omega^*)G &= \frac{1}{2} \omega^* S e^{-\tau^*/\mu_{0n}} \\ \frac{dG}{d\tau^*} + \frac{3}{2}(1 - \omega^* g^*)H &= \frac{3}{4} \omega^* g^* \mu_{0n} S e^{-\tau^*/\mu_{0n}} \end{aligned} \quad (A9)$$

where $S = \pi F_0$. These are two first-order coupled ordinary differential equations for the unknown functions $H = H(\tau^*)$ and $G = G(\tau^*)$. Taking the optical depth derivatives of these two equations and eliminating the first-order derivative terms results in:

$$\begin{aligned} \frac{d^2 H}{d\tau^{*2}} - 3(1 - \omega^*)(1 - \omega^* g^*)H &= -\frac{1}{2} \omega^* S \left\{ \frac{1}{\mu_{0n}} + 3g^* \mu_{0n}(1 - \omega^*) \right\} e^{-\tau^*/\mu_{0n}} \\ \frac{d^2 G}{d\tau^{*2}} - 3(1 - \omega^*)(1 - \omega^* g^*)G &= -\frac{3}{4} \omega^* S \{1 + g^*(1 - \omega^*)\} e^{-\tau^*/\mu_{0n}} \end{aligned} \quad (A10)$$

Let

$$\lambda^2 = 3(1 - \omega^*)(1 - \omega^* g^*) \quad \bar{\alpha} = \frac{\frac{3}{4} \omega^* S \{1 + g^*(1 - \omega^*)\}}{\frac{1}{\mu_{0n}^2} - \lambda^2} \quad \bar{\beta} = \frac{\frac{1}{2} \omega^* S \left\{ \frac{1}{\mu_{0n}} + 3g^* \mu_{0n}(1 - \omega^*) \right\}}{\frac{1}{\mu_{0n}^2} - \lambda^2} \quad (A11)$$

so the second-order transfer equations can be written concisely as:

$$\begin{aligned} \frac{d^2 H}{d\tau^{*2}} - \lambda^2 H &= -(\frac{1}{\mu_{0n}^2} - \lambda^2) \bar{\alpha} e^{-\tau^*/\mu_{0n}} \\ \frac{d^2 G}{d\tau^{*2}} - \lambda^2 G &= -(\frac{1}{\mu_{0n}^2} - \lambda^2) \bar{\beta} e^{-\tau^*/\mu_{0n}} \end{aligned} \quad (A12)$$

where the definitions of $\bar{\alpha}$ and $\bar{\beta}$ allow for solutions to the inhomogeneous equations. For the homogeneous equations (i.e. $\bar{\alpha} = \bar{\beta} = 0$), $C_1 e^{+\lambda\tau^*} + C_2 e^{-\lambda\tau^*}$ is a solution for G , where C_1 and C_2 are constants to be determined by the boundary conditions. Using the first-order equation for G implies that the solution for H is $-PC_1 e^{+\lambda\tau^*} + PC_2 e^{-\lambda\tau^*}$ where P is a constant. Thus, the combined homogeneous and inhomogeneous solutions are:

$$\begin{aligned} G(\tau^*) &= C_1 e^{+\lambda\tau^*} + C_2 e^{-\lambda\tau^*} - \bar{\alpha} e^{-\tau^*/\mu_{0n}} \\ H(\tau^*) &= -PC_1 e^{+\lambda\tau^*} + PC_2 e^{-\lambda\tau^*} - \bar{\beta} e^{-\tau^*/\mu_{0n}} \\ P &= \frac{2}{3} \frac{\lambda}{1 - \omega^* g^*} \end{aligned} \quad (A13)$$

Using Eqs. A8 for the downward and upward diffuse fluxes, we can write the solutions:

$$\begin{aligned} F^\downarrow &= G + H = C_1(1 - P)e^{+\lambda\tau^*} + C_2(1 + P)e^{-\lambda\tau^*} - \bar{\alpha}e^{-\tau^*/\mu_{0n}} - \bar{\beta}e^{-\tau^*/\mu_{0n}} \\ F^\uparrow &= G - H = C_1(1 + P)e^{+\lambda\tau^*} + C_2(1 - P)e^{-\lambda\tau^*} - \bar{\alpha}e^{-\tau^*/\mu_{0n}} + \bar{\beta}e^{-\tau^*/\mu_{0n}} \end{aligned} \quad (A14)$$

Consider first the case of incident direct solar radiation from above, but no incident diffuse fluxes. The boundary conditions for the diffuse fluxes $F^\downarrow(\tau^*)$ and $F^\uparrow(\tau^*)$ are:

$$F^\downarrow(0) = G(0) + H(0) = 0 \quad F^\uparrow(\tau_0^*) = G(\tau_0^*) - H(\tau_0^*) = 0 \quad (A15)$$

resulting in the coupled equations:

$$\begin{aligned} C_1(1 - P) + C_2(1 + P) - \bar{\alpha} - \bar{\beta} &= 0 \\ C_1(1 + P)e^{+\lambda\tau_0^*} + C_2(1 - P)e^{-\lambda\tau_0^*} - \bar{\alpha}e^{-\tau_0^*/\mu_{0n}} + \bar{\beta}e^{-\tau_0^*/\mu_{0n}} &= 0 \end{aligned} \quad (A16)$$

or

$$\begin{pmatrix} 1 - P & 1 + P \\ (1 + P)e^{+\lambda\tau_0^*} & (1 - P)e^{-\lambda\tau_0^*} \end{pmatrix} \begin{pmatrix} C_1 \\ C_2 \end{pmatrix} = \begin{pmatrix} \bar{\alpha} + \bar{\beta} \\ (\bar{\alpha} - \bar{\beta})e^{-\tau_0^*/\mu_{0n}} \end{pmatrix} \quad (A17)$$

The solutions to these coupled equations are:

$$\begin{aligned} C_1 &= \left| \begin{array}{cc} \bar{\alpha} + \bar{\beta} & 1 + P \\ (\bar{\alpha} - \bar{\beta})e^{-\tau_0^*/\mu_{0n}} & (1 - P)e^{-\lambda\tau_0^*} \end{array} \right| / D \\ &= \left\{ (\bar{\alpha} + \bar{\beta})(1 - P)e^{-\lambda\tau_0^*} - (1 + P)(\bar{\alpha} - \bar{\beta})e^{-\tau_0^*/\mu_{0n}} \right\} / D \end{aligned} \quad (A18)$$

$$\begin{aligned} C_2 &= \left| \begin{array}{cc} 1 - P & \bar{\alpha} + \bar{\beta} \\ (1 + P)e^{+\lambda\tau_0^*} & (\bar{\alpha} - \bar{\beta})e^{-\tau_0^*/\mu_{0n}} \end{array} \right| / D \\ &= \left\{ (1 - P)(\bar{\alpha} - \bar{\beta})e^{-\tau_0^*/\mu_{0n}} - (\bar{\alpha} + \bar{\beta})(1 + P)e^{+\lambda\tau_0^*} \right\} / D \end{aligned} \quad (A19)$$

$$D = (1 - P)^2 e^{-\lambda\tau_0^*} - (1 + P)^2 e^{+\lambda\tau_0^*} \quad (A20)$$

Consider the reflectivity to direct solar radiation at $\tau^* = 0$:

$$R(\mu_{0n}) = \frac{F^\uparrow(0)}{\pi F_0 \mu_{0n}} = \frac{G(0) - H(0)}{\pi F_0 \mu_{0n}} = \frac{C_1(1 + P) + C_2(1 - P) - \bar{\alpha} + \bar{\beta}}{S \mu_{0n}}$$

or

$$\begin{aligned} R(\mu_{0n}) &= \frac{1}{S \mu_{0n} D} \left\{ (\bar{\alpha} + \bar{\beta})(1 - P)(1 + P)e^{-\lambda\tau_0^*} - (1 + P)^2(\bar{\alpha} - \bar{\beta})e^{-\tau_0^*/\mu_{0n}} \right\} \\ &+ \frac{1}{S \mu_{0n} D} \left\{ (1 - P)^2(\bar{\alpha} - \bar{\beta})e^{-\tau_0^*/\mu_{0n}} - (\bar{\alpha} + \bar{\beta})(1 - P)(1 + P)e^{+\lambda\tau_0^*} \right\} \\ &- \frac{1}{S \mu_{0n}}(\bar{\alpha} - \bar{\beta}) \end{aligned} \quad (A21)$$

Collecting terms in $\bar{\alpha} + \bar{\beta}$ and $\bar{\alpha} - \bar{\beta}$:

$$\begin{aligned} R(\mu_{0n}) &= \frac{1}{S \mu_{0n} D} \left\{ (\bar{\alpha} - \bar{\beta}) \left[(1 - P)^2 - (1 + P)^2 \right] e^{-\tau_0^*/\mu_{0n}} \right\} \\ &+ \frac{1}{S \mu_{0n} D} \left\{ (\bar{\alpha} + \bar{\beta}) \left[(P + 1)(P - 1)e^{+\lambda\tau_0^*} - (P + 1)(P - 1)e^{-\lambda\tau_0^*} \right] \right\} \\ &- \frac{1}{S \mu_{0n}}(\bar{\alpha} - \bar{\beta}) \end{aligned} \quad (A22)$$

To facilitate comparison with Coakley et al. (1983), we define:

$$\begin{aligned}
u &= 1/P \\
\alpha &= \bar{\alpha}/S\mu_{0n} \\
\gamma &= \bar{\beta}/S\mu_{0n} \\
N &= -u^2 D = (u+1)^2 e^{+\lambda\tau_0^*} - (u-1)^2 e^{-\lambda\tau_0^*}
\end{aligned} \tag{A23}$$

Substituting into Eq. A22 we finally get:

$$\begin{aligned}
R(\mu_{0n}) &= (\alpha - \gamma)(4u/N)e^{-\tau_0^*/\mu_{0n}} + (\alpha + \gamma)(u+1)(u-1) \left[e^{+\lambda\tau_0^*} - e^{-\lambda\tau_0^*} \right] / N - (\alpha - \gamma) \\
\alpha &= \frac{3}{4}\omega^*\mu_{0n} \left(\frac{1+g^*(1-\omega^*)}{1-\lambda^2\mu_{0n}^2} \right) \\
\gamma &= \frac{1}{2}\omega^* \left(\frac{1+3g^*(1-\omega^*)\mu_{0n}^2}{1-\lambda^2\mu_{0n}^2} \right) \\
N &= (u+1)^2 e^{+\lambda\tau_0^*} - (u-1)^2 e^{-\lambda\tau_0^*} \\
u &= \frac{3}{2} \left(\frac{1-\omega^*g^*}{\lambda} \right) \\
\lambda &= \sqrt{3(1-\omega^*)(1-\omega^*g^*)}
\end{aligned} \tag{A24}$$

Consider the total transmissivity (i.e. both diffuse and direct) to direct solar radiation at $\tau^* = \tau_0^*$:

$$\begin{aligned}
T(\mu_{0n}) &= \frac{F^\downarrow(\tau_0^*)}{\pi F_0 \mu_{0n}} + e^{-\tau_0^*/\mu_{0n}} = \frac{G(\tau_0^*) + H(\tau_0^*)}{\pi F_0 \mu_{0n}} + e^{-\tau_0^*/\mu_{0n}} \\
&= \frac{1}{S\mu_{0n}D} \left[C_1(1-P)e^{+\lambda\tau_0^*} + C_2(1+P)e^{-\lambda\tau_0^*} - \bar{\alpha}e^{-\tau_0^*/\mu_{0n}} - \bar{\beta}e^{-\tau_0^*/\mu_{0n}} \right] + e^{-\tau_0^*/\mu_{0n}} \\
&= \frac{1}{S\mu_{0n}D} \left[(1-P)^2(\bar{\alpha} + \bar{\beta}) - (\bar{\alpha} - \bar{\beta})(1+P)(1-P)e^{-\tau_0^*/\mu_{0n}}e^{+\lambda\tau_0^*} \right] \\
&+ \frac{1}{S\mu_{0n}D} \left[(1-P)(\bar{\alpha} - \bar{\beta})(1+P)e^{-\tau_0^*/\mu_{0n}}e^{-\lambda\tau_0^*} - (\bar{\alpha} + \bar{\beta})(1+P)^2 \right] \\
&- \frac{1}{S\mu_{0n}D} \left[(\bar{\alpha} + \bar{\beta})e^{-\tau_0^*/\mu_{0n}} \right] + e^{-\tau_0^*/\mu_{0n}}
\end{aligned} \tag{A25}$$

Making the substitutions in Eqs. A23 and rearranging yields:

$$\begin{aligned}
T(\mu_{0n}) &= (\alpha + \gamma)(4u/N) + (\alpha - \gamma) \left[\frac{(u+1)(u-1)(e^{+\lambda\tau_0^*} - e^{-\lambda\tau_0^*})}{N} \right] e^{-\tau_0^*/\mu_{0n}} \\
&- (\alpha + \gamma - 1)e^{-\tau_0^*/\mu_{0n}}
\end{aligned} \tag{A26}$$

Now consider the case of diffuse incident flux. Then, $F_0 = 0$ for the direct solar radiation term, so that $\bar{\alpha} = \bar{\beta} = 0$. The boundary conditions are F_{top} from above and no flux from below. The coupled equations are:

$$\begin{aligned}
C_1(1-P) + C_2(1+P) &= F_{top} \\
C_1(1+P)e^{+\lambda\tau_0^*} + C_2(1-P)e^{-\lambda\tau_0^*} &= 0
\end{aligned} \tag{A27}$$

or

$$\begin{pmatrix} 1-P & 1+P \\ (1+P)e^{+\lambda\tau_0^*} & (1-P)e^{-\lambda\tau_0^*} \end{pmatrix} \begin{pmatrix} C_1 \\ C_2 \end{pmatrix} = \begin{pmatrix} F_{top} \\ 0 \end{pmatrix} \tag{A28}$$

The solutions are:

$$\begin{aligned} C_1 &= \begin{vmatrix} F_{top} & 1+P \\ 0 & (1-P)e^{-\lambda\tau_0^*} \end{vmatrix} / D = F_{top}(1-P)e^{-\lambda\tau_0^*} / D \\ C_2 &= \begin{vmatrix} 1-P & F_{top} \\ (1+P)e^{+\lambda\tau_0^*} & 0 \end{vmatrix} / D = -F_{top}(1+P)e^{+\lambda\tau_0^*} / D \end{aligned} \quad (A29)$$

The diffuse reflectivity is:

$$\begin{aligned} \overline{R} &= \frac{F^\uparrow(0)}{F_{top}} = \frac{G(0) - H(0)}{F_{top}} = \frac{C_1(1+P) + C_2(1-P)}{F_{top}} \\ &= \left[(1-P)(1+P)e^{-\lambda\tau_0^*} - (1+P)(1-P)e^{+\lambda\tau_0^*} \right] / D \\ &= \left[(u+1)(u-1)(e^{+\lambda\tau_0^*} - e^{-\lambda\tau_0^*}) \right] / N \end{aligned} \quad (A30)$$

The diffuse transmissivity is:

$$\begin{aligned} \overline{T} &= \frac{F^\downarrow(\tau_0^*)}{F_{top}} = \frac{G(\tau_0^*) + H(\tau_0^*)}{F_{top}} = \frac{C_1(1-P)e^{+\lambda\tau_0^*} + C_2(1+P)e^{-\lambda\tau_0^*}}{F_{top}} \\ &= (1-P)^2/D - (1+P)^2/D \\ &= 4u/N \end{aligned} \quad (A31)$$

using the substitutions from Eqs. A23.

Examination of Eq. A30 for the diffuse albedo shows that if $u < 1$ then \overline{R} will be negative (see Wiscombe and Warren, 1980). This occurs for strongly absorbing/scattering conditions of interest in the near-infrared. Simply setting $\overline{R} < 0$ diffuse reflectivities to 0 will bias the albedos low. Therefore, we perform a gaussian integration over angle of the positive definite reflectivity and transmissivity of Eqs. A24 and A25 respectively (assuming isotropic incident radiation):

$$\begin{aligned} \overline{R} &= 2 \int_0^{+1} \mu R(\mu) d\mu \\ \overline{T} &= 2 \int_0^{+1} \mu T(\mu) d\mu \end{aligned} \quad (A32)$$

Numerical experimentation shows that using 8 or more gaussian integration angles (e.g. 8 in the downwards hemisphere) results in an integration error less than .001. If necessary for numerical efficiency, 4 angles can be used but the integration errors increase to order .003. We chose 8 angles listed in Table A.

Table A. Gaussian Angles and Weights. Angles are given as cosine of zenith angle μ .

number	μ	weight
1	.9894009	.0271525
2	.9445750	.0622535
3	.8656312	.0951585
4	.7554044	.1246290
5	.6178762	.1495960
6	.4580168	.1691565
7	.2816036	.1826034
8	.0950125	.1894506

Note that a numerical integration of μ from 0 to 1 using the angles and weights in Table A yields .5015 (exact value .5000), showing that 8 angles gives accuracy in numerical integration of a few parts per thousand.

To summarize, we present the direct and diffuse reflectivities and transmissivities:

$$\begin{aligned}
R(\mu_{0n}) &= (\alpha - \gamma)(4u/N)e^{-\tau_0^*/\mu_{0n}} + (\alpha + \gamma)(u+1)(u-1) \left[e^{+\lambda\tau_0^*} - e^{-\lambda\tau_0^*} \right] / N - (\alpha - \gamma) \\
T(\mu_{0n}) &= (\alpha + \gamma)(4u/N) + (\alpha - \gamma) \left[\frac{(u+1)(u-1)(e^{+\lambda\tau_0^*} - e^{-\lambda\tau_0^*})}{N} \right] e^{-\tau_0^*/\mu_{0n}} \\
&\quad - (\alpha + \gamma - 1)e^{-\tau_0^*/\mu_{0n}} \\
\bar{R} &= 2 \int_0^1 \mu R(\mu) d\mu \\
\bar{T} &= 2 \int_0^1 \mu T(\mu) d\mu \\
\alpha &= \frac{3}{4} \omega^* \mu_{0n} \left(\frac{1 + g^*(1 - \omega^*)}{1 - \lambda^2 \mu_{0n}^2} \right) \\
\gamma &= \frac{1}{2} \omega^* \left(\frac{1 + 3g^*(1 - \omega^*) \mu_{0n}^2}{1 - \lambda^2 \mu_{0n}^2} \right) \\
N &= (u+1)^2 e^{\lambda\tau_0^*} - (u-1)^2 e^{-\lambda\tau_0^*} \\
u &= \frac{3}{2} \left(\frac{1 - \omega^* g^*}{\lambda} \right) \\
\lambda &= \sqrt{3(1 - \omega^*)(1 - \omega^* g^*)}
\end{aligned} \tag{A33}$$

Note that α and γ have a singularity at $\lambda = 1/\mu_{0n}$. For low precision machines (32bit) it is possible that this condition will occur for an integration with diurnal cycle (i.e. varying μ_{0n}). To insure against this, a small ϵ can be included, as $1 - \lambda^2 \mu_{0n}^2 + \epsilon$, with $\epsilon \sim 10^{-5}$, so that the solutions will be smooth across the singularity.

Appendix B: Solution for Multiple Layers

Appendix A presented the Delta-Eddington solution for a single layer; here we treat the multiple scattering solution between layers.

To combine apparent optical properties (AOPs) of two or more layers, we follow Coakley et al. (1983). Essentially, direct radiation once scattered within a layer (Appendix A) is assumed, upon exiting the layer, to be diffuse and isotropic over the hemisphere into which it is directed. We first treat the case of two layers which do not include a refractive boundary. Consider that layer 1 (with AOPs $[R_1(\mu_0) \ T_1(\mu_0) \ \bar{R}_1 \ \bar{T}_1]$) overlies layer 2 (with AOPs $[R_2(\mu_0) \ T_2(\mu_0) \ \bar{R}_2 \ \bar{T}_2]$), where μ_0 is the cosine zenith angle of the direct solar beam. Let $[R_{12}(\mu_0), T_{12}(\mu_0), \bar{R}_{12}, \bar{T}_{12}]$ be the AOPs for the combined layers. Note that the order 12 is important, signifying reflectivities and transmissivities due to radiation from above the combined layers, i.e. so layer 1 is encountered first. Let τ_1^* be the scaled optical depth of layer 1, and let the normalized diffuse upward and downward fluxes at the interface between layers be D^\uparrow and D^\downarrow respectively. For direct flux incident at cosine zenith angle μ_0 from above, normalized to 1 at the top interface of layer 1, and no incident diffuse flux, applying flux continuity at the interfaces we have:

$$\begin{aligned} R_{12}(\mu_0) &= R_1(\mu_0) + D^\uparrow \bar{T}_1 \\ D^\uparrow &= D^\downarrow \bar{R}_2 + e^{-\tau_1^*/\mu_0} R_2(\mu_0) \\ D^\downarrow &= D^\uparrow \bar{R}_1 + (T_1(\mu_0) - e^{-\tau_1^*/\mu_0}) \\ T_{12}(\mu_0) &= e^{-\tau_1^*/\mu_0} T_2(\mu_0) + D^\downarrow \bar{T}_2 \end{aligned} \tag{B1}$$

These equations can be understood term by term. The combined reflectivity of the two layers (1 over 2) to direct radiation from above at cosine zenith angle μ_0 ($R_{12}(\mu_0)$) is the direct reflectivity of layer 1 ($R_1(\mu_0)$) plus the upward diffuse flux at the interface between the two layers (D^\uparrow) times the diffuse transmissivity of layer 1 (\bar{T}_1). The upward diffuse flux at the interface between layers (D^\uparrow) is the downward diffuse flux at the interface (D^\downarrow) times the reflectivity of layer 2 to diffuse radiation (\bar{R}_2) plus the direct beam through layer 1 ($e^{-\tau_1^*/\mu_0}$) times the reflectivity of layer 2 to direct radiation ($R_2(\mu_0)$). The downward diffuse flux at the interface between layers (D^\downarrow) is the upward diffuse flux at the interface (D^\uparrow) times the reflectivity of layer 1 to diffuse radiation (\bar{R}_1) plus the diffuse portion of the direct beam transmitted through layer 1 ($T_1(\mu_0) - e^{-\tau_1^*/\mu_0}$). We note that $T_1(\mu_0)$ is the total transmission of the direct beam through layer 1, so if we subtract the direct beam $e^{-\tau_1^*/\mu_0}$, the result is the diffusely transmitted flux (see Eq. A25). Finally, the combined transmissivity of the two layers (1 over 2) to direct radiation from above at cosine zenith angle μ_0 ($T_{12}(\mu_0)$) is the direct beam that transmits layer 1 ($e^{-\tau_1^*/\mu_0}$) times the total transmissivity of layer 2 ($T_2(\mu_0)$) plus the downward diffuse flux at the interface (D^\downarrow) times the transmissivity of layer 2 to diffuse radiation (\bar{T}_2).

We can eliminate the upward diffuse flux D^\uparrow in the first equation of Eq. B1 using the second and third equations to first eliminate D^\downarrow , yielding the combined reflectivity $R_{12}(\mu_0)$.

Similarly, we can eliminate the down diffuse flux D^\downarrow in the fourth equation of Eq. B1 using the second and third equations to first eliminate D^\uparrow , yielding the combined transmissivity $T_{12}(\mu_0)$. The resulting equations for the combined reflectivity and transmissivity to direct radiation are:

$$\begin{aligned} R_{12}(\mu_0) &= R_1(\mu_0) + \frac{\{(T_1(\mu_0) - e^{-\tau_1^*/\mu_0})\bar{R}_2 + e^{-\tau_1^*/\mu_0}R_2(\mu_0)\}\bar{T}_1}{1 - \bar{R}_1\bar{R}_2} \\ T_{12}(\mu_0) &= e^{-\tau_1^*/\mu_0}T_2(\mu_0) + \frac{\{(T_1(\mu_0) - e^{-\tau_1^*/\mu_0}) + e^{-\tau_1^*/\mu_0}R_2(\mu_0)\bar{R}_1\}\bar{T}_2}{1 - \bar{R}_1\bar{R}_2} \end{aligned} \quad (B2)$$

We can interpret the denominator term $1 - \bar{R}_1\bar{R}_2$ as a series of multiple interlayer scatterings of successively higher orders using the binomial expansion: $(1 - x)^{-1} = 1 + x + x^2 + x^3 + x^4 \dots$ valid for $x < 1$. Thus, all orders of multiple scatterings between layers are accounted for.

Similarly, for the case of diffuse downward flux at the top of the two layers, normalized to 1 at the top of layer 1, the combined reflectivity and transmissivity are:

$$\begin{aligned} \bar{R}_{12} &= \bar{R}_1 + D^\uparrow \bar{T}_1 \\ D^\uparrow &= D^\downarrow \bar{R}_2 \\ D^\downarrow &= D^\uparrow \bar{R}_1 + \bar{T}_1 \\ \bar{T}_{12} &= D^\downarrow \bar{T}_2 \end{aligned} \quad (B3)$$

Note that in Eq. B3 the interface diffuse fluxes D^\uparrow and D^\downarrow are different than those in Eq. B1. In Eq. B1 these diffuse fluxes are due to multiple scattering from the direct beam source at the top, whereas here they are due to multiple scattering of a diffuse beam source at the top. These equations can also be understood term by term. The combined reflectivity of the two layers (1 over 2) to diffuse radiation from above (\bar{R}_{12}) is the diffuse reflectivity of layer 1 (\bar{R}_1) plus the upward diffuse flux at the interface between the two layers (D^\uparrow) times the diffuse transmissivity of layer 1 (\bar{T}_1). The upward diffuse flux at the interface between layers (D^\uparrow) is the downward diffuse flux at the interface (D^\downarrow) times the reflectivity of layer 2 to diffuse radiation (\bar{R}_2). The downward diffuse flux at the interface between layers (D^\downarrow) is the upward diffuse flux at the interface (D^\uparrow) times the reflectivity of layer 1 to diffuse radiation (\bar{R}_1) plus the diffuse radiation transmitted through layer 1 (\bar{T}_1). Finally, the combined transmissivity of the two layers (1 over 2) to diffuse radiation from above (\bar{T}_{12}) is the downward diffuse flux at the interface (D^\downarrow) times the transmissivity of layer 2 to diffuse radiation (\bar{T}_2).

We can eliminate the upward diffuse flux D^\uparrow in the first equation of Eq. B3 using the second and third equations to first eliminate D^\downarrow , yielding the combined reflectivity \bar{R}_{12} . Similarly, we can eliminate the down diffuse flux D^\downarrow in the fourth equation of Eq. B3 using the second and third equations to first eliminate D^\uparrow , yielding the combined transmissivity \bar{T}_{12} . The resulting equations for the combined reflectivity and transmissivity to diffuse

radiation from above are:

$$\begin{aligned}\bar{R}_{12} &= \bar{R}_1 + \frac{\bar{T}_1 \bar{R}_2 \bar{T}_1}{1 - \bar{R}_1 \bar{R}_2} \\ \bar{T}_{12} &= \frac{\bar{T}_1 \bar{T}_2}{1 - \bar{R}_1 \bar{R}_2}\end{aligned}\tag{B4}$$

We also need the combined reflectivity and transmissivity to diffuse radiation from below. We note that if the order 1 over 2 in Eqs. B4 is reversed to 2 over 1, then top becomes bottom, and we can immediately write the combined reflectivity and transmissivity to diffuse radiation from below:

$$\begin{aligned}\bar{R}_{21} &= \bar{R}_2 + \frac{\bar{T}_2 \bar{R}_1 \bar{T}_2}{1 - \bar{R}_2 \bar{R}_1} \\ \bar{T}_{21} &= \frac{\bar{T}_2 \bar{T}_1}{1 - \bar{R}_2 \bar{R}_1}\end{aligned}\tag{B5}$$

Note that for the combined transmissivities to diffuse radiation, $\bar{T}_{12} = \bar{T}_{21}$, but for the combined reflectivities to diffuse radiation, $\bar{R}_{12} \neq \bar{R}_{21}$ in general. Thus the combined AOPs depend on whether we consider radiation incident from above layer 1 or below layer 2. Such a combined two layer system is said to be “inhomogeneous” for AOPs as opposed to the individual layers which are said to be “homogeneous” for AOPs.

To combine several layers together, two passes are made through the layers: one starting from the top and proceeding down, the other starting at the bottom surface and proceeding up. In passing from the top down, we make the following approximation. If the total transmission to either direct radiation (e.g. $T_{12}(\mu_0)$ for a two layer system) or diffuse radiation (e.g. \bar{T}_{12} for a two layer system) is less than a small adjustable value (typically .001), AOPs for lower layers are not computed. In passing from the bottom up, we assume non-zero values of ocean reflectivities but zero transmissivities at the ocean/ice interface.

Once the entire column has been combined, we have at all interfaces between layers: $e^{-\tau^*/\mu_0}$, the direct beam transmission from the top, with τ^* the scaled optical depth from top to the interface, $R_{up}(\mu_0)$, the reflectivity to direct solar radiation of the entire column below, $T_{dn}(\mu_0)$, the total transmission (i.e. both direct and diffuse) to direct solar radiation incident at the top to the interface, \bar{R}_{up} , the reflectivity of the column below the interface to diffuse radiation from above, \bar{R}_{dn} , the reflectivity of the column above the interface to diffuse radiation from below, and \bar{T}_{dn} the transmissivity of the column above the interface to diffuse radiation from above.

Using the interface reflectivities and transmissivities, we can write down the normalized

upward and downward fluxes to both incident direct and diffuse radiation:

$$\begin{aligned}
Fdr_{dn} &= e^{-\tau^*/\mu_0} + \frac{(T_{dn}(\mu_0) - e^{-\tau^*/\mu_0}) + e^{-\tau^*/\mu_0} R_{up}(\mu_0) \bar{R}_{dn}}{1 - \bar{R}_{dn} \bar{R}_{up}} \\
Fdr_{up} &= \frac{e^{-\tau^*/\mu_0} R_{up}(\mu_0) + (T_{dn}(\mu_0) - e^{-\tau^*/\mu_0}) \bar{R}_{up}}{1 - \bar{R}_{dn} \bar{R}_{up}} \\
Fdf_{dn} &= \frac{\bar{T}_{dn}}{1 - \bar{R}_{dn} \bar{R}_{up}} \\
Fdf_{up} &= \frac{\bar{T}_{dn} \bar{R}_{up}}{1 - \bar{R}_{dn} \bar{R}_{up}}
\end{aligned} \tag{B6}$$

The various terms in the fluxes can be interpreted from ray-tracing arguments. Consider Fdr_{dn} first. The first term is the direct beam transmission. The next term is the diffusely transmitted radiation through the entire atmosphere above the interface. The last term is the directly transmitted radiation reflected by the entire system below the interface and in turn reflected back down by the entire atmosphere above the interface. The denominator accounts for all orders of multiple diffuse reflections at the interface. Next consider Fdr_{up} . The first term in the numerator is direct beam transmission that reflects off of the entire system below the interface; the second term is the diffusely transmitted radiation through the entire atmosphere above the interface (total transmission minus the direct beam transmission) that reflects off of the entire system below the interface. Again, the denominator accounts for all orders of multiple diffuse reflections at the interface. The diffuse fluxes Fdf_{dn} and Fdf_{up} should be self-evident at this point.

We note a couple of interesting features of these flux expressions. If the optical depth above the interface for the direct solar beam is very large, i.e. if $\tau^* \gg 1$, then $e^{-\tau^*/\mu_0} \ll 1$ and the two fluxes for the direct beam become identical to their respective diffuse fluxes. If there is no zenith angle dependence of the reflectivity, i.e. if $R_{up}(\mu_0) = \bar{R}_{up}$, then the direct fluxes also reduce to the diffuse fluxes. Finally, by separating the direct and diffuse contributions to the downward flux, and multiplying the appropriate terms by the appropriate reflectivity, one can derive Fdr_{up} from Fdr_{dn} .

Eqs. B1 through B6 are valid only for layers with the same index of refraction, in other words, above and below the refractive boundary (section 4.1). To include the refractive boundary, we use Eqs. 21 and 25 to define the reflectivities and transmissivities of the refractive boundary to direct and diffuse radiation, respectively. Consider the refractive boundary as a pseudo-layer at the top of a layer of index of refraction n , such as that for the DL (see Table 1 and Fig. 1). We combine the refractive boundary to the rest of the DL using Eqs. B2, being careful to distinguish upward and downward diffuse reflectivities and transmissivities in the refractive boundary (e.g. Eq. 25), where we substitute “f” for 1 (referring to the Fresnel layer, i.e. the refractive boundary), yielding the combined

formulas:

$$\begin{aligned} R_{f2}(\mu_0) &= R_f(\mu_0) + \frac{T_f(\mu_0)R_2(\mu_{0n})\overline{T}_{fb}}{1 - \overline{R}_{fb}\overline{R}_2} \\ T_{f2}(\mu_0) &= T_f(\mu_0)T_2(\mu_{0n}) + \frac{\{T_f(\mu_0)R_2(\mu_{0n})\overline{R}_{fb}\}\overline{T}_2}{1 - \overline{R}_{fb}\overline{R}_2} \end{aligned} \quad (B7)$$

Note very carefully that the direct beam cosine zenith angle μ_0 is distinguished above the refractive boundary (i.e. in the R_f and T_f terms) from below the refractive boundary where the angle is μ_{0n} (e.g. Eq. 20 and the terms $R_2(\mu_{0n})$ and $T_2(\mu_{0n})$). Note also that there is no “scattering” of radiation passing through the refractive boundary, so there is no term $T_1(\mu_0) - e^{-\tau_1^*/\mu_0}$ as in Eqs. B2; here this term is zero.

We can generalize the combination formulas in Eqs. B2 and those for the fluxes in Eqs. B6 by redefining the direct beam radiation as:

$$Tdr_s(\mu_0, \tau_a + \tau_b) = e^{-\tau_a^*/\mu_0} T_f(\mu_0) e^{-\tau_b^*/\mu_{0n}} \quad (B8)$$

where subscript s refers to the direct solar beam, τ_a^* is the scaled optical depth from the top interface down to the refractive boundary, τ_b^* is the scaled optical depth from the refractive boundary to the interface below the refractive boundary. This equation clearly shows how the direct beam is refracted and continues into the lower medium at the refracted angle, and how the refractive boundary reduces the direct beam passing through it.

We apply Eqs. B4 for the combined reflectivity and transmissivity to diffuse radiation from above, yielding the equations:

$$\begin{aligned} \overline{R}_{f2} &= \overline{R}_{fa} + \frac{\overline{T}_{fa}\overline{R}_2\overline{T}_{fb}}{1 - \overline{R}_{fb}\overline{R}_2} \\ \overline{T}_{f2} &= \frac{\overline{T}_{fa}\overline{T}_2}{1 - \overline{R}_{fb}\overline{R}_2} \end{aligned} \quad (B9)$$

We again need the combined reflectivity and transmissivity to diffuse radiation from below. We note that if the order f over 2 in Eqs. B4 is reversed to 2 over f, then top becomes bottom, and we can immediately write the combined reflectivity and transmissivity to diffuse radiation from below:

$$\begin{aligned} \overline{R}_{2f} &= \overline{R}_2 + \frac{\overline{T}_2\overline{R}_{fb}\overline{T}_2}{1 - \overline{R}_2\overline{R}_{fb}} \\ \overline{T}_{2f} &= \frac{\overline{T}_2\overline{T}_{fb}}{1 - \overline{R}_2\overline{R}_{fb}} \end{aligned} \quad (B10)$$

Note that in contrast to Eqs. B4 and B5, the combined transmissivities \overline{T}_{f2} and \overline{T}_{2f} are not equal in general.

Appendix C: Atmosphere Radiation Model

We use the solar radiation model of CCM3 (Kiehl et al. 1996; based on Briegleb 1992). This radiation model is the basis for that in CCSM3 (Collins et al. 2004). The latter includes detailed aerosols and a sophisticated cloud overlap scheme, but the basic physics is the same. Thus, for the purposes of providing surface spectral band direct and diffuse fluxes required by the Delta-Eddington solar radiation treatment for both clear and overcast skies, in the same wave bands and using the same radiative transfer technique as in CCSM3, the CCM3 column (i.e. one dimensional) radiation model is adequate. We give a brief overview of this model.

The solar radiation spectrum is divided into 18 discrete spectral intervals, for each of which the solar irradiance fraction is specified: 7 intervals for O_3 for wavelengths $0.20 - 0.35\mu m$, 1 interval for the visible wavelengths $0.35 - 0.70\mu m$, 7 intervals for the H_2O bands $0.70 - 5.00\mu m$, and 3 intervals for the CO_2 $2.7\mu m$ and $4.3\mu m$ bands. Absorption by O_2 is also included in the visible and near-infrared. A background boundary layer aerosol is included for the lowest three atmospheric layers with visible optical depth 0.12. Cloud scattering depends on phase (liquid or ice), spectral band, particle effective radius and cloud water path. Cloud particles are assumed to be liquid droplets for temperatures greater than $-10^\circ C$.

The atmospheric column is divided into 18 horizontally and vertically homogeneous layers, each of which is a well-mixed combination of several radiatively active constituents. The Delta-Eddington solution for each of these layers is evaluated and then combined together, subject to specified cosine solar zenith angle and surface spectral direct/diffuse reflectivities. Thus, the method is very similar to the one used in this report.

For solar radiation top-of-atmosphere flux we specify 20 May at 80° north latitude for overcast conditions. For clear sky we use a latitude of 67° and summer solstice conditions to increase solar zenith angle range (e.g. Fig. 18). For this clear sky Arctic circle case, cosine solar zenith angle varies from 0.01 (about 0.5° solar elevation) to 0.72 (about 47° solar elevation, appropriate for local noon near solstice at the Arctic circle).

The profile is modified from an original sub-arctic profile (McClatchey et al. 1972). Layers have the specified mid-layer pressure (P) and temperature T, and are bounded by interfaces with mean adjacent-layer pressures. CO_2 is uniformly mixed at 370×10^{-6} volume mixing ratio. Cloud cover (CC) is removed for clear sky conditions with no changes to the rest of the profile. Cloud particles are assumed to be liquid droplets with $7\mu m$ effective radius, in keeping with Jin et al. (1994); CCM3 radiation assumes liquid droplets for $T > -10^\circ C$. CP is cloud path (liquid water), the mass path for cloud droplets in the specified atmospheric layer. The cloud level (~ 930 hPa), is taken from Jin et al. (1994). “srf” refers to the surface air level at nominally 2 m, and “grnd” to the physical snow/ice/pond surface. The profile is shown in Table C.

Table C. Polar Atmosphere Profile. Mid-layer pressure P, temperature T, water vapor specific humidity H_2O , ozone mass mixing ratio O_3 , cloud cover (fraction) CC, cloud liquid water path CP. “srf” is 2 m above surface, and “grnd” is the physical surface.

layer	P(hPa)	T(K)	$H_2O(g/g)$	$O_3(g/g)$	CC	CP(g/m^2)
18	2	273	4.0×10^{-6}	7.0×10^{-6}	0	0
17	5	251	4.0×10^{-6}	1.3×10^{-5}	0	0
16	15	234	4.0×10^{-6}	1.0×10^{-5}	0	0
15	35	226	4.0×10^{-6}	5.5×10^{-6}	0	0
14	60	225	4.0×10^{-6}	4.2×10^{-6}	0	0
13	105	225	4.0×10^{-6}	2.2×10^{-6}	0	0
12	160	225	6.4×10^{-6}	1.0×10^{-6}	0	0
11	235	225	2.6×10^{-5}	5.0×10^{-7}	0	0
10	320	234	1.2×10^{-4}	2.0×10^{-7}	0	0
9	420	247	5.2×10^{-4}	1.4×10^{-7}	0	0
8	520	257	1.1×10^{-3}	1.0×10^{-7}	0	0
7	610	265	2.0×10^{-3}	8.0×10^{-8}	0	0
6	710	272	3.1×10^{-3}	7.0×10^{-8}	0	0
5	800	277	4.2×10^{-3}	6.0×10^{-8}	0	0
4	870	280	5.1×10^{-3}	5.5×10^{-8}	0	0
3	930	281	5.9×10^{-3}	5.0×10^{-8}	--1--	60
2	970	278	4.0×10^{-3}	4.5×10^{-8}	0	0
1	1000	276	3.0×10^{-3}	4.0×10^{-8}	0	0
srf	1008	273	3.0×10^{-3}	4.0×10^{-8}	0	0
grnd	1010	273	---	---	---	---

Appendix D: Variable Number of Snow and Sea Ice Layers

The number of snow and sea ice layers in this work, namely one for snow and four for sea ice, was determined by the present version of CCSM sea ice. For many applications however, a different number of snow and sea ice layers may be desired. In this appendix, we discuss briefly how the Delta-Eddington solar radiation treatment generalizes to variable number of snow and sea ice layers. The case for multiple pond layers over sea ice would be similar to that for multiple snow layers.

Variable Number of Snow Layers

An extension to multiple snow layers is straightforward using the band data in Tables 4 to 7. Given the grain radius and snow density, snow extinction coefficients for each snow layer can be evaluated from Eq. 68, and any dust or carbon soot (or other) impurities included through Eqs. 69 and 70. With the addition of snow layer thickness, individual snow layer reflectivities and transmissivities can be computed as in Eqs. 50 and combined with one another and with the underlying sea ice layers using the multiple scattering formalism in section 4.4 .

One remaining issue is how to represent surface absorption when two or more snow layers overlie sea ice (see section 4.5). For one snow layer in the present version of CCSM sea ice, all solar absorption above the sea ice refractive boundary should be included in the surface absorption if snow has zero heat capacity (see section 3 and Table 1). This approach yields a smooth transition between snow/ice and ice surface absorption as snow thickness tends to zero. In this case the optical thinning of the snow allows most solar radiation to penetrate the snow layer and be absorbed in the sea ice surface scattering layer, which is physically realistic. Surface absorbed solar radiation would first be used to melt the thin snow layer in the present sea ice thermodynamics, even though such absorption includes that of the sea ice SSL, but the close thermal contact of a thin snow layer and the sea ice SSL makes this approximation acceptable. When the snow layer is thick, most of the solar absorption occurs in the snow layer because of its large optical thickness, so the approximation of including all solar absorption above the refractive boundary as thermodynamic surface absorption remains valid. We note again that this approach assumes snow and pond have zero heat capacity, i.e. they have no internal absorption, and is the case for the present CCSM sea ice model (see Briegleb et al. 2004).

However, if snow has finite heat capacity for one or more layers, how is surface absorption to be represented, as opposed to internal snow layer absorption? How is this surface absorption to depend on the thickness of the snow layers? A reasonable solution is to include a “snow SSL” analogous to that for bare sea ice, and thus sub-divide the top snow layer for the radiative transfer calculation. This is the approach we took in the Delta-Eddington solar radiation treatment presented in this work. Similarly to sea ice (see

top of p.10) we note that for the snow thermal conductivity, density and heat capacity identical to sea ice (Briegleb et al. 2004), the thermal penetration depth for one hour flux exchange is .04 m, consistent with near surface absorption of solar radiation. For example, one can choose a fixed snow surface scattering layer thickness of .04 m say, and include all absorption in this layer for the surface as we have done here. When the top snow layer thickness becomes less than .08 m, one can set this snow SSL thickness equal to half the top snow layer thickness. As the total snow layer thickness thins during melting, the surface and internal absorption will become very small. When snow vanishes, surface absorption can then become that for the bare sea ice case, namely the solar radiation absorbed in the sea ice SSL.

Variable Number of Sea Ice Layers

For the bare sea ice case, we continue to sub-divide the top layer into a surface scattering layer (SSL) and a drained layer (DL), i.e. layers $h_{1/4}$ and $h_{3/4}$ of Table 1, respectively. To approximately conserve the broadband albedos and transmittances, the DL extinction coefficient is multiplied by the number of evenly-spaced sea ice layers over the standard number of four. This empirical approximation partially accounts for the variation in DL optical path with variable number of sea ice layers. We treat the SSL in the same manner as previously: SSL thickness .05 m unless total sea ice thickness h_i is less than 1.5 m, otherwise $h_i/30$. When the top sea ice layer becomes less than twice the SSL thickness, we set the SSL thickness to half the top layer thickness (see Table 1).

Table D shows albedos and spectral transmittances to the underlying ocean for a wide range of sea ice layer numbers for thin (0.1 m), moderate (1.0 m) and thick (5.0 m) sea ice. We include results for one ponded sea ice case.

The variations in sea ice albedos and spectral transmittances with varying number of sea ice layers arise from approximations in the Delta-Eddington solar radiation treatment discussed in section 4. Nevertheless, the variations for broad band albedo are within the uncertainty of measurements reported in section 5.3 . Uncertainties in the transmittances are not known very well, but the variations shown in Table D become large for layer numbers much less than or much greater than the standard four layer case, especially for thinner bare sea ice and ponded ice. Any user of the Delta-Eddington solar radiation treatment who uses a different number of sea ice layers than the standard four needs to be aware of these changes in important AOPs.

Table D. Broadband albedos and spectral transmittances for Delta-Eddington solar radiation treatment, for various number of sea ice layers. “Alb” is albedo, “Tr” transmittance through the sea ice to the ocean, “bb” broadband, “vs” visible and “ni” near-infrared. Atmosphere radiation model and profile (Appendix C) has an overcast low stratus cloud. The solar zenith angle is 60° . Albedos and transmittances are for diffuse incident radiation on the sea ice, with h_i the sea ice thickness and h_p the pond depth.

Ice Layer Number	Alb(bb) $0.2 - 5.0\mu m$	Tr(vs) $0.2 - 0.7\mu m$	Tr(ni) $0.7 - 5.0\mu m$
Bare Sea Ice $h_i = 0.1$ m			
1	.229	.741	.414
2	.241	.708	.213
4	.246	.692	.146
16	.242	.692	.113
64	.243	.687	.099
Bare Sea Ice $h_i = 1.0$ m			
1	.584	.265	0
2	.592	.190	0
4	.595	.156	0
16	.591	.142	0
64	.593	.125	0
Bare Sea Ice $h_i = 5.0$ m			
1	.657	.034	0
2	.657	.004	0
4	.657	.002	0
16	.657	0	0
64	.655	0	0
Ponded Sea Ice $h_i = 1.0$ m, $h_p = 0.2$ m			
1	.195	.288	0
2	.198	.289	0
4	.204	.280	0
16	.218	.242	0
64	.226	.212	0

Appendix E: Glossary of Acronyms

Term	Description
AOP	Apparent Optical Property (e.g. albedo, absorbed and transmitted flux)
Chl a	Chlorophyll a
CC	Cloud Cover (i.e. fraction of horizontal coverage)
CCM3	Community Climate Model Version 3
CCSM	Community Climate System Model
CCSM3	Community Climate System Model Version 3
CP	Cloud Path (i.e. cloud liquid water, or mass path)
DE	Delta-Eddington solar radiation
DL	Drained layer between the surface scattering layer and ice interior
DOM	Discrete Ordinate radiation Model
INT	Interior sea ice below the drained layer
IOP	Inherent Optical Property (e.g. extinction coefficient, single scattering albedo and asymmetry parameter)
MC	Monte Carlo radiation model
SGER	Small Grant for Experimental Research
SHEBA	Surface Heat Budget of the Arctic field experiment 1997-1998
SNICAR	SNow Ice and Aerosol Radiative model
SSL	Surface scattering layer
SW	Shortwave (0.2 to $5.0\mu m$ wavelength solar radiation)
x1	CCSM high horizontal resolution ocean/sea ice grid
x3	CCSM low horizontal resolution ocean/sea ice grid

References

- Allison, I., R. E. Brandt and S. G. Warren, 1993: East Antarctic sea ice: albedo, thickness distribution, and snow cover. *J. Geophys. Res.*, **98**, 12417–12429.
- Brandt, R. E., S. G. Warren, A. P. Worby and T. C. Grenfell, 2005: Surface Albedo of the Antarctic Sea Ice Zone. *J. Climate*, **18**, 3606–3622.
- Briegleb, B. P., 1992: Delta-Eddington Approximation for Solar Radiation in the NCAR Community Climate Model. *J. Geophys. Res.*, **97**, 7603–7612.
- Briegleb, B. P., C. M. Bitz, E. C. Hunke, W. H. Lipscomb, M. M. Holland, J. L. Schramm, and R. E. Moritz, 2004: Scientific Description of the Sea Ice Component in the Community Climate System Model, Version 3. NCAR/TN-463+STR, 70pp.
- Coakley, J. A., R. D. Cess, F. B. Yurevich, 1983: The effect of tropospheric aerosols on the Earth's radiation budget: A parameterization for climate models. *J. Atmos. Sci.*, **40**, 116–138.
- Collins, W. D., P. J. Rasch, B. A. Boville, J. R. McCaa, D. L. Williamson, J. T. Kiehl, B. P. Briegleb, C. M. Bitz, Shian-Jiann Lin, Minghua Zhang, Youngjiu Dai, 2004: Description of the NCAR Community Atmosphere Model (CAM 3.0). NCAR/TN-464+STR, 214pp.
- Collins, W. D., C. M. Bitz, M. L. Blackmon, G. B. Bonan, C. S. Bretherton, J. A. Carton, P. Chang, S. C. Doney, J. J. Hack, T. B. Henderson, J. T. Kiehl, W. G. Large, D. S. McKenna, B. D. Santer, and R. D. Smith, 2006: The Community Climate System Model: CCSM3. *J. Climate*, **19**, 2122–2143.
- Cox, G. F. N., and W. F. Weeks, 1983: Equations for determining the gas and brine volumes in sea-ice samples. *J. Glaciol.*, **29**, 306–316.
- Curry, J. A., J. L. Schramm, E. E. Ebert, 1995: Sea ice-albedo feedback mechanism. *J. Climate*, **8**, 240–247.
- Curry, J. A., J. L. Schramm, D. K. Perovich, and J. O. Pinto, 2001: Applications of SHEBA/FIRE data to evaluation of snow/ice albedo parameterizations. *J. Geophys. Research.*, **106**, D14, 15345–15355.
- Ebert, E. E. and J. A. Curry, 1993: An intermediate one-dimensional sea ice model for investigating ice-atmosphere interactions. *J. Geophys. Research.*, **98**, 10085–10109.
- Flanner, M. G. and C. S. Zender, 2006: Linking snowpack microphysics and albedo evolution, *J. Geophys. Research.*, **111**, D12208, doi:10.1029/2005JD006834.
- Flanner, M. G., C. S. Zender, J. T. Randerson, and P. J. Rasch, 2006: Present Day Climate Forcing and Response from Black Carbon in Snow, *J. Geophys. Research.*, in press
- Grenfell, T. C., G. A. Maykut, 1977: The optical properties of ice and snow in the Arctic Basin. *J. Glaciology*, **18**, 445–463.

- Grenfell, T. C. and D. K. Perovich, 1981: Radiation absorption coefficients of polycrystalline ice from 400-1400 nm. *J. Geophys. Research.*, **86**, 7447–7450.
- Grenfell, T. C., 1991: A radiative transfer model for sea ice with vertical structure variations. *J. Geophys. Research.*, **96**, 16991–17001.
- Grenfell, T. C. and S. G. Warren, 1999: Representation of a nonspherical ice particle by a collection of independent spheres for scattering and absorption of radiation. *J. Geophys. Research.*, **104**, D24, 31697–31709.
- Grenfell, T. C., B. Light and M. Sturm, 2002: Spatial distribution and radiative effects of soot in the snow and sea ice during the SHEBA experiment. *J. Geophys. Res.*, **107**, NO. C10, 8032, 10.1029/2000JC000414.
- Heney, L. G., and J. L. Greenstein, 1941: Diffuse radiation in the galaxy, *Astrophys. J.*, **93**, 70–83.
- Holland, M., and C. M. Bitz, 2003: Polar amplification of climate change in coupled models. *Climate Dynamics*, **21**, 221–232.
- Irvine, W. M., and J. B. Pollack, 1968: Infrared optical properties of water and ice spheres. *Icarus*, **8**, 324–360.
- Jin, Z., K. Stamnes, W. F. Weeks, and Si-Chee Tsay, 1994: The effect of sea ice on the solar energy budget in the atmosphere-sea ice-ocean system: A model study. *J. Geophys. Res.*, **99**, 25281–25294.
- Joseph, J. H., W. J. Wiscombe, and J. A. Weinman, 1976. The delta-Eddington approximation for radiative flux transfer, *J. Atmos. Sci.*, **33**, 2452–2459.
- Kiehl, J. T., J. J. Hack, G. B. Bonan, B. A. Boville, B. P. Briegleb, D. L. Williamson, P. J. Rasch, 1996: Description of the NCAR Community Climate Model (CCM3). NCAR/TN-420+STR, 152pp.
- Light, B., G. A. Maykut, and T. C. Grenfell, 2003a: Effects of temperature on the microstructure of first-year Arctic sea ice. *J. Geophys. Res.*, p**108(C2)**, 3051, doi:10.1029/2001JC000887.
- Light, B., G. A. Maykut, and T. C. Grenfell, 2003b: A two-dimensional Monte Carlo model of radiative transfer in sea ice. *J. Geophys. Res.*, **108(C7)**, 3219, doi:10.1029/2002JC001513.
- Light, B., G. A. Maykut, and T. C. Grenfell, 2004: A temperature-dependent, structural-optical model of first-year sea ice. *J. Geophys. Res.*, **109**, **C06013**, doi:10.1029/2003JC002164.
- Light, B., T. C. Grenfell, and D. K. Perovich: Transmission and absorption of solar radiation by arctic sea ice during the melt season, submitted to *J. Geophys. Res.*

- Liou, Kuo-Nan, 1980: An Introduction to Atmospheric Radiation. *Academic Press, Inc. (London) Ltd.* 392 pp.
- Maykut, G. A. and D. Perovich, 1987: The role of shortwave radiation in the summer decay of sea ice cover. *J. Geophys. Research.*, **92**, 7032–7044.
- Maykut, G. A. and B. Light, 1995: Refractive-index measurements in freezing sea-ice and sodium chloride brines. *App. Opt.*, **34**, 950–961.
- McCormick, N. J., and G. E. Rinaldi, 1989: Seawater optical property estimation from in situ irradiance measurements. *App. Opt.*, **28**, 2605–2613.
- McClatchey, R. A., R. W. Fenn, J. E. A. Selby, F. E. Volz, and J. S. Garing, 1972. Optical Properties of the Atmosphere, Report AFCRL-72-0497, Air Force Cambridge Res. Lab., Bedford Mass.
- Paltridge, G. W. and C. M. R. Platt, 1976: Radiative processes in meteorology and climatology. *Elsevier Scientific Publishing Company*, Amsterdam, Oxford, New York.
- Paulson, C. A. and J. J. Simpson, 1977: Irradiance measurements in the upper ocean. *J. Phys. Oceanogr.*, **7**, 952–956.
- Perovich, D. K., T. C. Grenfell, B. Light and P. V. Hobbs, 2002: Seasonal evolution of the albedo of multiyear Arctic sea ice. *J. Geophys. Research.*, **107**, 8044.
- Shettle, E. P. and J. A. Weinman, 1970. The transfer of solar irradiance through inhomogeneous turbid atmospheres evaluated by Eddington’s approximation. *J. Atmos. Sci.*, **27**, 1048–1055.
- Soo Hoo, J. B., A. C. Palmisano, S. T. Kottmeier, M. P. Lizotte, S. L. Soo Hoo, and C. W. Sullivan, 1987: Spectral light absorption and quantum yield of photosynthesis in sea ice microalgae and a bloom of *Phaeocystis Pouchetti* from McMurdo Sound, Antarctica. *Mar. Ecol. Prog. Ser.*, **39**, 175–189.
- Warren, S. G. and W. J. Wiscombe, 1980: A model for the spectral albedos of snow, 2, snow containing atmospheric aerosols. *J. Atmos. Sci.*, **37**, 2734–2745.
- Warren, S. G., 1984: Optical constants of ice from the ultraviolet to the microwave. *Appl. Opt.*, **23**, 1206–1225.
- Warren, S. G. and A. D. Clarke, 1990: Soot in the Atmosphere and Snow Surface of Antarctica. *J. Geophys. Research.*, **95**, 1811–1816.
- Weatherly, J. W., B. P. Briegleb, W. G. Large and J. A. Maslanik, 1998: Sea Ice and Polar Climate in the NCAR CSM. *J. Climate*, **11**, 1472–1486.
- Wiscombe, W. J. and S. G. Warren, 1980: A model for the spectral albedos of snow, 1, pure snow. *J. Atmos. Sci.*, **37**, 2712–2733.

Figure 1. Sea ice layer structure, showing the surface scattering layer in relation to the drained layer and lower interior layers, for three sea ice thicknesses. h_i is the total sea ice thickness, with $h_i/4$ the thickness for the lowest three interior layers. The surface scattering layer thickness $h_{1/4}$ is $h_i/30$ for sea ice thinner than 1.50 m, and .05 m for thicker sea ice. The drained layer just below the surface scattering layer has thickness $h_{3/4} = h_i/4 - h_{1/4}$. Figure shown to scale, including sea ice freeboard.

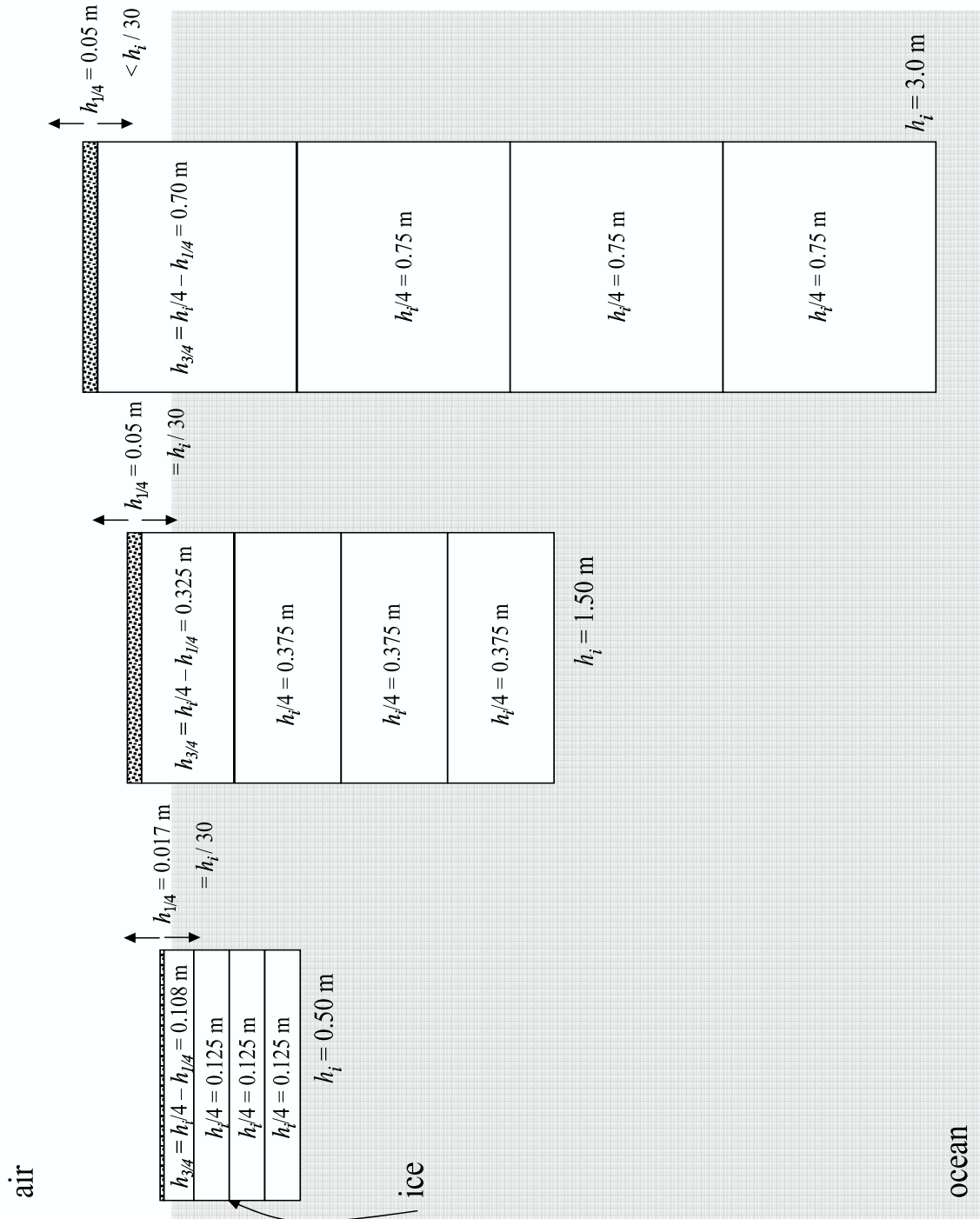


Figure 2. Types of snow/sea ice surfaces used in the Delta-Eddington solar radiation treatment. The first type is that for snow of depth h_s that completely covers the underlying sea ice (lower part of the figure). The second is that for ponded sea ice with no snow cover $h_s = 0$, where the fractional coverage of bare sea ice is $1 - f_p$ and that of ponds $f_p > 0$ (upper part of figure). Ponded sea ice is covered with ponds of depth $h_p > 0$, and the sea ice under the pond does not have an optically thick surface scattering layer. The surface scattering layer thickness is $h_{1/4}$, the drained layer thickness just below the surface scattering layer is $h_{3/4} = h_i/4 - h_{1/4}$, where h_i is the total sea ice thickness, and the lowest three interior layers have thickness $h_i/4$. Snow and the surface scattering layer (where present) are hatched. Sea ice under pond is colored light gray, while pond is colored dark gray.

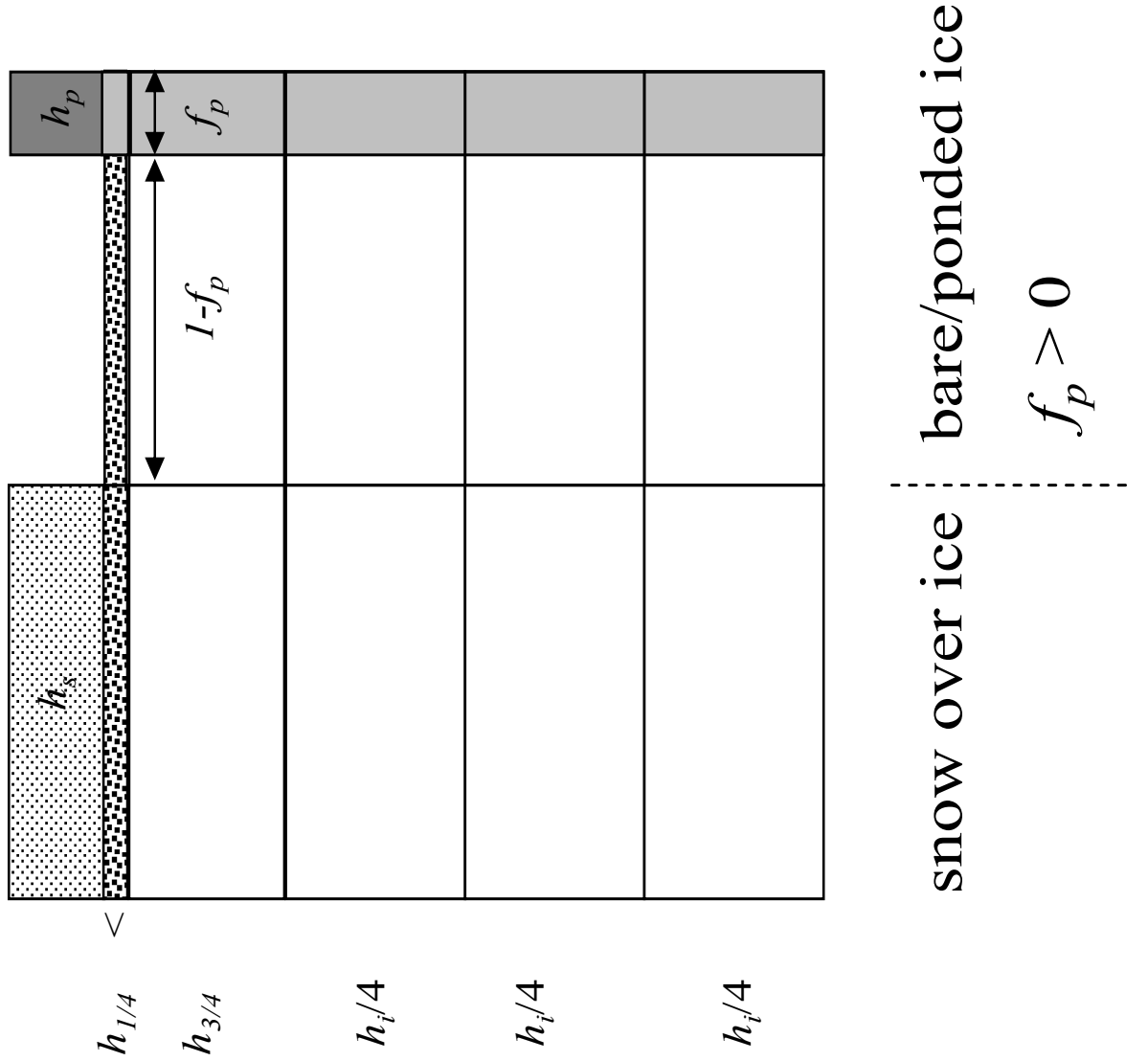


Figure 3. The refractive boundary location between the $h_{1/4}$ granular surface scattering layer and the $h_{3/4}$ solid drained layer. A portion of the direct radiation at cosine zenith angle μ incident on the top of the sea ice transmits the $h_{1/4}$ surface scattering layer, is refracted by the refractive boundary into cosine zenith angle μ_n , and continues into the $h_{3/4}$ solid drained layer. The reflectivity and transmissivity to direct radiation at the refractive boundary are $R_f(\mu)$ and $T_f(\mu)$ respectively. The reflectivity and transmissivity to diffuse radiation from above the refractive boundary layer are \bar{R}_{fa} and \bar{T}_{fa} respectively, and from below the refractive layer \bar{R}_{fb} and \bar{T}_{fb} respectively.

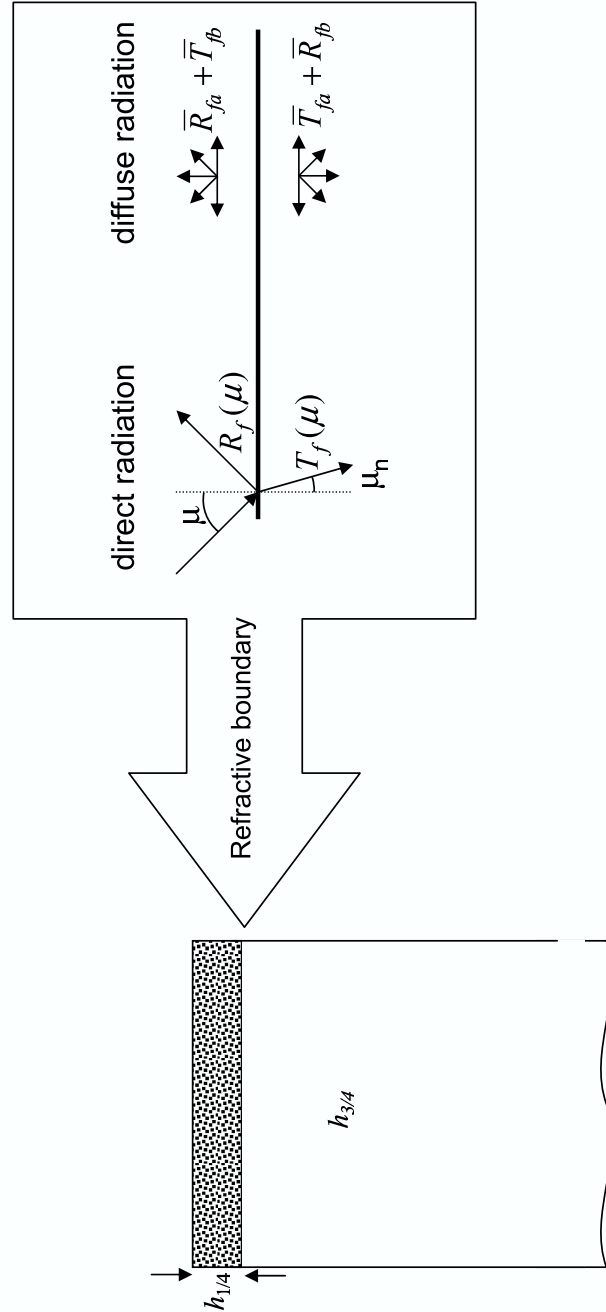


Figure 4. Snow albedo vs grain radius. Based on Mie calculations for equivalent ice spheres, from Wiscombe and Warren (1980), and Warren (personal communication). Albedos computed with the Delta-Eddington method for an optically thick homogeneous snow layer at $1nm$ spectral resolution and solar irradiance weighted over the various bands, for an incident beam with $\mu_0 = 0.5$.

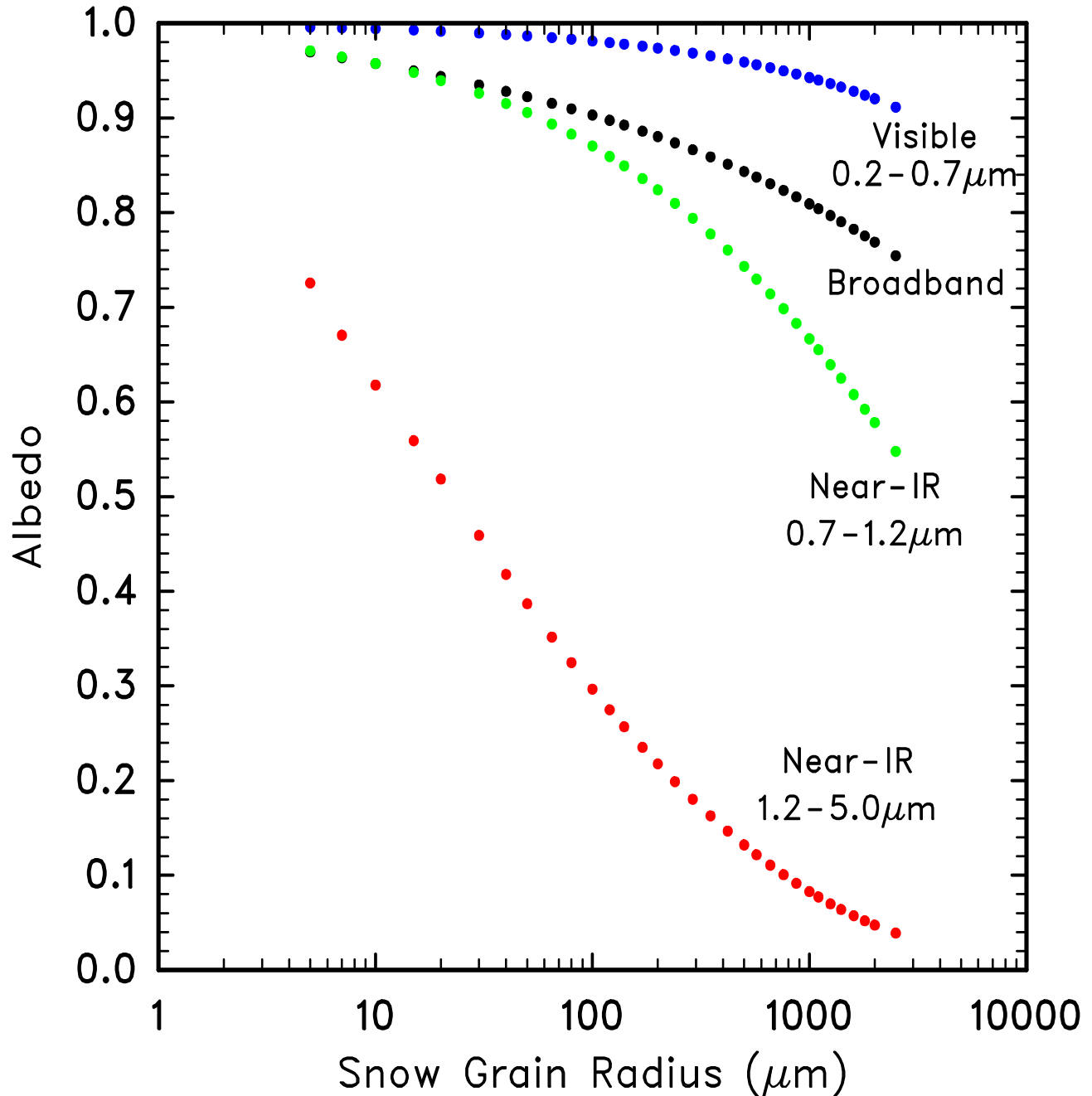


Figure 5. Broadband snow albedo vs snow thickness from the Delta-Eddington solar radiation parameterization, for various snow grain radii r_s . Overcast and clear sky conditions with cosine solar zenith angle $\mu_0 = 0.5$. Snow overlies sea ice of thickness 1.5 m. As snow thins regardless of snow grain radius, the underlying sea ice (overcast broad band albedo 0.647) is uncovered. One clear sky case is shown for 2500 μm grain size. The clear sky broadband albedo is lower for this case because of greater proportion of near-ir irradiance compared to visible than in the overcast case. For this case of 2500 μm grain size and clear sky, a few centimeters of snow actually absorbs more than the underlying sea ice.

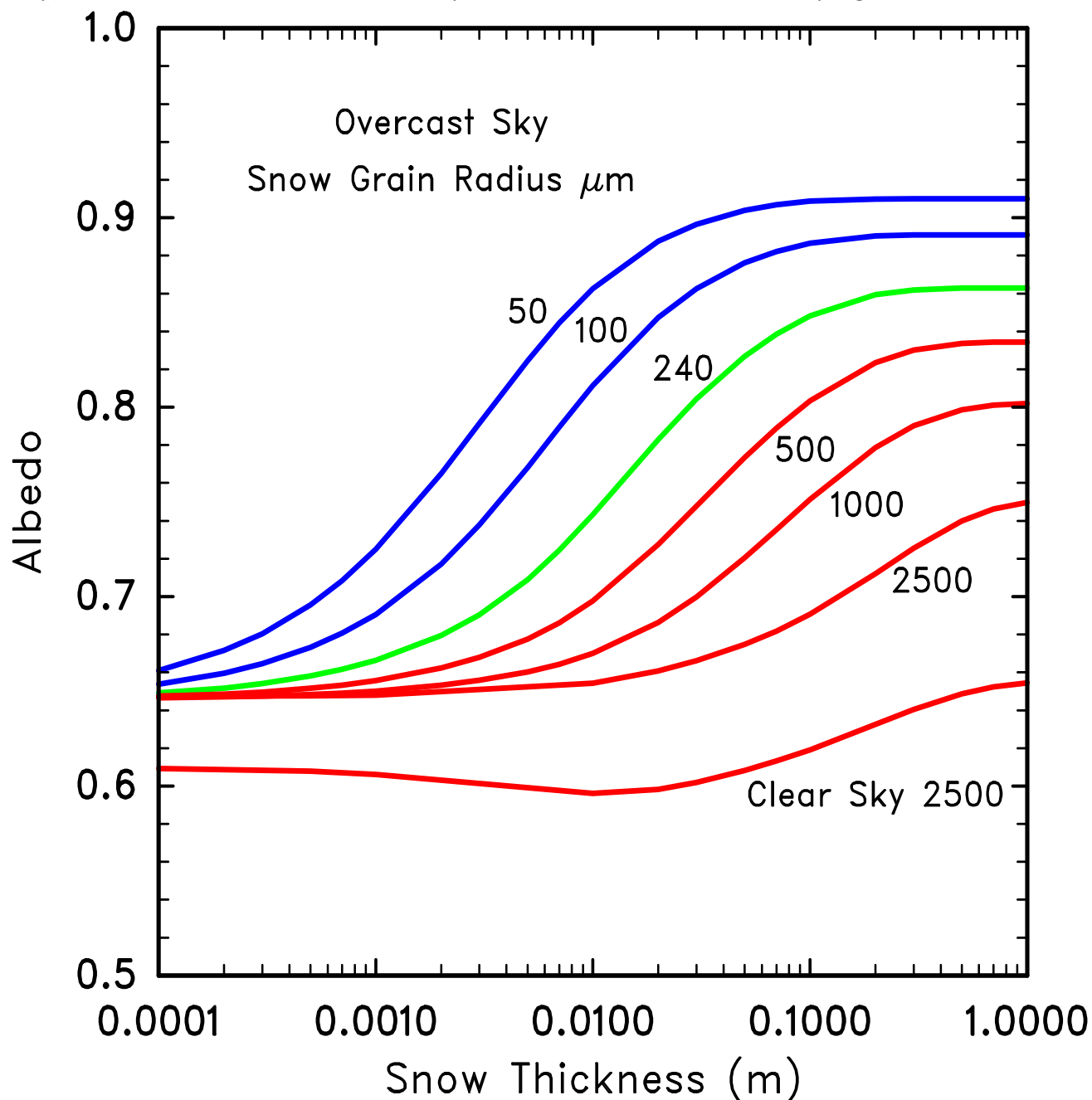


Figure 6. Averaged spectral albedos and related standard deviations for bare and ponded ice obtained along the albedo line during the SHEBA observations of the summer of 1998. The ponded ice spectral albedos are for 100% pond coverage.

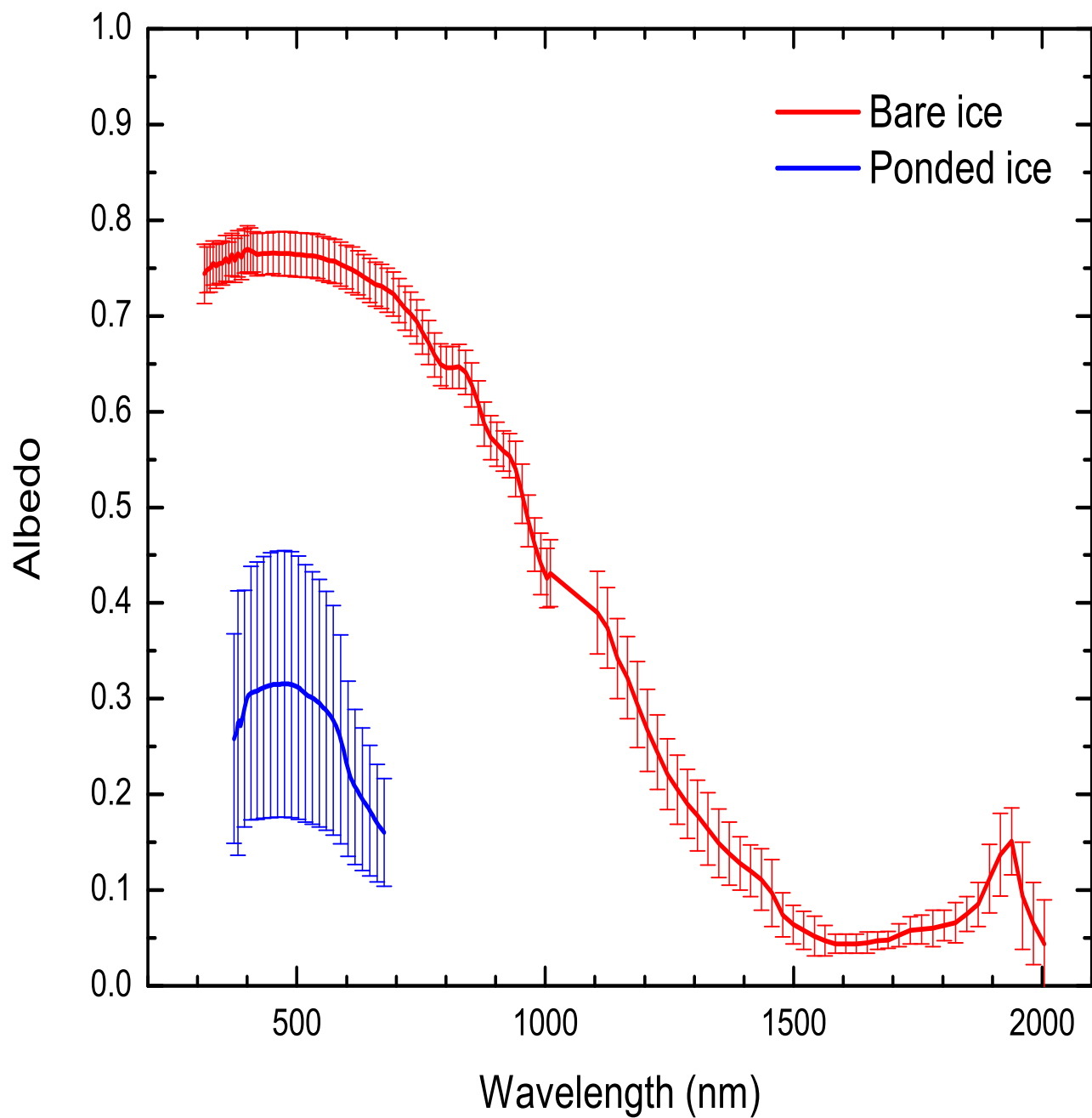


Figure 7. Average spectral albedos for bare and ponded ice. Ponded ice albedos are for 100% pond coverage. Observed bare ice and ponded ice spectral albedos and related standard deviations were obtained along the albedo line during the SHEBA observations of the summer of 1998. For the model calculations, bare sea ice is 2.0 m thick, while pond-over-ice is 0.35 m deep and ice-under-pond is 1.5 m thick. The Delta-Eddington solar parameterization uses IOPs from Tables 12 and 15, and includes algal absorption in the lowest layer of sea ice for both bare sea ice and ponded ice. CCSM3 parameterization spectral albedos are shown for bare sea ice.

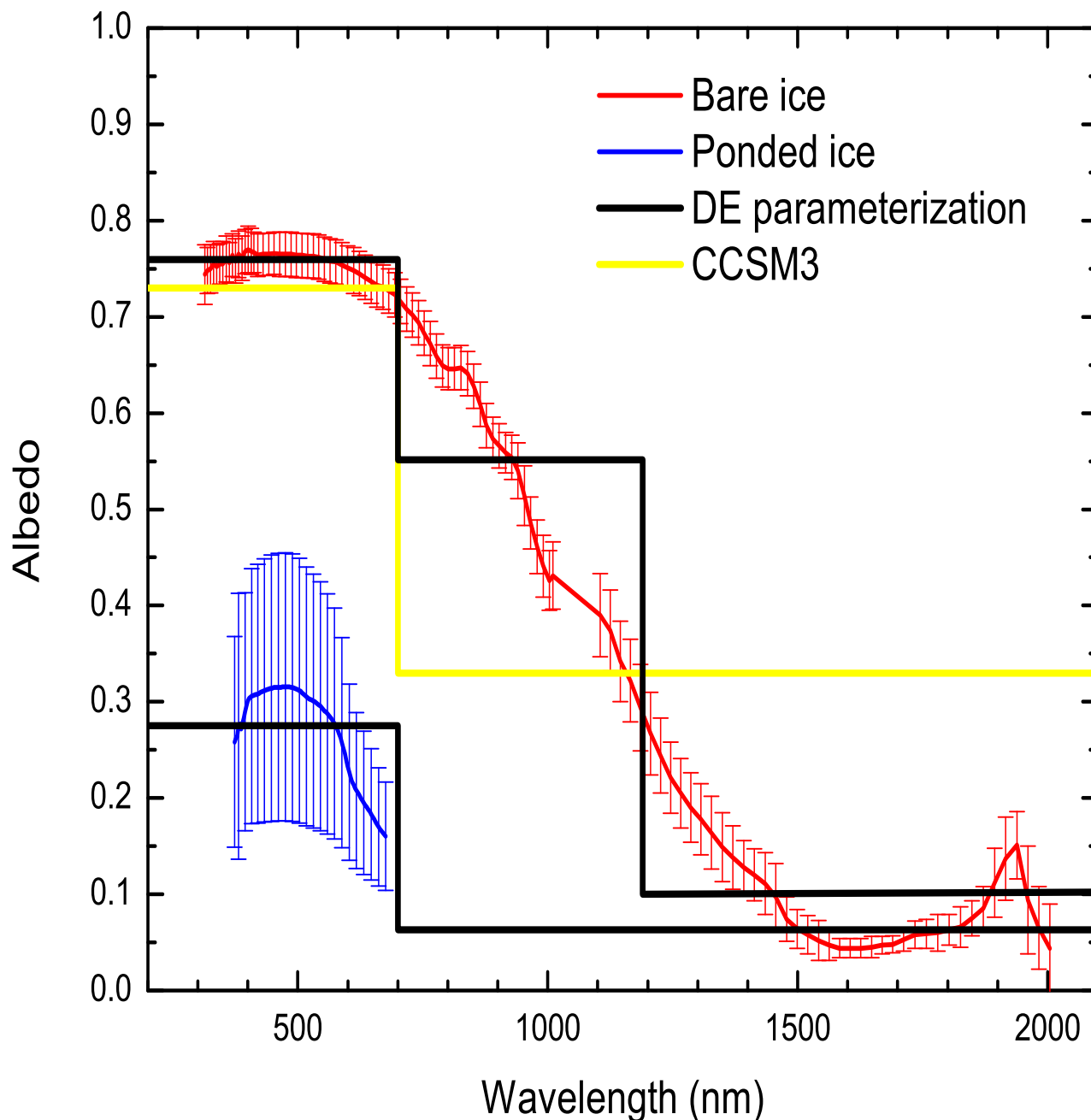


Figure 8. Spectral transmittance for a variety of bare ice locations measured during the SHEBA summer, where FY=first year ice, MY=multi-year ice. For observed spectra, dates, ice types and thicknesses are as follows: 15 Aug (FY ice, 100 cm), 6 August (MY ice, 155 cm), 27 July (MY ice, 168 cm); 7 June (FY shorefast ice off Pt. Barrow, AK, 140 cm). Model predicted transmittances are for bare ice with thickness 100 cm, 150 cm, and 200 cm. The Delta-Eddington radiative transfer calculations are shown as solid colored lines. The lowest layer of sea ice includes algal absorption of 75 mg Chl a m^{-2} over a 0.5 m thick layer (see Table 16), and therefore a visible absorption optical depth of 0.3 .

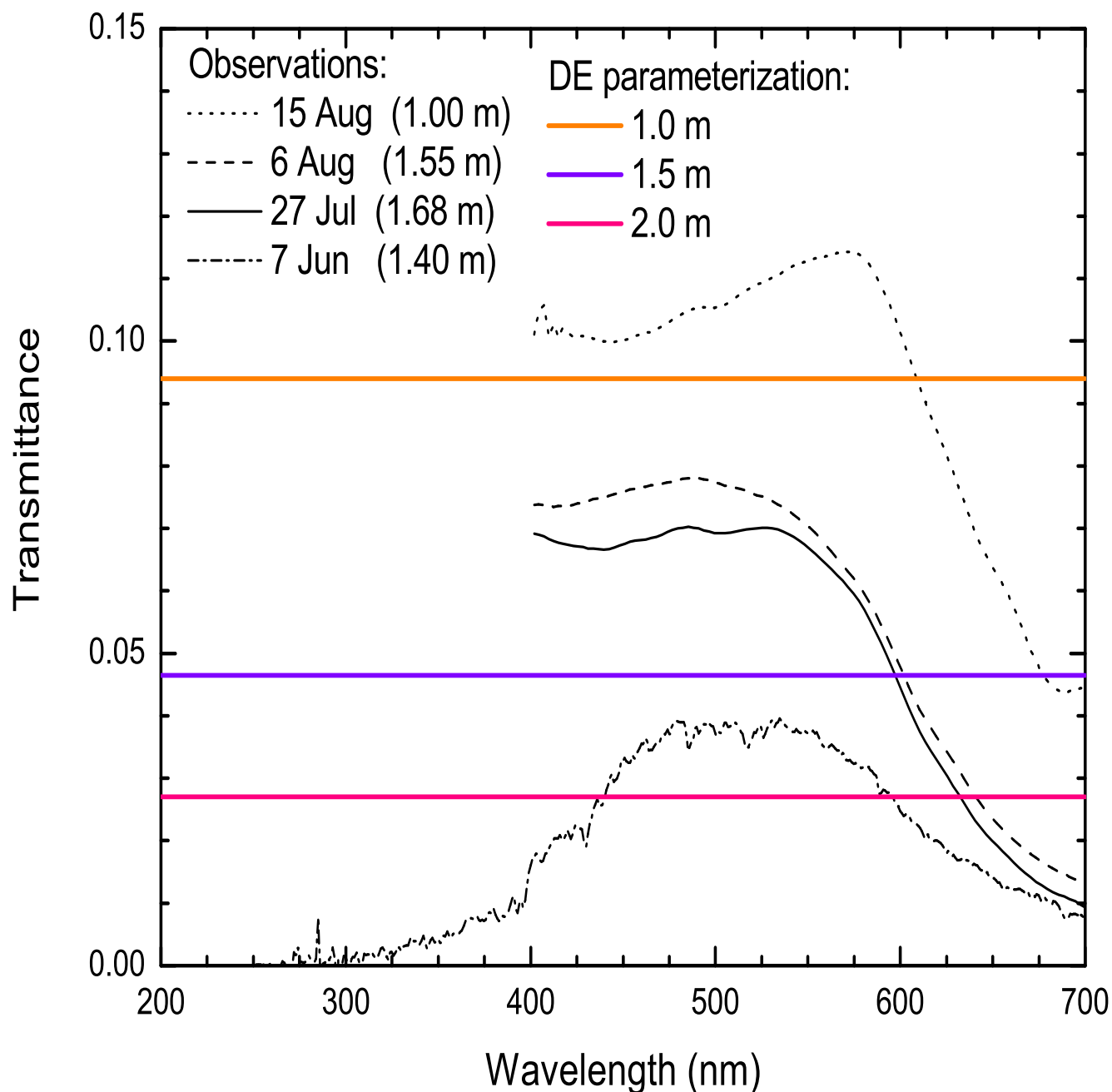


Figure 9. Observed and modeled spectral transmittance for a melt pond on 27 July (Multi-year ice, 146 cm ice thickness). The model calculation is for ponded ice with thickness 150 cm underlying 50 cm of water. It was computed using the IOPs of Table 15, along with the Delta-Eddington radiative transfer calculation. The lowest layer of sea ice includes algal absorption of 75 mg Chl a m^{-2} over a 0.5 m thick layer (see Table 16), and therefore a visible absorption optical depth of 0.3 .

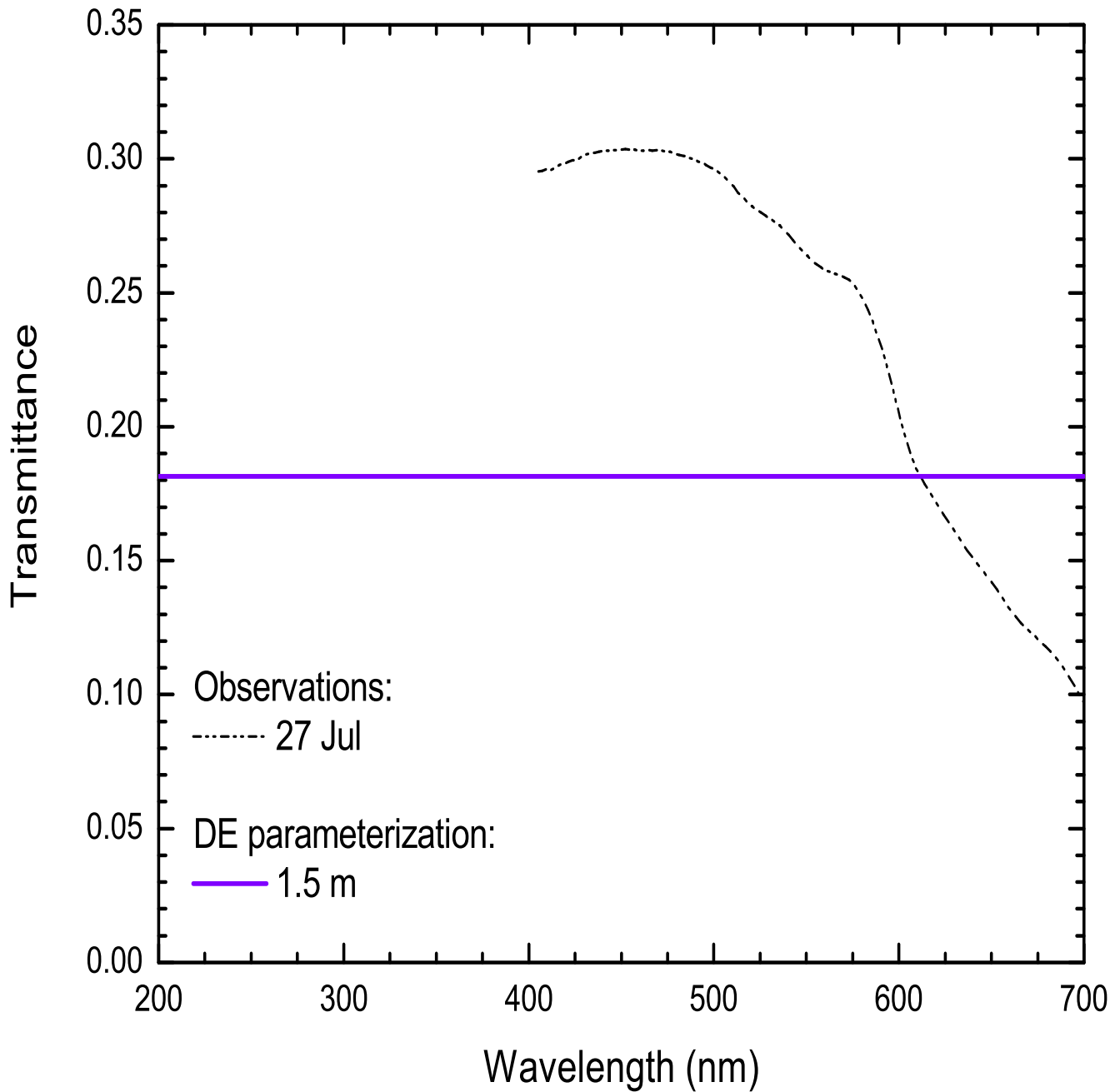


Figure 10. Average albedos for bare and ponded ice along with model calculated band-averaged albedos for ice scattering coefficients increased/decreased by one standard deviation ($\pm 15\%$) for bare ice (green), two standard deviations ($\pm 30\%$) for bare ice (cyan), and one standard deviation for ponded ice ($+300\%$, -50% , green). Bare ice and ponded ice spectral albedos and related standard deviations were obtained along the albedo line during the SHEBA observations of the summer of 1998. The model calculated band-averaged albedos use the IOPs of Tables 12 and 15, along with the Delta-Eddington radiative transfer calculation. For the model calculations, bare sea ice is 2.0 m thick, while pond-over-ice is 0.35 m deep and ice-under-pond is 1.5 m thick.

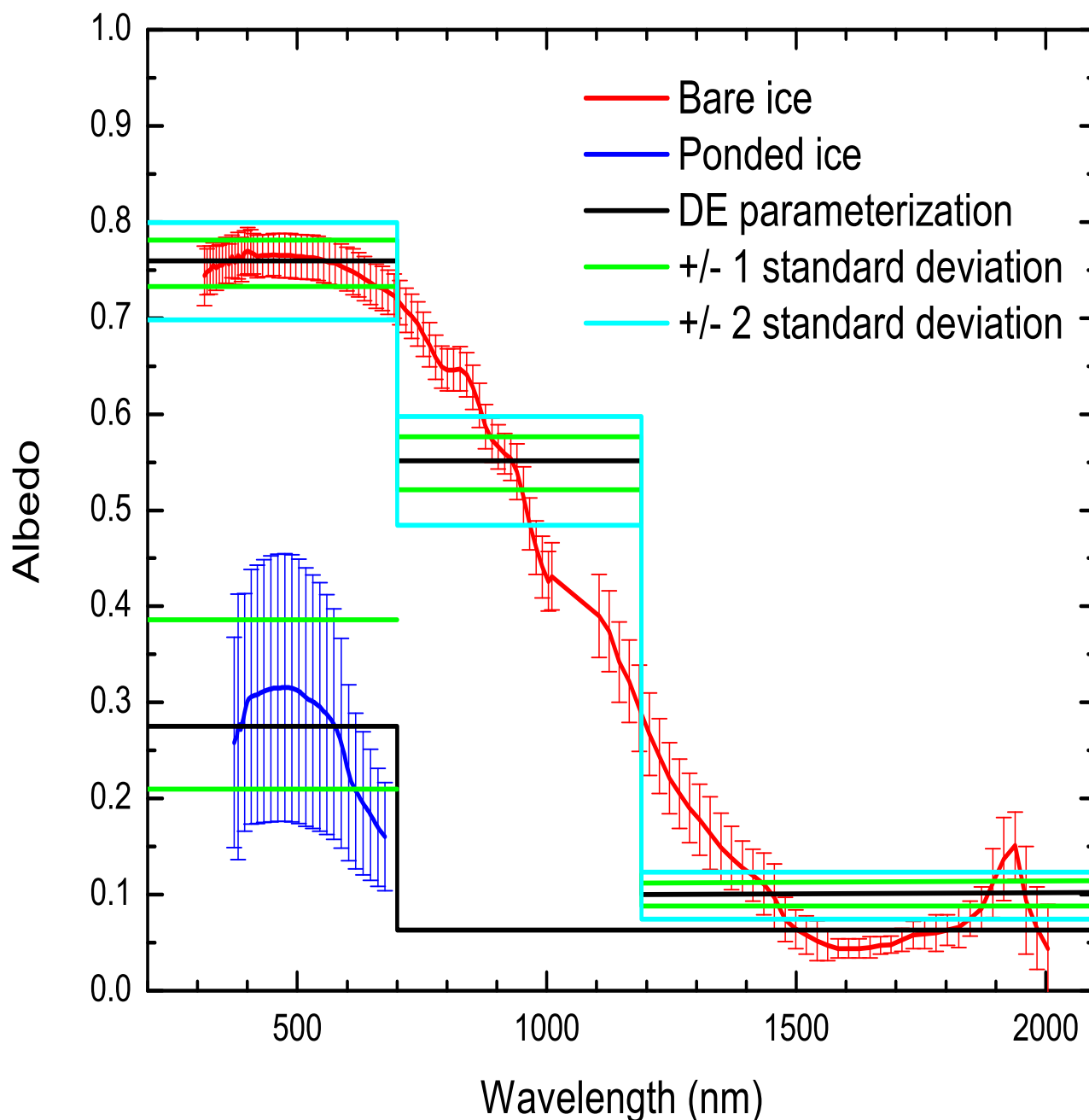


Figure 11. Model predicted transmittance for 1.5 m thick bare ice calculated using $\pm 15\%$ change in scattering to represent one standard deviation change in surface albedo and $\pm 30\%$ change in scattering to represent a two standard deviation change in surface albedo. Predicted transmittances are compared with observed transmittances shown in Fig. 8. They were computed using the IOPs of Table 12, along with the Delta-Eddington radiative transfer calculation. The lowest layer of sea ice includes algal absorption of 75 mg Chl a m^{-2} over a 0.5 m thick layer (see Table 16), and therefore a visible absorption optical depth of 0.3 .

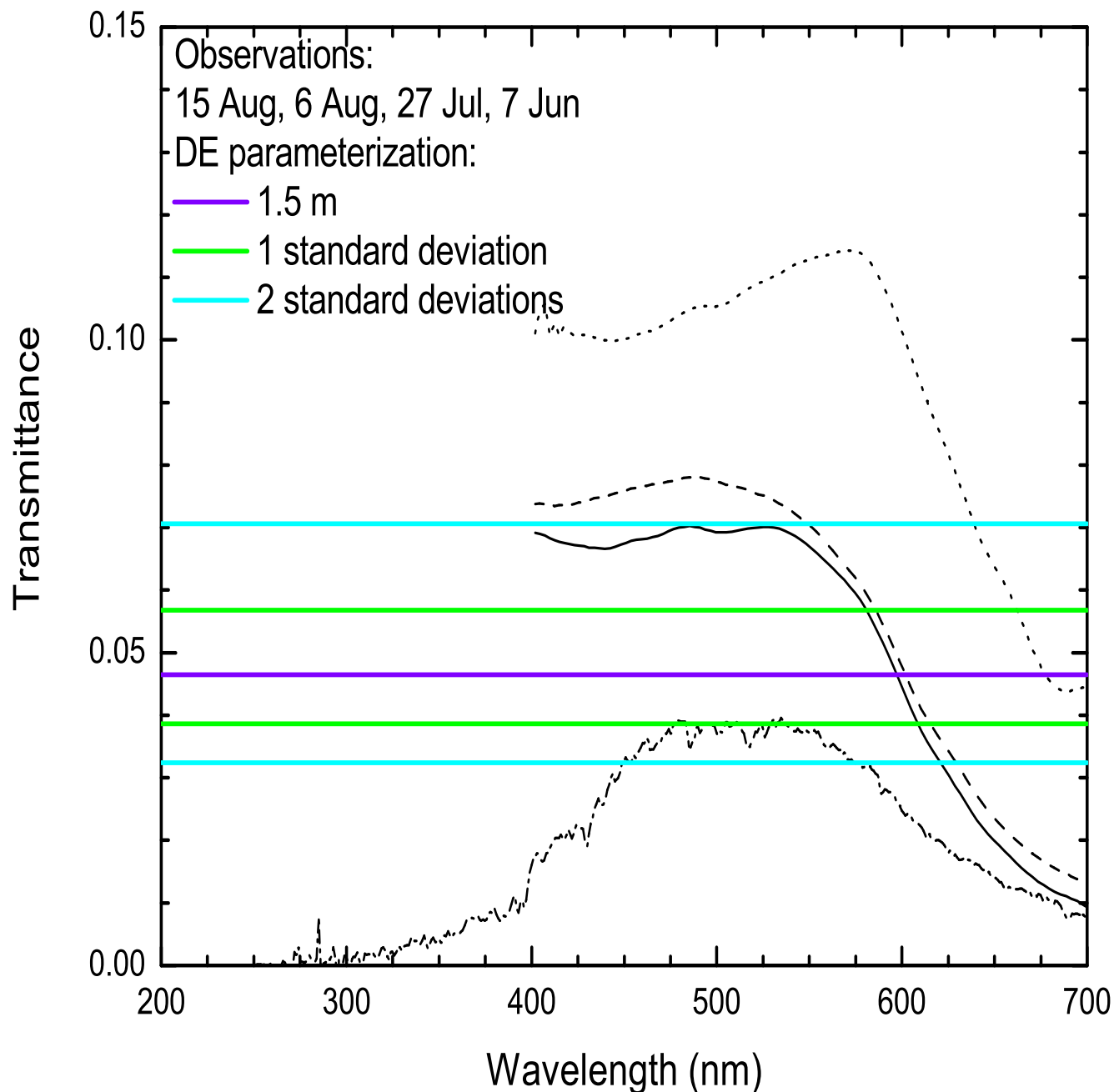


Figure 12. Model predicted transmittance for 1.5 m thick ponded ice calculated using -50% and +300% change in scattering to represent one standard deviation change in surface albedo. Predictions are compared with observed transmittance for ponded ice on 27 July (Fig. 9). They were computed using the IOPs of Table 15, along with the Delta-Eddington radiative transfer calculation. For the model calculations, sea ice is 1.5 m thick and pond-over-ice is 0.35 m deep. The lowest layer of sea ice includes algal absorption of 75 mg Chl $a\ m^{-2}$ over a 0.5 m thick layer (see Table 16), and therefore a visible absorption optical depth of 0.3 .

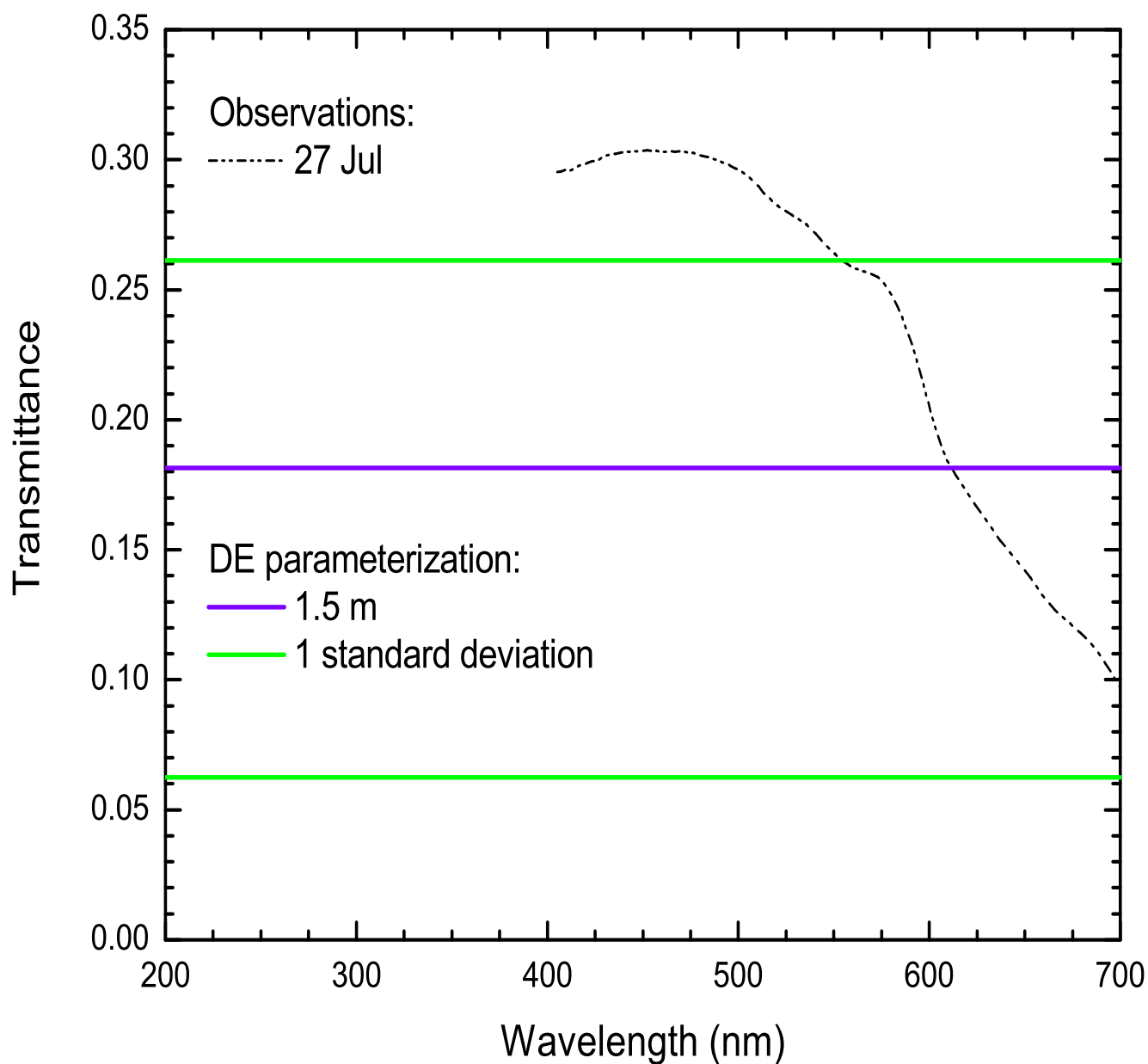


Figure 13. Broadband albedo vs pond depth over ice of various thicknesses, from the Delta-Eddington solar radiation parameterization. Overcast conditions with cosine solar zenith angle $\mu_0 = 0.5$. Pond thicknesses less than .005 m are set to zero, so the leftmost values are for bare sea ice. For pond depth in the range .005 m to .020 m, IOPs for ponded ice and bare ice are weighted together by pond depth. The unrealistically large pond depths (up to 10 m) are included to show how very deep pond broadband albedo asymptotes to the diffuse ocean broadband albedo of 0.063.

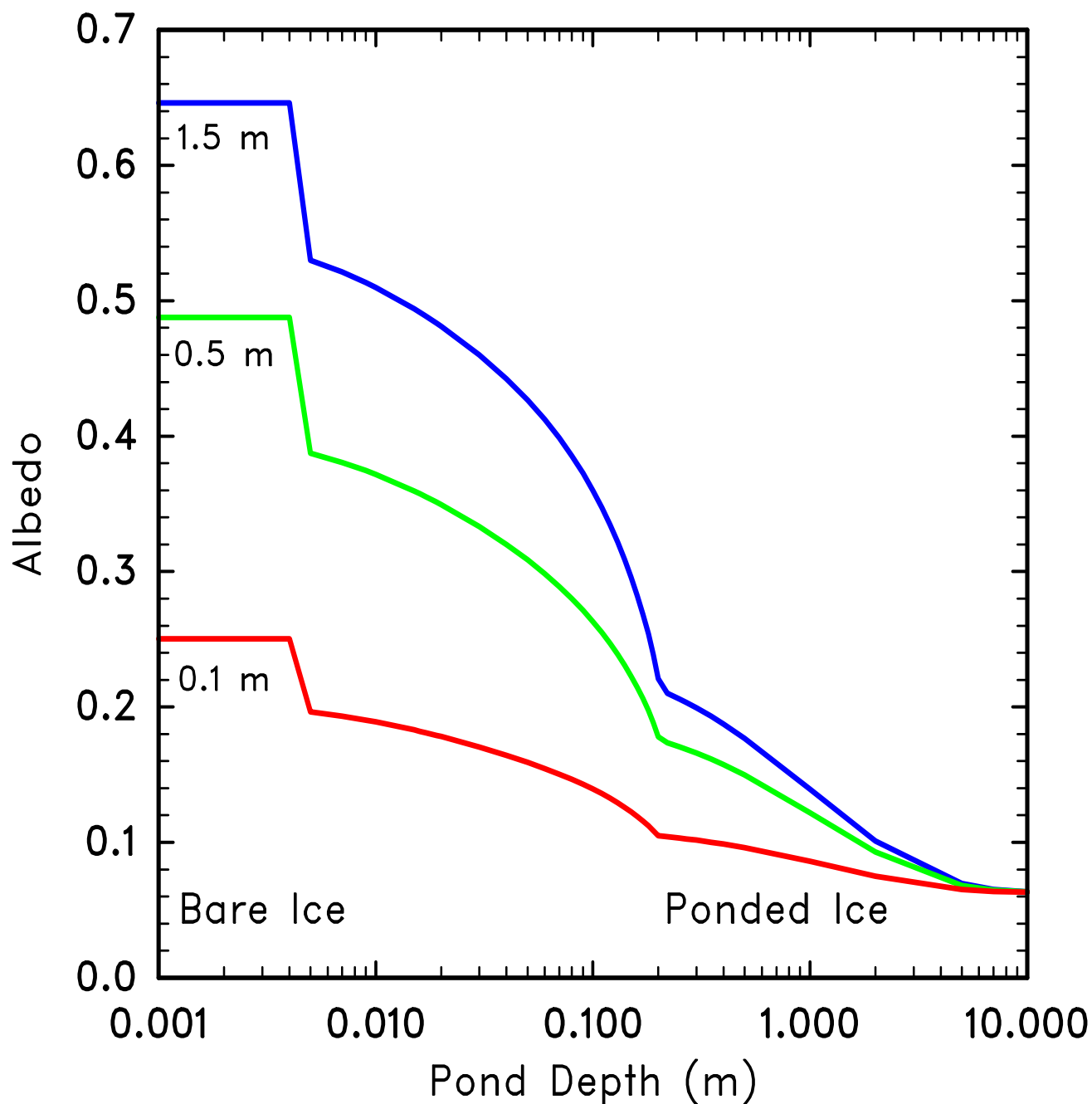


Figure 14. Broadband albedo with ice thickness: comparison of Delta-Eddington solar radiation and CCSM3. Overcast conditions with cosine solar zenith angle $\mu_0 = 0.5$. Various available observations are included. For the Delta-Eddington solar radiation, the surface scattering layer thickness is $h_i/30$ for sea ice thinner than 1.50 m, and .05 m for thicker sea ice, where h_i is the total sea ice thickness. For CCSM3 solar radiation, sea ice thicker than 0.5 m has constant albedo, while sea ice thinner than 0.5 m has an empirical thickness dependence.

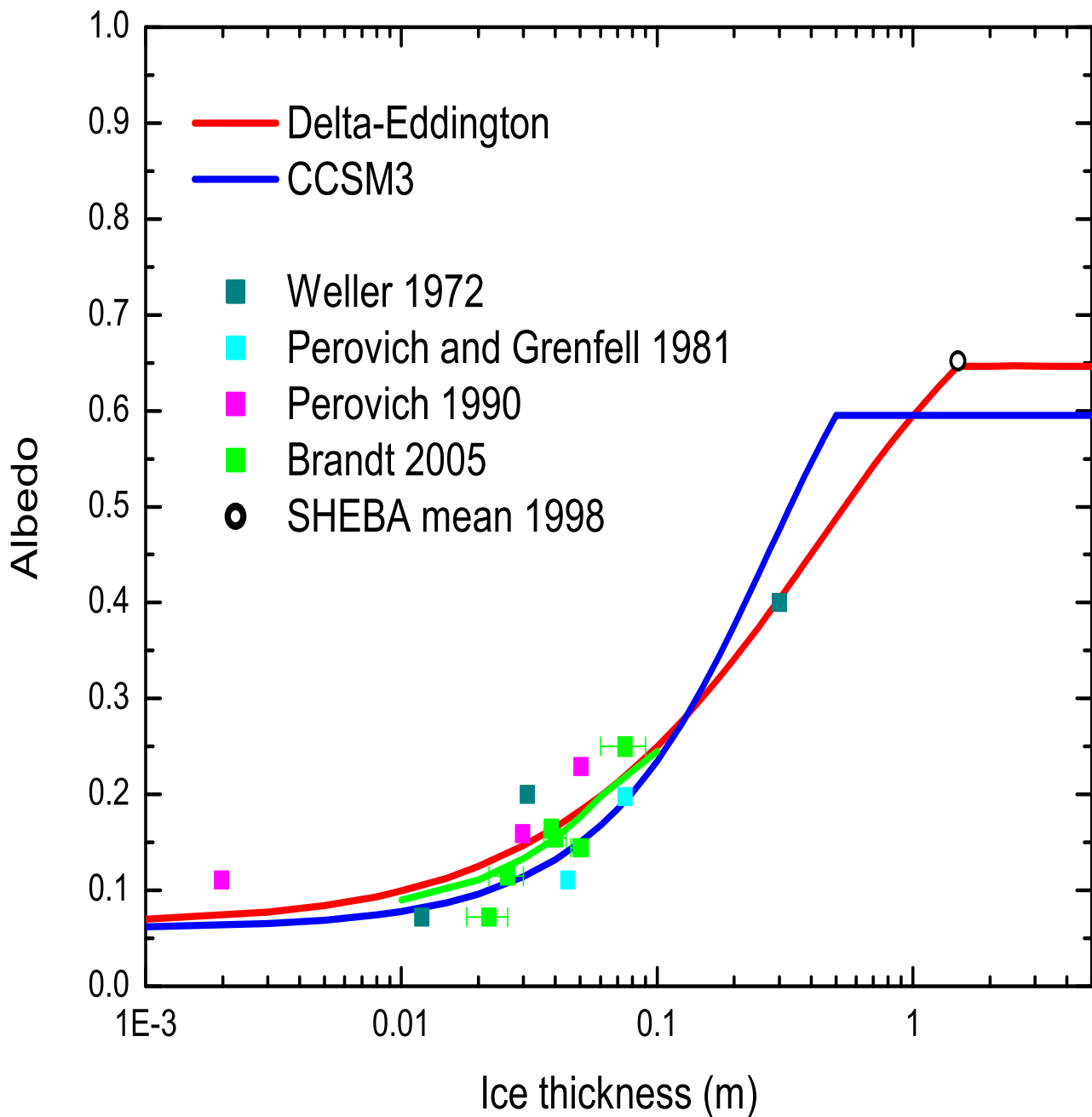


Figure 15. Comparison of I_0 with ice thickness: Delta-Eddington solar radiation (solid) and CCSM3 (dash). Overcast conditions with cosine solar zenith angle $\mu_0 = 0.5$. I_0 is the fraction of sea ice absorbed solar radiation that penetrates the surface scattering layer. Visible (vs, 0.2-0.7 μm , blue) and near-ir (nir, 0.7-5.0 μm , red) shown separately. The near-ir value for CCSM3 is zero.

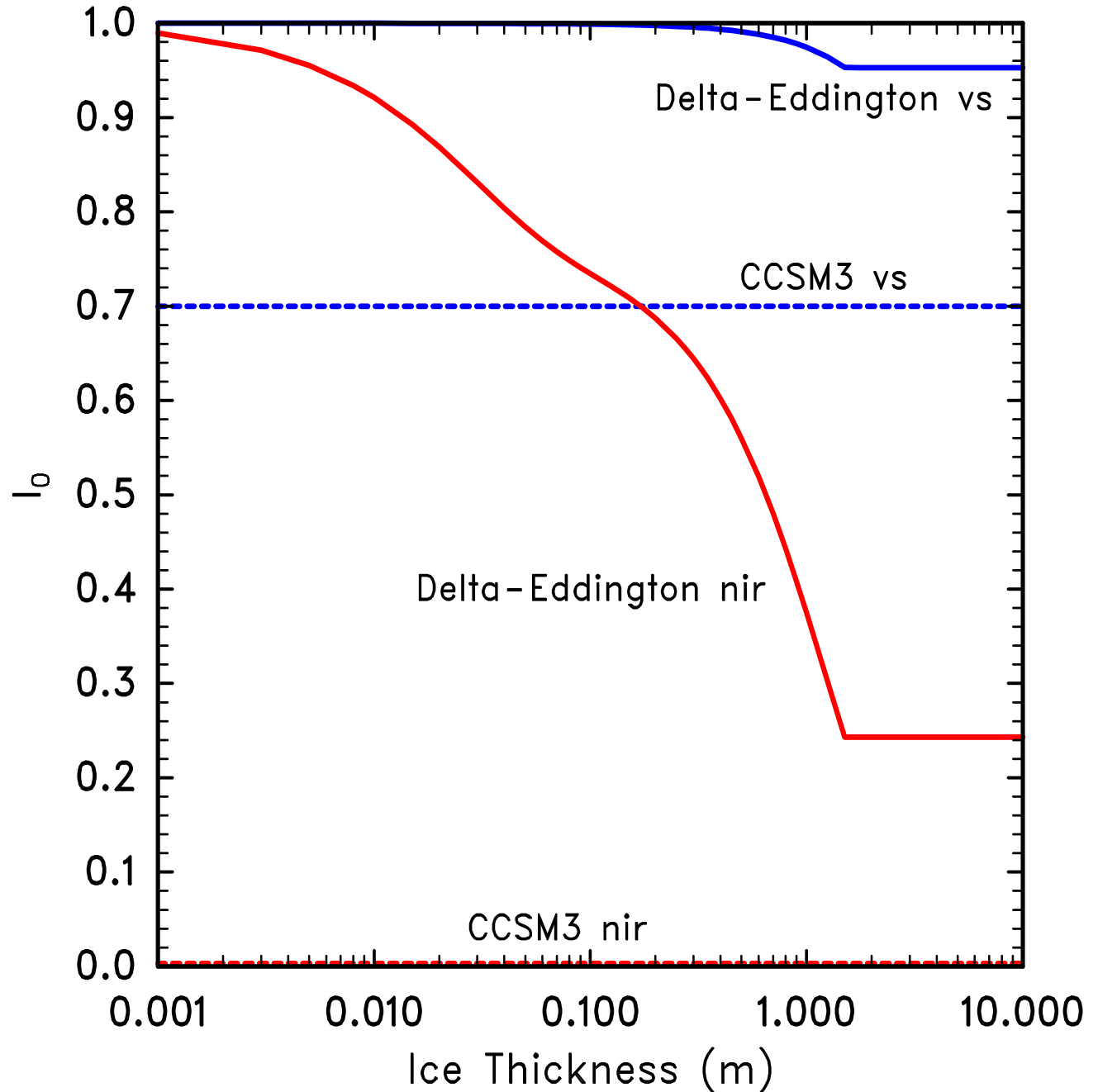


Figure 16. Sea ice transmittance to the underlying ocean with ice thickness: comparison of Delta-Eddington solar radiation (solid) and CCSM3 (dash). Overcast conditions with cosine solar zenith angle $\mu_0 = 0.5$. Visible (vs, 0.2-0.7 μm , blue) and near-ir (nir, 0.7-5.0 μm , red) shown separately. The near-ir value for CCSM3 is zero.

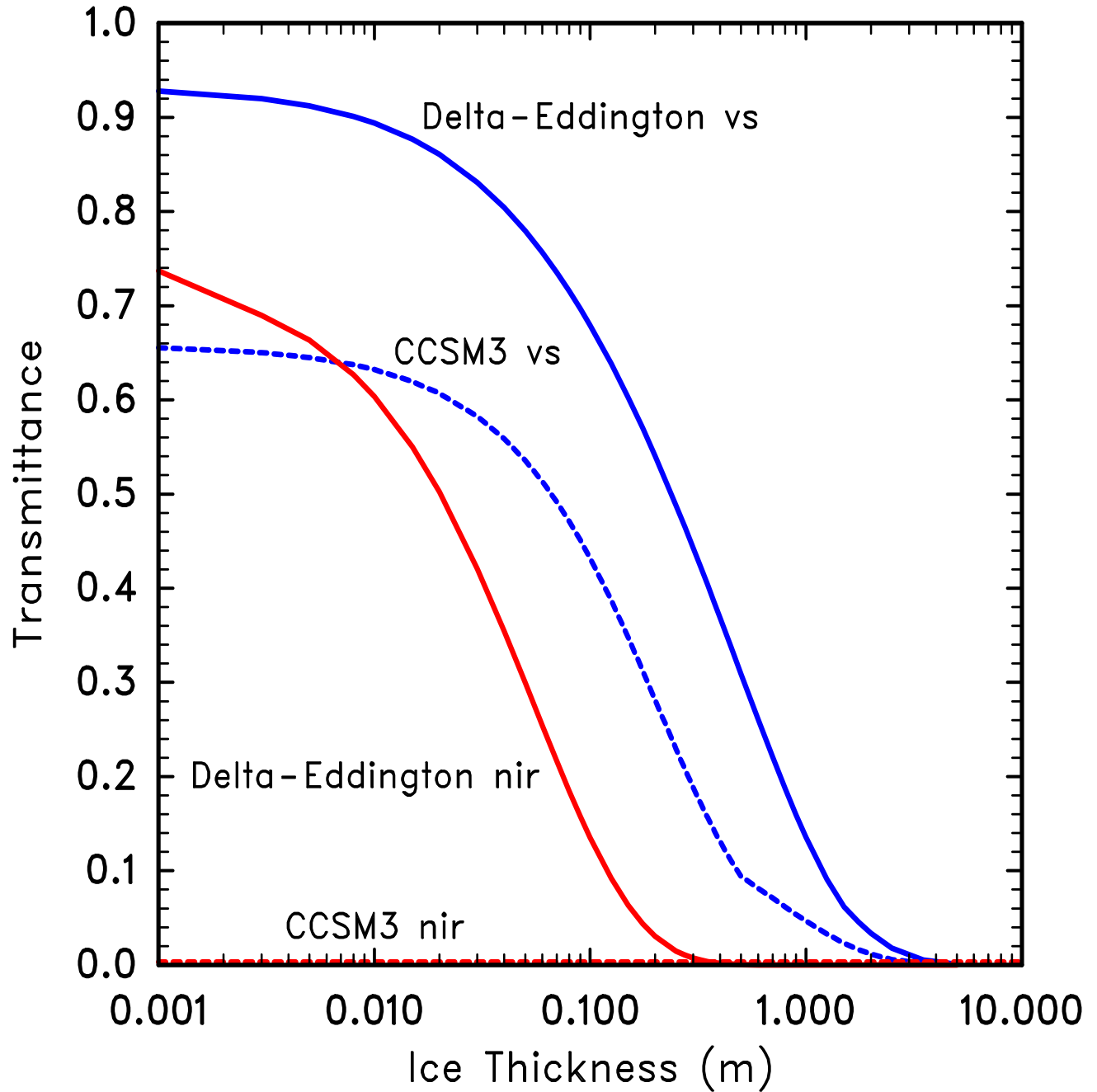


Figure 17a. Absorption profiles for bare ice: comparison of Delta-Eddington solar radiation and CCSM3 visible band. Overcast conditions with cosine solar zenith angle $\mu_0 = 0.5$. The plain colored bars are for Delta-Eddington, the stippled bars are for CCSM3. The legend indicates three ice thicknesses, 0.1 m, 1.0 m and 5.0 m.

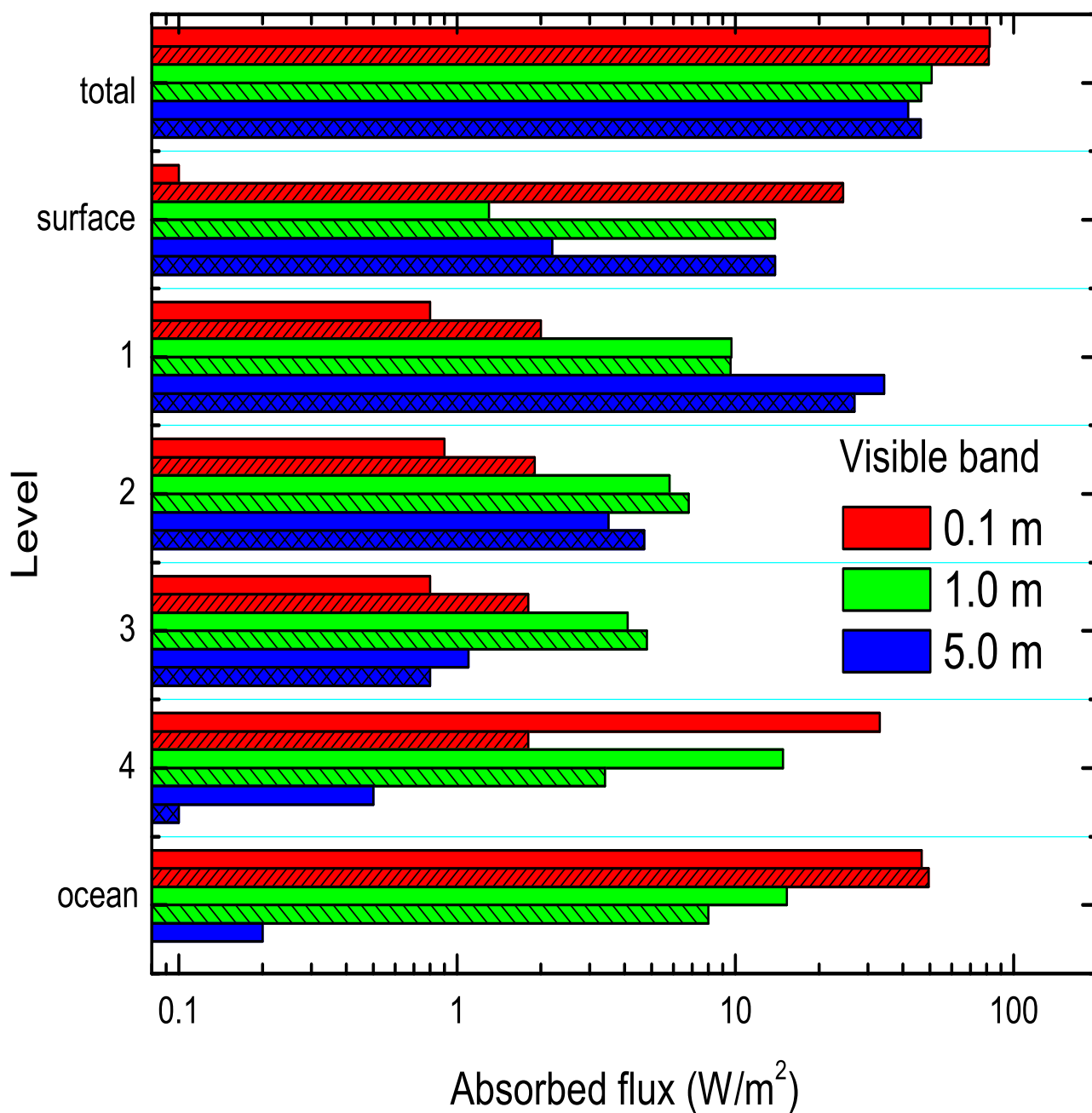


Figure 17b. Absorption profiles for bare ice: comparison of Delta-Eddington solar radiation and CCSM3 near-infrared band. Overcast conditions with cosine solar zenith angle $\mu_0 = 0.5$. The plain colored bars are for Delta-Eddington, the stippled bars are for CCSM3.

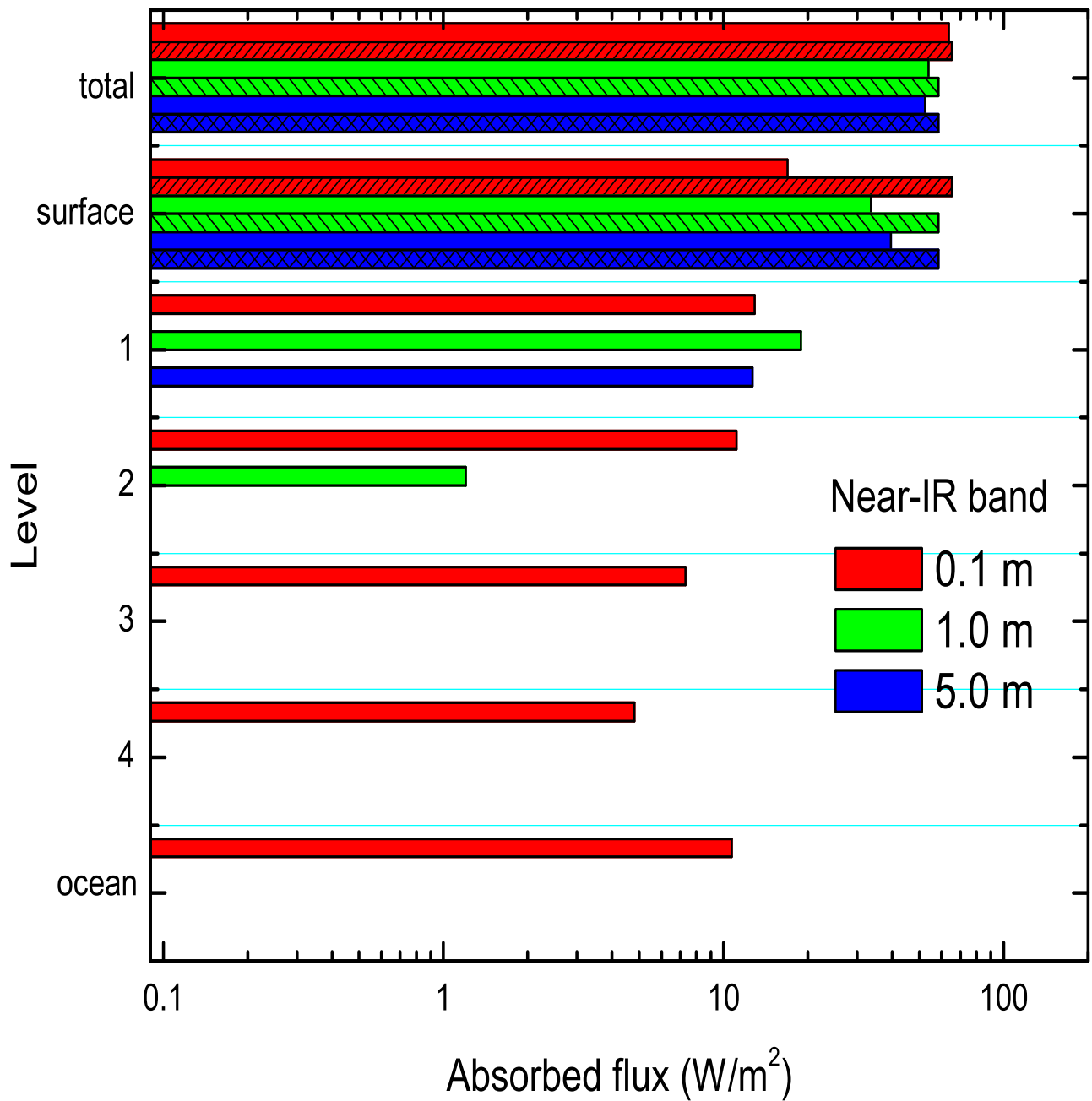


Figure 17c. Absorption profiles for bare ice: comparison of Delta-Eddington solar radiation and CCSM3 broadband. Overcast conditions with cosine solar zenith angle $\mu_0 = 0.5$. The plain colored bars are for Delta-Eddington, the stippled bars are for CCSM3.

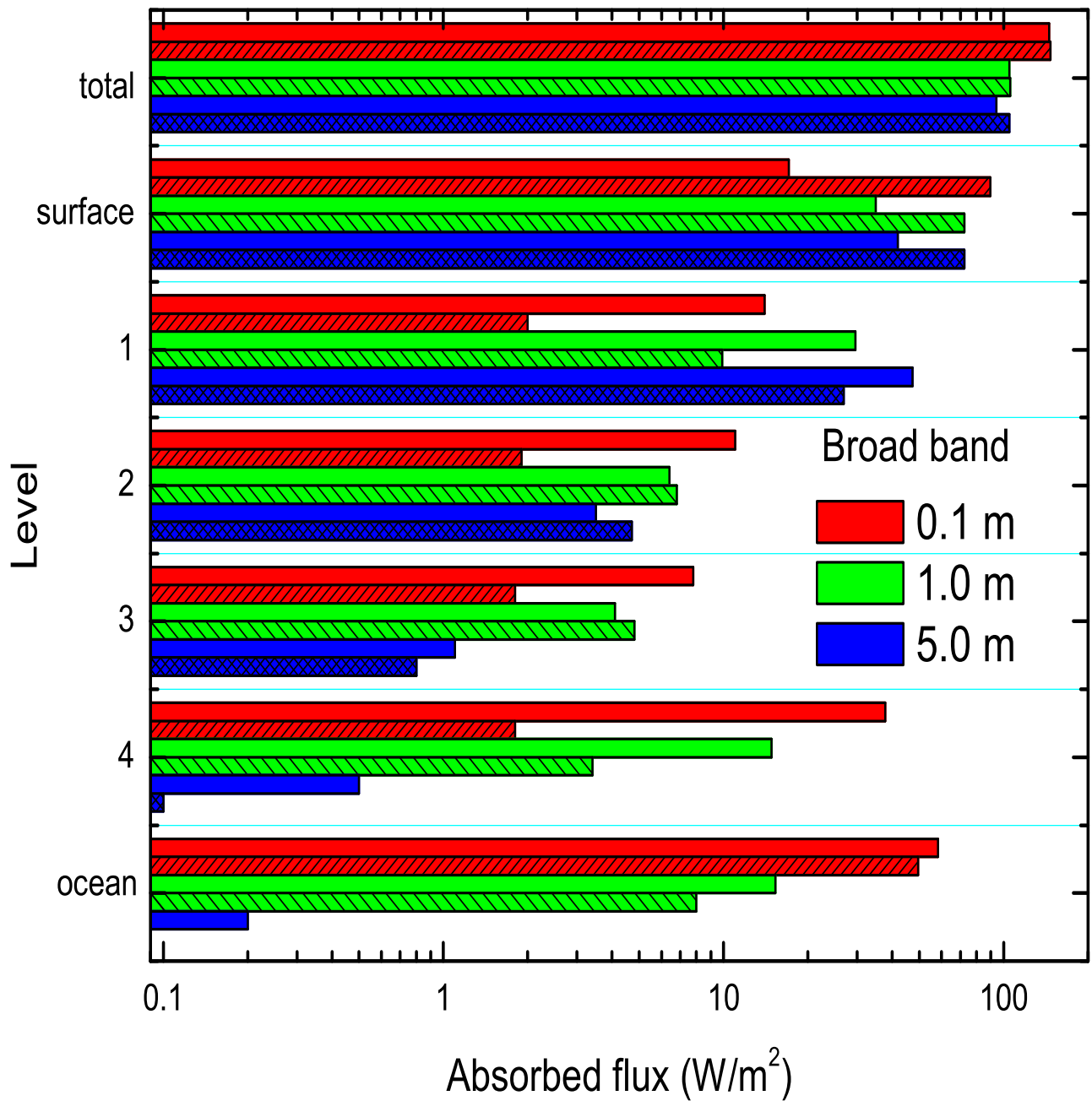


Figure 18. Broadband albedo vs cosine solar zenith angle for clear sky conditions, from the Delta-Eddington solar radiation parameterization. The range in solar zenith angles is appropriate for solstice conditions at the Arctic and Antarctic circles. Snow and pond completely cover sea ice. Snow and pond thickness over 1.5 m thick sea ice shown; bare ice thickness shown, and additionally for snow, the grain radius. The decline in broadband albedo for the lowest elevation angles is due both to predominately diffuse irradiance for which surface albedos are lower than direct albedos, and to a larger portion of near-ir irradiance compared to visible irradiance.

